Hierarchical modelling of molecule-surface interactions: Towards the simulation of polymer coating systems

TECHNISCHE UNIVERSITÄT DARMSTADT

Vom Fachbereich Chemie
der Technischen Universität Darmstadt

zur Erlangung des akademischen Grades eines
Doktor rerum naturalium (Dr. rer. nat.)

genehmigte
Dissertation

vorgelegt von

Dipl.-Chem. Claudia Rosemarie Herbers

aus Lingen (Ems), Deutschland

Referent:	Prof. Dr. Nico F. A. van der Vegt
Korreferent:	Prof. Dr. Müller-Plathe
Tag der Einreichung:	03.05.2012
Tag der mündlichen Prüfung:	25.06.2012

Darmstadt 2012

D17

Contents

Summary

A microscopic insight into the interaction of small molecules or macromolecules with surfaces is important in order to understand mechanisms that are determined by interface properties. From an application point of view, it provides a powerful route to tackle problems related to wetting, material development, polymer coatings, nanodevices, biomolecular recognition or self-assembly. From a computational point of view, the atomistic modelling of such complex interface systems is, at the current point of research, still a challenging problem. The complex interface between soft matter and hard matter cannot be easily described by using standard simulation approaches. While quantum calculations could, in principle, provide a detailed description of the electronic structure at the interface, they lack the computational efficiency needed to reach time and length scale that are sufficient to describe the system. Standard classical atomistic models, on the other hand, are developed to describe bulk properties. Originating from this computationally challenging situation, a dual-scale modelling approach was proposed, which combines the two level of resolution. In this approach quantum chemical information on near-surface conformations and corresponding adsorption energies are used to parameterise classical force fields.

This thesis reviews the current state-of-the-art of atomistic modelling of surface interactions and discusses current challenges in the field, some of which are addressed in this thesis. The quantum-classical modelling approach was used to develop force fields for water on ZnO(0001) and ethanol on α-alumina. A global optimisation technique, a genetic algorithm, was implemented to optimise the fitting procedure of the classical force field. This allows for the parameterisation of complex interfacial interactions, which cannot be performed manually anymore. Furthermore, the representability of the classical force fields that are obtained by the quantum-classical modelling approach is a central issue. The representability of the force fields, which is the ability to predict adsorption states that have not been used as a target in the parameterisation, has been only poorly addressed in the current literature. However, the correct prediction of the sensitive interplay of the entropic and enthalpic con-

tributions at the interface is essential for obtaining reliable simulation results. This thesis identifies the important aspects that have to be considered in the fitting procedure in order to obtain reliable force fields. It has been demonstrated that only a balanced subset of quantum chemical data, that contain information about distance-, orientation- and site-dependences, result in a force that is representable enough to provide an accurate description of the adsorption energy landscape.

The implementation of the quantum-classical modelling approach presented in this thesis opens a promising route to simulate larger scale interface systems, like polymer coatings, which are interesting from an applications point of view. Preliminary results for atomistic simulations of a polyurethane coating on ZnO are presented. These coatings are used as anti-corrosive barrier coatings, which should prevent water and other impurities from penetrating through the polymer to the surface. A detailed microscopic understanding of the water or impurity permeation in such systems could help to optimise the coating's properties. It has been shown in this thesis that atomistic as well as recently developed mesoscale techniques have successfully been used to model polymer permeation. This thesis can therefore be seen as a first step towards a comprehensive multiscale modelling study of polymer coating systems, which encompasses the quantum, atomistic and mesocale level of resolution.

Zusammenfassung

Ein mikroskopisches Verständnis der Wechselwirkung zwischen kleinen Molekülen bzw. Makromolekülen und anorganischen Oberfächen ist die Vorraussetzung, um Phänome zu verstehen, die durch die spezifische Wechselwirkung an der Grenzfläche hervorgerufen werden. Dies ist besonders aus anwendungsorientierter Sicht interessant, da hierdurch neue Lösungsvorschläge für Probleme im Bereich Benetzung, Materialentwicklung, Polymerbeschichtungen, Nanomaterialen, sowie biologische Implantate oder Biosensoren entwickelt werden können. Aus theoretischer Sicht hingegen, stellt die klassische Modellentwicklung zur Beschreibung von komplexen Grenzflächen zwischen weicher und harter Materie immer noch ein zentrales Problem dar, da die gängigen Simulationstechniken diesbezüglich an ihre Grenzen stoßen. Eine quantenchemische Berechnungen der Molekül-Oberflächen Wechselwirkung kann hier prinzipiell Aufschluss über die elektronische Struktur an der Grenzfäche geben. Allerdings können gegenwärtig nur solche Zeit- und Längenskalen erreicht werden, die für die Beschreibung derartige Systeme nicht ausreichend sind. Die geläufigen klassischen, atomistischen Modelle wiederum sind hingegen so parametrisiert, dass sie lediglich die Bulk-Eigenschaften des Systems beschreiben können. Sogenannte Multiskalen-Modellierungsmethoden haben sich in diesem Kontext als besonders nützlich herausgestellt, da sie die bestehende Lücke zwischen quantenchemischer und atomistischer Ebene schließen können. Hierbei wird das klassische Kraftfeld mithilfe von quantenchemischen Informationen über Grenzflächenkonformationen und Adsorptionsenergien parametrisiert.

Diese Arbeit gibt einen ausführlichen Überblick über den aktuellen Stand der Forschung im Bereich der atomischen Simulationen von Oberflächenwechselwirkungen. Dabei werden aktuelle Probleme und Fragestellungen diskutiert und deren Lösungsansätze im Rahmen dieser Arbeit präsentiert. Basierend auf einer Vielzahl von quantenchemischen Berechnungen wurden mithilfe einer zweiskaligen Modellierungsmethode Kraftfelder für die Systeme Wasser auf ZnO(0001) und Ethanol auf α-A_2O_3 entwickelt. Ein evolutionärer Algorithmus wurde als globales Optimierungsverfahren implementiert, um die Parametrisierung von komplexen Grenz-

flächenwechselwirkungen zu ermöglichen. Darüberhinaus ist die Validierung der klassischen Kraftfelder von zentraler Bedeutung, da nur akkurate und zuverlässig bestimmte Kraftfelder garantieren können, dass Grenzflächenphänomene adäquat prognostiziert werden können. In der Literatur sind allerdings kaum Studien über die Qualität und Validierung von klassichen Kraftfeldern zu finden. Hieraus resultiert die Frage, inwiefern diese Modelle in der Lage sind, andere Adsorptionskonformationen und -energien, die nicht zuvor in die Parametrisierung eingeflossen sind, korrekt zu beschreiben. Als Ergebnis dieser Arbeit hat sich herausgestellt, dass quantenchemische Adsorptionenergien als Funktion der Position, Orientierung und Distanz des Moleküls bezüglich der Oberfäche in die Parametrisierung einbezogen werden sollten.

Die in dieser Arbeit neuartig optimierte und implementierte zweiskalige Modellierungsmethode zur Beschreibung von Molekül-Oberflächen Wechselwirkungen stellt einen vielversprechenden Ansatz zur Simulation von größeren, reellen Systemen dar. Polymerbeschichtungen, die oft als Korrosionsschutz für Metalle oder metalloxidische Oberflächen verwendet werden, beinhalten komplexe Grenzflächen zwischen weicher und harter Materie und könnten somit beispielsweise mithilfe dieser Methode simuliert werden. Diese Arbeit präsentiert erste Ergebnisse zu Simulationen von Polyurethanbeschichtungen auf ZnO(0001). Hierbei ist besonders eine mikroskopische Studie zur Permeation von Wasser und anderen Verunreinigungen innerhalb des Polymernetzwerkes von großem Interesse, da ein Verständnis von mikroskopischen Mechanismen zur gezielten Optimierung derartiger Polymerbeschichtungen beitragen kann. Weiterhin wird gezeigt, dass die gegenwärtigen atomistischen und vergröberten, mesoskaligen Modelle die Permeation von kleineren Molekülen zuverlässig beschreiben können. Insgesamt stellt diese Arbeit somit einen ersten, vielversprechenden Schritt in Richtung von Multiskalensimulationen zur Beschreibung von Polymerbeschichtungen auf festen anorganischen Oberflächen dar.

Danke!

Ich möchte an dieser Stelle die Gelegenheit nutzen Danke zu sagen. Mein Dank gebührt zunächst den Mitgliedern meiner Prüfungskommission Frau Prof. Thiele, Herrn Prof. Biesalski und inbesondere Herrn Prof. Müller-Plathe, der mir durch zahlreiche wissenschaftliche Diskussionen immer wieder neue Anregungen gegeben und mich so stets wissenschaftlich unterstützt hat. Desweiteren gilt ein besonderer und herzlicher Dank meinem Betreuer Nico van der Vegt, ohne den diese Arbeit nicht möglich gewesen wäre. Sein wissenschaftlicher Enthusiasmus, seine unkonventionelle Art und seine enorme Motivation sind einfach großartig und inspirierend. Ich habe die Zeit in seiner Arbeitsgruppe am Max-Planck-Institut für Polymerforschung in Mainz, als auch hier am Center of Smart Interfaces der TU Damstadt sehr genoßen und es ist umso unglaubwürdiger, dass diese tolle Zeit schon so bald zu Ende sein soll. In den letzten Jahren habe ich viele wundervolle, unterschiedliche Menschen kennengelernt. Einige von ihnen sind gute Freunde geworden, was mich besonders gücklich macht. Ich möchte an dieser Stelle deshalb all meinen Kollegen und Freunden am MPI-P in Mainz und am CSI in Darmstadt danken. Ein herzlicher Dank gilt natürlich auch der Arbeitsgruppe von Florian Müller-Plathe.

Zuletzt möchte ich einigen Freunden und Kollegen ganz besonders danken, da sie mir in den letzten Jahren viel Freude und Unterstützung geschenkt haben. Es ist wirklich schön solch' tolle Menschen um sich zu haben. Thank you so much, Simon! Grazie mille, Valentina e Emiliano! Xie-xi-ni, Chunli! Danke je wel, Pim en Nico! Danke, Imke! Und großes Dankeschön an alle meine tollen Kollegen am CSI!

Introduction

One of the recent challenges in the fields of wetting, material development, polymer coatings, nanodevices, biomolecular recognition, implantology and self-assembly is the detection and understanding of those mechanisms that determine material properties. In systems that contain a soft-hard matter interface, the macroscopic properties are usually determined by the specific nature of the interfacial interactions. Hence, microscopic insights can help to overcome recent challenges and open a powerful route towards the targeted design of materials. Over the past few decades, computer simulations have proven to be a useful, powerful tool that can provide a microscopic understanding of the system. However, the classical modelling of surface interactions is still a major challenge for modern computer simulation techniques. This thesis presents new and improved methods to tackle this problem and aims to provide tools to model realistic soft-hard interface systems.

A polymer coating on a solid substrate is a perfect example of a complex soft-hard interface system in which macroscopic properties are determined by the complex interplay of entropic and enthalpic contributions at the interface. A polyurethane coating on ZnO(0001) has been chosen as a model system for an anti-corrosive barrier coating. In order to model such systems, methods are needed that employ multiple levels of resolution. On the one hand, an accurate description of the electronic structure at the interface is necessary in order to capture near-surface conformations and corresponding adsorption energies. On the other hand, mescoscale, so-called "coarse-grained", simulation techniques are necessary in order to reach sufficient length and time scales to simulate realistic polymer coating systems. In an anti-corrosive coating system, it is especially important that the polymer permeation of water and other impurities is captured accurately, which is not clear a priori for coarse-grained models. However, in this thesis, it is demonstrated, based on a thorough study of a polystyrene-additive system, that the diffusion and the solubility of different penetrants are well accessible with recently developed coarse-grained models. The most challenging step, which forms the focus of this thesis, is the classical, atomistic modelling of surface interactions. While quantum calculations can in principle provide an accurate, microscopic picture of the interface, classical simulation

techniques lack reliable models that can capture surface interactions correctly. However, quantum methods, despite the progress in computational power over recent decades, still do not reach the length and time scales needed to model realistic systems. As a result, previous studies have proposed a dual-scale modelling approach that combines these two level of resolution in a bottom-up fashion. The quantum information is transferred to the atomistic scale by parameterising classical force fields such that they reproduce quantum data.[1–20] This thesis begins by reviewing the current state-of-art of quantum-classical modelling of surface interactions and discusses the current challenges in the field. One of the biggest challenges is the representability of the classical force field, that is, the ability to predict adsorption states different to those used in the parameterisation. This issue has only been poorly addressed in the literature. However, reliable force fields are essential in order to capture the sensitive entropic and enthalpic interplay at the interface. In the early 2000s, Abrams, Delle Site et al. were one of the first groups to study a realistic technical material using a dual-scale modelling approach.[4,21,22] They studied polycarbonate on nickel (present in optical data storage and nanodevices) and found that even small modifications to the chemical substructure of the polymer, such as the chain ends, can sensitively control the interfacial behaviour of the polymer. This shows the importance of a multiscale modelling approach that can transfer characteristic information of the system from the quantum level over the atomistic level up to a mesocale level. This is a challenging approach in which many open questions remain, some of which will be be addressed at the end of this thesis.

The thesis is structured as follows. Chapter 1 reviews the current state-of-the-art of quantum-classical modelling of surface interactions and discusses current challenges in the field, some of which will be addressed in chapters 2 and 3. In order to optimise the fitting procedure, a global optimisation technique (a genetic algorithm) has been implemented in the quantum-classical modelling scheme and this is discussed in chapter 2. This procedure enables complex, heterogeneous adsorption energy landscapes to be modelled in a fast and efficient way. A classical force field for the interaction of water with a partially hydrogen-terminated ZnO(0001) surface has been developed using the previously described technique. In the literature, the fitting of such classical force fields has often been done by considering only one or a few quantum data, which means that only part of the complex adsorption energy landscape is taken into account. Herein, the effect of this choice of target

quantum information on the representability of the force field is also discussed. This representability study has been taken one step further in chapter 3: an extensive quantum chemical study of ethanol on α-alumina has been performed, which provides information of the change of the adsorption energy as a function of distance, position, and orientation of the ethanol with respect to the surface. In this chapter, it is demonstrated that fitting to a subset of quantum data influences the representability of the force field. The first steps towards the modelling a polymer coating systems are presented in chapter 4. Preliminarily results for a polyurethane coating system on ZnO(0001) are reported, in which the water permeation and its influence on the hydrogen bonding network is analysed. Chapters 5 and 6 demonstrate, based on the study of polystyrene-additive systems, that recent coarse-grained simulation techniques are capable of modelling polymer permeation. A polystyrene melt has been chosen as a model system since it is both experimentally and computationally well studied. Finally, chapter 7 highlights some remaining open questions in the field of multiscale modelling of surface interactions that have not been addressed in this thesis.

Publications

This thesis is based on the following publications:

C. R. Herbers, C. Li, and N. F. A. van der Vegt, *Grand challenges in atomistic modelling of molecule-surface interactions*, J. Comput. Chem. (submitted)

K. Johnston, C. R. Herbers, and N. F. A. van der Vegt, *Development of classical molecule-surface interaction potentials based on density functional theory calculations: Investigation of force field representability*, J. Phys. Chem. C (submitted)

C. R. Herbers*, E. Brini*, G. Deichmann, and N. F. A. van der Vegt, *Thermodynamic transferability of coarse grained potentials for polymer-additive systems*, Phys. Chem. Chem. Phys. (submitted)

C. R. Herbers, K. Johnston, and N. F. A. van der Vegt, *Modelling molecule-surface interactions: an automated quantum-classical approach using a genetic algorithm*, Phys. Chem. Chem. Phys., 13:10577 (2011).
Reproduced by permission of the PCCP Owner Societies

D. Fritz, C. R. Herbers, K. Kremer, and N. F. A. van der Vegt, *Hierarchical modeling of polymer permeation*, Soft Matter, 5:4556-4563 (2009).
Reproduced by permission of The Royal Society of Chemistry

* shared authorship

1 Grand challenges in atomistic modelling of molecule-surface interactions

A detailed understanding of the adsorption of small molecules or macromolecules to a materials surface is of importance e.g. in the context of material and biomaterial research. Atomistic simulations provide in principle provide microscopic insight in the complex entropic and enthalpic interplay at the interface. However, an application of atomistic simulations techniques to such interface systems is a non-trivial problem, mostly because commonly used force fields cannot be straightforwardly applied, as they are usually developed to reproduce bulk properties of liquids. Therefore, a dual-scale modelling approach has often been the method of choice in the past, in which the classical force field is parameterised such that quantum chemical (QC) information on near-surface conformations and adsorption energies is reproduced by the classical force field. We will discuss in this review the current state-of-the-art of quantum-classical modelling of molecule-surface interactions and outline the major challenges in this field. In this context we will, among other things, lay emphasis on discussing ways to obtain representable force fields and propose systematic and system-independent strategies to optimise the quantum-classical fitting procedure.

1.1 Introduction

Soft matter (like organic liquids, biomolecules or polymers) which is in direct contact with hard matter (like biominerals, metals, alloys or metal oxides) can be found in a wide range of systems. The nature of these systems is often determined by the specific interfacial interaction of molecules with the substrate. When a molecule approaches the interface it adsorbs on the surface. The adsorption can occur via physisorption or chemisorption depending on the nature of the interaction. The conformational phase space of the adsorbent at the interface is reduced in comparison to the bulk and preferential adsorption sites on the surface are occupied. This enthalpic and entropic interplay between the molecules and the substrate results in system specific macroscopic properties. Wettability, biomineralisation, coatings, implantology, biomaterials and catalysis are all examples for systems or effects where

the important phenomena happen at the interface. The importance of these soft-hard interface systems has been recognised in recent years, however, very little is understood at this point regarding the interfacial interactions and how theses relate to the material's properties. A detailed insight into the microscopic level of such systems is needed to understand macroscopic phenomena and open a systematic route to improve or develop new materials. However, interfacial systems are highly complex and thus non-trivial to characterise neither with experimental techniques nor with simulation methods[23–28]. Especially computer simulations studies, that are focussing on modelling soft-hard interfaces, encounter many challenges. Mostly because standard atomistic force fields, like GROMOS[29–31], CHARMM[32–34], OPLS[35,36] or AMBER[37–39], are developed to reproduce bulk properties of liquids. Therefore, they cannot be straight forwardly applied to simulations of an interface since they might predict artifacts or yield in an unphysical description of the interface. The development of molecule-surface interaction potentials is a complex problem and it has, as we will show in this review, often been unsatisfactorily addressed in the literature. At the current point of development only small steps have been made towards obtaining reliable force fields for interface systems, some of which we will discuss throughout this review. In this framework, we will study ways to develop reliable, representable force fields and analyse potential problems and future challenges.

Generally, an interface force field has to capture the adsorption energy change as a function of the distance, position and orientation of the molecule with respect to the surface. This means, that the relative adsorption strength of the molecule in different conformations on the surface has to be modelled correctly. The conformational phase space at the interface is significantly different than the one in the bulk and only if the model can capture this complex adsorption energy landscape, the correct enthalpic and entropic description of the interface is guaranteed. Essentially, there are two routes to obtain interfacial force fields: Firstly, the force field is parameterised based on experimental information on interface properties[40–43] or secondly, the parameterisation is based on quantum chemical (QC) information of the near-surface conformations and corresponding adsorption strengths of the molecules on the surface[1–20]. We not that in this review, we will neither discuss force fields, which are based on the fitting of experimental information, nor force fields for organic-inorganic interfaces in biomineralisation processes[24,26,44–54] since they are using parameterisation approaches, which are not based on QC information.

In the case of force fields that are parameterised based on experimental information on macroscopic properties it it not a priori clear how local properties, such as conformations of the adsorbents and the relative adsorption strengths of different conformations, are captured. On the contrary, these local properties can be described quite accurately by QC calculations, although one might argue that the computed absolute energies are strongly dependent on the method that is used for the QC calculations. However, the *relative* adsorption energies between different conformation are less dependent of the QC method, as we will see in section 1.3.1.1. It is crucial in an MD simulation that these relative energies between different adsorption states (the energy barriers) are correctly described in order to guarantee a correct sampling of the near-surface region. Since QC calculations can give a qualitatively good description of conformations and corresponding energy barriers, a dual-scale quantum-classical modelling approach has often been the method of choice in the past. However, due to computational limitations of the electronic structure calculations, QC data on only a finite number of conformations can enter the fitting routine. This finite amount of conformations have to be chosen carefully since an insufficient or unrepresentative sample of QC information might bias the resulting force field such that other adsorption states cannot be predicted correctly. Subsequently, a classical simulation using these force field may provide unrealistic and unphysical predictions. In previous work, electronic structure information, that enter the parameterisation, included details about the global minimum adsorption state or distance dependent information of the adsorption strength of the molecule with respect to a few positions or atomic sites on the surface [2–15,20] and thus it is not a priori clear if the resulting force fields are representable enough to predicting the full adsorption energy landscape correctly. In this work, we will address this issue and extract potential problems and challenges that are related to the parameterisation procedure. Important aspects are e.g. the amount of QC information as well as the nature of the force field (e.g. the analytical form of the potentials, the treatment of the charges or the modelling of the surface). Furthermore, the validation of the force fields is an important aspect, which has often been neglected in the past.

Moreover, the quantum-classical modelling approach has mainly been applied to parameterise the interaction between small molecules, like water or small biomolecules, and metal or metal oxides. [1,2,6–8,11,12,14,15,17,20]. However, in many systems, in which macroscopic properties are determined by the interfacial interaction and morphology, the adsorbents are macromolecules. In implantology, bio-

inspired materials, polymer coatings or wetting phenomena of complex fluids, the important phenomena happen at the interface and they have often been insufficiently understood. Since the quantum-classical parameterisation can also be applied to model macromolecules on surface, as we will see in section 1.3.3, this approach can be used to make progress in this field. In a so called building-block approach, the macromolecule is divided into small sub-molecules, whose interaction with the substrate is then separately parameterised.[3,4,9,19] Especially, for macromolecules it is important to capture the relative adsorption strengths of the different functional building-blocks of the macromolecules to obtain a correct microscopic picture of the near-surface morphology.

The review is structured as followed: Firstly, in section 1.2, we will analyse the different state-of-the-art quantum-classical modelling approaches. This section is subdivided into two parts. Section 1.2.1 will review the QC information that enter the fitting routine and section 1.2.2 discusses the classical force field that is used to describe the molecule-surface interactions. Secondly, in section 1.3, we will summarise the major challenges in this field and present possible routes to obtain reliable force fields. Section 1.4 will sum up the work.

1.2 Quantum-classical modelling approach

The atomistic modelling of molecule-surface interactions is a non-trivial problem. Standard atomistic force fields like GROMOS[29–31], CHARMM[32–34], OPLS[35,36] or AMBER[37–39], are not suitable to model interfacial interactions since they are parameterised on bulk properties of liquids. Therefore, new potentials have to be developed that can describe the interaction between the molecule and the surface in such a way that it ensures a correct sampling of the underlying adsorption energy landscape. In the past, a so called quantum–classical modelling approach has often been applied to developed molecule–surface interaction potentials. The parameterisation of the force fields is based on QC calculations on adsorbed structures and the corresponding energies.[1–20] We will explain in following paragraph how the quantum-classical modelling is carried out.

In Fig. 1.1 a commonly applied fitting procedure is schematically presented. In a first step, QC calculations of a given numbers of conformations of the molecules of the surface are performed. The conformations of the adsorption states are then used in a classical simulation, where the classical adsorption energies are calculated

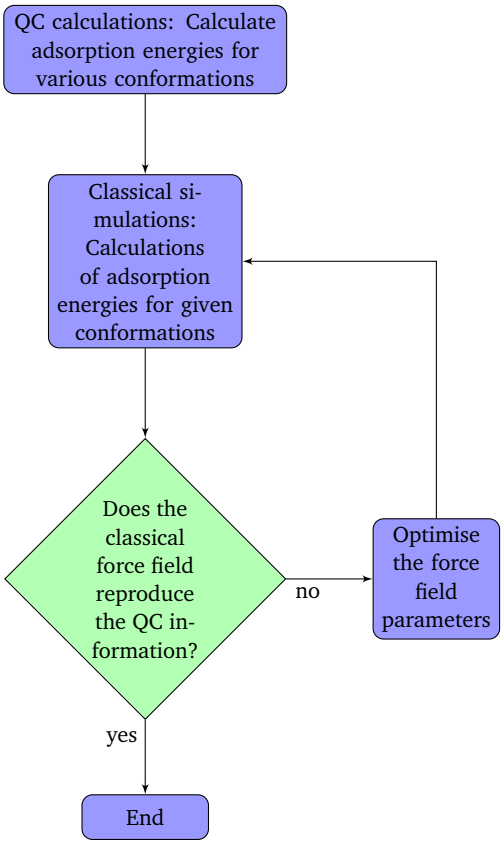

Figure 1.1: Schematic representation of the quantum-classical modelling of molecule-surface interactions.

and compared to the ones obtained by QC calculations. If the QC and the classical simulation results differ, the classical force field has to be refined and optimised until agreement is reached.

The method is applicable to a wide range of systems and is not restricted to a specific type of QC calculation, e.g. Hartree-Fock (HF), post-HF methods, density functional theory (DFT) or the DFT based finite-electronic temperature method (FEMD). The nature of the classical force field (e.g. the analytical form of the potentials, charge polarisability effects or the modelling of the surface) can be chosen freely. In Tab. 1.1 we have listed a selected number of representative publications, in which the developed molecule-surface interaction potentials are based on a quantum-classical modelling approach. We list details of the QC information that enters the fitting procedure as well as details of the form of the classical force field. We can see from a first comparison that there are significant differences not only in the QC information that enter the fitting routine but also in nature of the classical force field. This diversity shows that at current point of development no clear strategy and no systematic ap-

Ref.	System	QC Information		Classical FF		
		method	type	potential	charges	polarisability
McCarthy 1996 [1]	H_2O on MgO	periodic HF	distance dependences in different orientations and positions	Buckingham	yes	no
Borodin 2003 [3]	polyethylene oxide on TiO_2 (CH_3OCH_3 on TiO_5H_9)	MP2	distance dependence	exponent and LJ(12-6)	yes	yes
Bandura 2003 [2]	H_2O on TiO_2	DFT	vibrational frequencies	Buckingham	yes	yes
Schravendijk 2005 [5]	benzene on Ni(111) and Au(111)	FEMD	distance and inclination dependence	LJ(10-4), Morse	no	no
Lopes 2006 [55]	H_2O on silica	DFT, HF	minimum interaction energies and geometries	LJ(12-6)	yes	no
Alexiadis 2007 [56]	Alkanethiol on Pt(111), Ag(111) and Au(111)	FEMD	minimum energy geometries	LJ(12-3)	no	no
Cole 2007 [8]	H_2O on oxidised Si	DFT	distance dependence	LJ(12-6), LJ(12-10)	yes	no
Schravendijk 2007 [9]	hydrated amino acids on Ni(111)	FEMD	minimum energy geometries	LJ(10-4), Morse	no	no
Ghiringhelli 2008 [13]	hydrated peptides on Pt(111)	FEMD	distance dependence	LJ(10-4)	no	no
Iori 2008 [12]	proteins on Au(111)	MP2	minimum energy geometries	LJ(12-6)	yes	yes
Youngs 2009 [14]	isopropanol on γ-Al_2O_3	DFT, HF	minimum energy geometry	LJ(12-6)	yes	no
Herbers 2011 [17]	water on ZnO(0001)	DFT	lateral dependence	LJ(12-6)	yes	no
Johnston 2011 [16]	benzene on Au(111)	DFT	distance dependences	LJ(12-6), Morse	no	no
Schneider 2011 [15]	hydrated biomolecules on oxidised TiO_2	DFT	distance dependence	LJ(12-6), LJ(9-3)	yes	no
Johnston 2012 [18]	ethanol on α-Al_2O_3	DFT	distance and lateral dependence	LJ(12-6)	yes	no

Table 1.1: Overview of a selected list of publications where the molecule-surface interaction potentials are obtained by a quantum-classical modelling approach.

proach for modelling molecule-surface interactions is present. Despite this diversity at first glance, we will try to extract similarities and differences and based on that extract challenges and propose systematic modelling solutions. In order to do so, we will firstly, in section 1.2.1, review the QC information that has been used in the fitting procedure to discuss in a second part, section 1.2.2, the nature of the classical force field that has been applied.

1.2.1 Quantum chemical information

In this section we will focus on the QC information that enters the fitting procedure. By discussing a few representative examples from the literature, we will analyse how

many and what type of QC information has been used in the previous reports (listed in Tab. 1.1).

Schneider and et al. studied water and small biomolecules on titanium dioxide in aqueous solutions.[15] The interactions of the molecules with the surface are based on a distance dependent adsorption energy curves with respect to one surface site. The classical interfacial pair potentials were fitted such that they reproduce the distance dependent QC curve. Bandura et al. proposed a different force field that describes the interaction with water on titanium dioxide.[2] In comparison to the work of Schneider et al., it is based on a fitting to certain adsorption geometries of small clusters of $Ti(OH)_4(H_2O)$ and does not take into account a full periodic description of the surface.

The work of Borodin et al. is also based on QC calculations of small clusters. In their work, the interaction between poly(ethylen oxide) and titanium dioxide is modelled by a small cluster of dimethylether (CH_3OCH_3) and TiO_5H_9. A distance dependent adsorption energy curve is used for the quantum-classical fitting approach. McCarthy et al. studied water on magnesium oxide.[1] They have taken a full periodic representation of the surface into account, where they studied the distance dependence of the adsorption of water on magnesium oxide with respect to a five different conformations of water on different surface sites. By doing so, they probed the surface in five different lateral positions on the surface, which means that lateral surface heterogeneities are accounted for, and they combined this with distance dependent information on the adsorption energy landscape.

Iori et al. have developed a quite complex force field that can describe the interaction between different proteins with Au(111) surface.[12] The force field is developed, along with the parameterisation on experimental desorption energy data, based on QC mechanical calculations of small molecules on Au(111). They obtained interaction energies and the corresponding adsorption geometries for each of the different molecules and fitted the classical force field such that these energies and geometries are reproduced. Johnston et al. have developed force fields for benzene and polystyrene on Au(111).[16,19] The parameterisation is done based on distance dependent adsorption energies of the molecules in various conformations and positions on the surface. Alexiadis et al. have proposed a force field to describe the interaction between alkenethiol and Au(111), Ag(111) and Pt(111).[56] The most favourable adsorption sites and geometries of methanthiol on the three different metals were taken into account in the parameterisation.

Lopes et al. have studied the interaction of water with quartz and have developed a force field that is compatible with the CHARMM force field.[55] Along with experimental information, they have parameterised the nonbonded interaction potentials based on minimum interaction energies and geometries. The interaction of water with an oxidised Si surface is modelled such that it reproduces distance dependence of a single water in two different conformations on the surface.

In our previous work, we have studied the adsorption of water on a zinc oxide surface.[17] We have calculated a wide range of about 200 adsorption energies, which correspond to different lateral conformations and orientations of water in different orientations on the surface. Furthermore, we developed a classical force field for ethanol on α-alumina based on a complex set of lateral and distance dependent conformations (involving 174 distinct conformations). This complex picture of the adsorption energy landscape that enters the fitting routine is contrasted with the work of Youngs et al., who have studied isopropanol on γ-alumina[14], the force field of which is developed based on one adsorption state of isopropanol on α-alumina.

In summary, one can conclude that the fitting is either performed based on distance dependent conformations and/or conformations at different surface sites. In some cases the force field has been developed based on only a single conformation of the molecule on the surface. The adsorption energy of a molecule on the surface is highly distance-, site- and orientation dependent. The interface force field should capture these three contributions. However, only a limited number of QC calculations can be performed. Consequently, the question arises which set of QC information has to enter the fitting routine in order to get reliable, representable force fields. This issue will be addressed in section 1.3.

1.2.2 Classical force field

In this section we will discuss the nature of the classical force fields that have been used in the past by analysing which potential forms have been applied and how electrostatic interactions have been taken into account. Detailed information for a selected number of publications are presented in Tab. 1.1. The classical interfacial force fields often contain pair potentials to describe the interactions between the adsorbent and the surface. Lennard-Jones (LJ) 12-6 potentials[12,14,17,18,55] or other potential forms[1–3,5,9,13,15,16,56], like the Morse potentials, Buckingham potential or other LJ exponential forms, can be found in the literature. The electrostatic interaction between the adsorbent and the surface often plays an important role as well. Especially,

in metal oxide systems, the interfacial interaction is dominated by Coulomb interactions. In most approaches, partial charges have been assigned as point charges to surface atoms, which were calculated using QC methods.[1–3,8,12,15,17,18,55] Beyond this, some force fields are also capable of modelling polarisability effects and thus capture the influence on the electrostatic surface potential in absence or presence of the adsorbent.[2,3,12]

From previous studies, as shown in Tab. 1.1, we cannot identify a correlation between the choice of the potential form and the systems studied in the literature. Similar systems are modelled differently and no systematic approach can be found. In principle, the nature of the specific interaction between the adsorbent and the surface should determine the choice of the potentials form. The LJ potential for example has a very steep and therefore "hard" repulsive part r^{-12} (see eq. 1.1), whereas the Morse potential has a much "softer" repulsive part, which is due to its exponential decay ($exp(-r)$) at small interatomic distances r (see eq. 1.2).

$$V(r) = 4\epsilon \left(\left(\frac{\sigma}{r} \right)^{12} - \left(\frac{\sigma}{r} \right)^{6} \right) \tag{1.1}$$

ϵ denotes the LJ well and σ is the LJ diameter.

$$V(r) = D_e \left(1 - exp\left(-a(r - r_e)\right)\right)^2 \tag{1.2}$$

r_e is the equilibrium bond distance, D_e the well depth and a is related to the width of the potential.

It has been shown in the past that the Morse potential can describe the adsorption of molecules, especially aromatic molecules, on pure metals or transition metals quite well.[5,9,18] For example, in the case of benzene adsorbing on Ni(221) an electron density transfer from the delocalised metal and benzene electrons can be observed.[57] In Fig. 1.2 this electron density transfer is schematically presented. Yellow and red indicate areas from which electron density is taken away and blue and green indicate ares to which electron density is transferred. Delle Site et al. found, as shown in Fig. 1.2, that electron density transfer takes place along the Ni-C bonds. A suitable potential form for describing a bonding situation, which is in this case induced by this short-range charge transfer, is a Morse potential. The work of Johnston et al. is another example which shows that the classical potential should

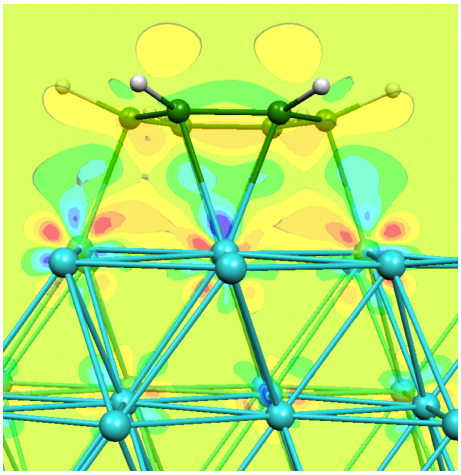

Figure 1.2: Adsorption of benzene on Ni(221). Schematic representation of the electronic density difference as calculated in Ref. [57]. Yellow and red indicate areas from which electron density is taken away and blue and green indicate areas to which electron density is transferred.

be chosen such that it represents the nature of the interaction.[16] They studied the adsorption on benzene on Au(111) and compared how well the LJ 12-6 potential and the Morse potential can describe the adsorption energy as a function of distance away from the surface. Also here a Morse potential turned out to be the better choice to capture the benzene-Au(111) interaction.

Commonly, the metal or metal oxide surface is represented atomistically and the interaction between the surface and the molecule is modelled using pair potentials, as discussed before. However, in the work of Schravendijk et al., Ghiringhelli et al. and Alexiadis et al. where the interaction between amino acids, small peptides or thiol derivatives with different metals are modelled[5,9,13,56], the surface is described as a flat wall and interaction is described with distance dependent potentials. This approach is only valid under the condition that lateral surface heterogeneities do not play an important role. We will further discuss this in section 1.3.1.

1.3 Discussion and challenges

In general, the classical force field that is obtained by a quantum-classical modelling approach should be tested after the parameterisation to check for its representability, which is the ability to predict adsorption states different from the one the force field is fitted on. In the current state-of-the-art work, the validation of the classical force field is often not taken into account. On the one hand, we have demonstrated in previous work, that the force fields, which are fitted on only one

or a few adsorption energies and conformations, like the force field of Youngs et al.[14], cannot predict the adsorption energy landscape correctly.[18] On the other hand, in the work of Bandura et al. the fitting on only a few conformations or using small clusters of the interfacial system instead of the full periodic description resulted in a representative force field.[2] Alimohammadi et al. have shown that this force field, despite the simplified representation of the interface on the quantum level, is capable of predicting correct binding energies and conformations for molecular adsorption on different modifications of titanium dioxide.[58] Consequently, the following question arises: How much QC information on conformations and adsorption energies is needed to obtain reliable force fields and what is the computationally most efficient way? What approximations can be made throughout the fitting routine and how accurate do the QC calculations need to be? We will address all of these question in this section.

The QC calculations are the most time consuming step or in other words the bottle neck of the quantum-classical modelling approach. Therefore, one aims at reducing the number of QC calculations. However, one has to keep in mind that a finite sample of conformation and corresponding adsorption energies can only then result in a realistic description of the molecule-surface interaction if this sample is representative with respect to underlying adsorption energy landscape. This guarantees that adsorption states, which are different from the ones that are used in the fitting procedure, can be predicted correctly. In section 1.3.1 we will discuss how to improve upon the representability of the classical force fields. Furthermore, the optimisation and automatisation of the modelling approach is an important aspect to consider to make the fitting as efficient as possible, which will be addressed in section 1.3.2. In the last part (section 1.3.3) we will discuss if and how macromolecules in contact with surfaces can be modelled.

1.3.1 Representability of the classical force field

The representability of the parameterised classical force field is a central problem in the quantum-classical modelling approach. In order to obtain reliable force fields, one has to be very careful in choosing the subset of QC information that enters into the fitting routine. Since the classical model has to describe the adsorption energy change as a function of the distance, position and orientation of the molecule with respect to the surface, one would intuitively choose a subset of QC data that capture

all three dependences. However, in the current state-of-the-art work this obvious consideration has most of the time not been made. As shown in section 1.2.1, classical force fields are in some cases parameterised on only one or a few conformations. The representability of the force field is often not tested after its parameterisation and the question remains how representable the classical force field in fact are.

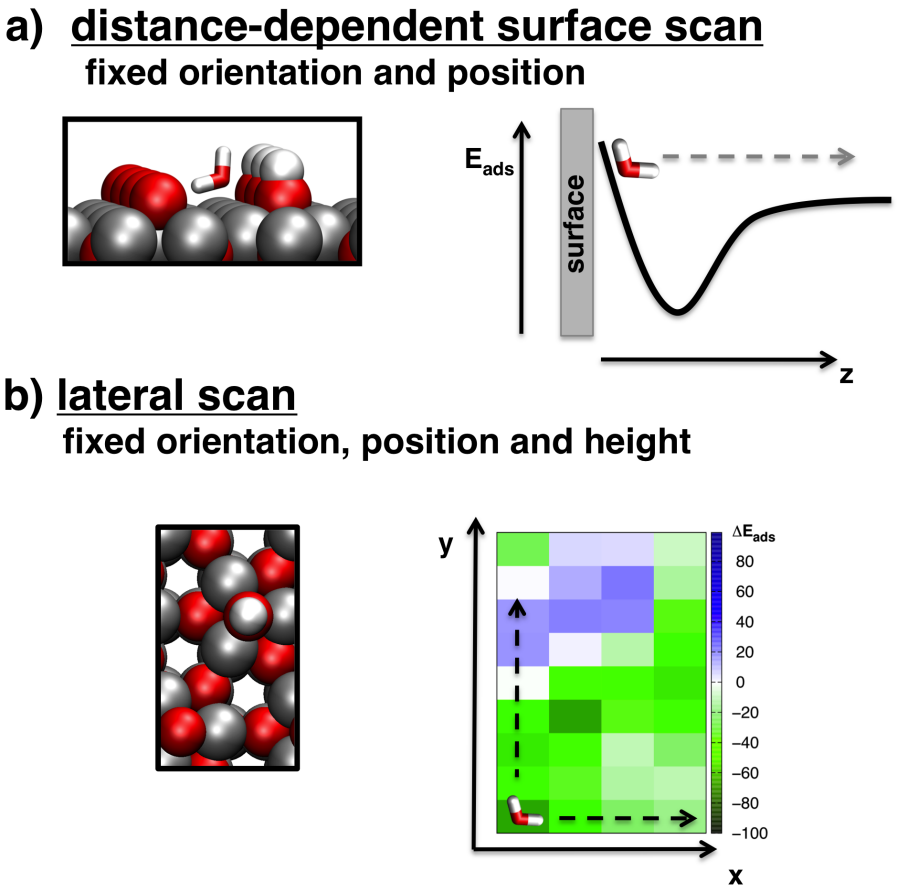

Figure 1.3: Schematic representation of the distance-dependent scan of the adsorption energy landscape (at a fixed orientation and surface site of the molecule) and a lateral scan across the surface (at a constant height from the surface).

In previous work, we have shown that reliable classical force fields can only then be obtained if the QC data are representative with respect to the underlying adsorption energy landscape.[17,18] This means that short- and long-range conformations, which include high and low energies, should be taken into account in the fitting procedure. However, the number of different conformations should ideally be as small as as possible, since the QC calculations are computational expensive. In section 1.2.1, we have shown that in the past, different conformations can be obtained in two ways: A lateral surface scan at a constant height of the molecule with respect to

the surface and distance-dependent scans of the molecule at a fixed orientation and position with respect to the surface. In Fig. 1.3 both approaches are presented in a schematic way. It is exemplary shown for water in contact with zinc oxide, which we have studied in previous work.[17] The distance-dependent probing of the adsorption energy landscape is shown in 1.3a), which is obtained by moving the molecule away from the surface. By laterally moving the molecule across the surface one can map out the adsorption energy at a constant distance from the surface and gain insight into lateral heterogeneities on the surface. A schematic representation of such a adsorption energy landscape is shown in 1.3b).

The choice of whether to fit to a lateral surface scan or to a distance dependent sample of QC information or on a combination of both is to some extent related to the scientific question, that the classical atomistic simulation should address, as well as to the complex nature of the interfacial interaction. In previous work, we have discussed this issue by studying the parameterisation procedure of two different systems: water on zinc oxide[17] and ethanol on alumina[18]. For the first system, we have performed a lateral surface scan using DFT calculations, which result in a sample of 198 distinct conformations of water on ZnO in different lateral positions and orientation. We have divided this full sample into three subset of around 70 conformations: The first one contains only conformation that have very negative adsorption energies (strong adsorption), the second one only conformations that have higher energies (weaker adsorption) and the third subset includes high- and low-energy conformations. We studied the representability of the classical force fields obtained by fitting on these three subsets. As expected, only the third subset results in a classical force field that can predict the adsorption energies of the 198 different conformations accurately. In order to get a feeling for the performance of the force field that is fitted on the high- or the low-energy subsets, we show in Fig. 1.4 the difference in adsorption energies between DFT and classical simulations. The force field is fitted on 70 conformations with low energies. The white and weak-coloured grid points correspond to the conformations that are used in the fitting procedure. Turquoise, orange and blue grid points represent deviations of the classical adsorption energies from the DFT reference. The root mean square deviation of the energy difference between the DFT and classical adsorption energies is 39 kJ/mol, in which the conformations that are predicted as very low adsorption energies (shown as blue grid points) make the biggest contribution. This might lead to an unphysical sampling in a subsequent molecular simulation and therefore to

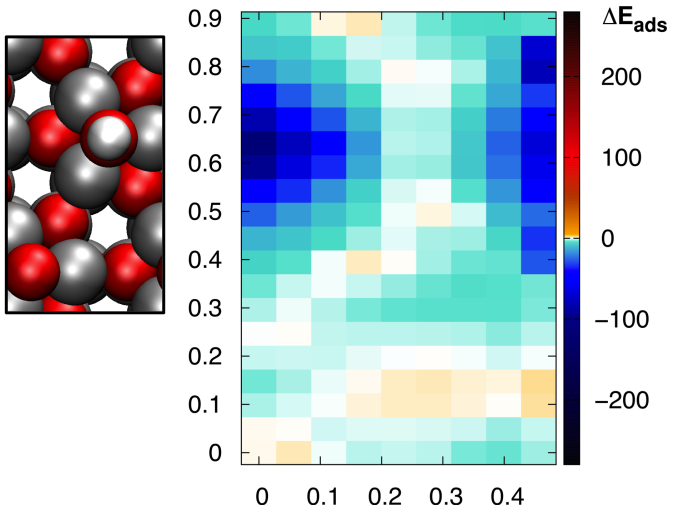

Figure 1.4: Differences in adsorption energy $\Delta E_{ads} = E_{DFT} - E_{class.}$ in kJ/mol. The classical force field is fitted on a subset of low energy structures.[17] The white and weak-coloured grid points correspond to the conformations that are used in the fitting procedure. Turquoise, orange and blue grid points represent deviations of the classical adsorption energies from the DFT reference.

wrong prediction of macroscopic properties. Only a balanced sample of high- *and* low-energy conformations guaranteed a representable force field.

In a second study, we have taken the previous work one step further and compared the representability of different force fields for the interaction between ethanol and alumina that are fitted on either three different distance dependent scans (as shown in 1.3a)), one lateral surface scan (as shown in 1.3b)) or a combination of both consisting of 174 distinct conformations.[18] We refer to Ref. [18] for detailed information about the fitting procedure. In Fig. 1.5 and 1.6 the DFT and classical energy landscapes (fitted on one lateral surface scan and three distance dependent scans) at two different heights of the molecule above the surface are shown. The classical force field, discussed in Fig. 1.5, is fitted on the lateral surface scan at a distance, which corresponds to $z = 0.39$ fractional units (details can be found in Ref. [18]). Unsurprisingly, the classical force field can reproduce the DFT energy landscape at that distance in a qualitatively good agreement (compare Fig. 1.5c) and d)). However, the adsorption energies of conformations in closer proximity to the surface cannot be described correctly. In fact, repulsive conformations (blue grid points in Fig. 1.5a)) are predicted as attractive adsorption states (blue grid points in Fig. 1.5b)). In Fig. 1.6 the representability of the force field that is fitted on three different distance-dependent surface scans is evaluated. This sample of conforma-

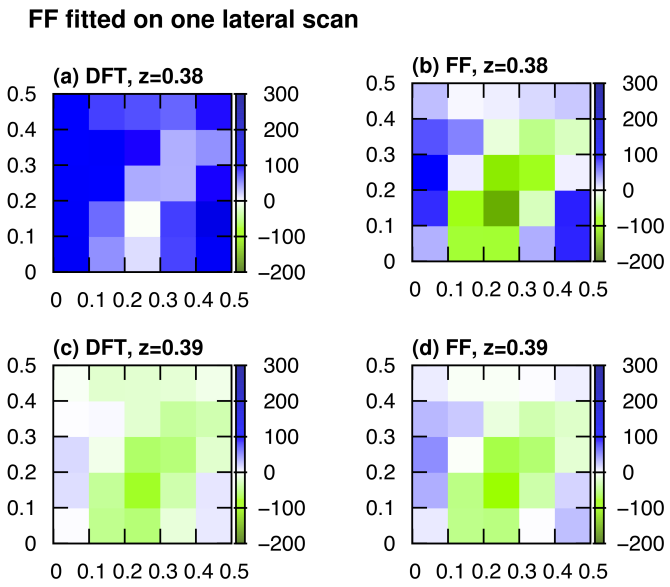

Figure 1.5: Comparison of the DFT adsorption energy landscapes with ones obtained by a force field (FF), which was fitted on one lateral DFT surface scan at z=0.39 fractional units (DFT energy landscape shown in b)). Details can be found in Ref. [18]. The energies are reported in kJ/mol.

tions contains distance dependent information as well information on the adsorption strength on three different surface sites. The resulting classical force field can predict the adsorption energy landscape in good agreement with the DFT reference at both distances from the surface. Especially striking is that the good qualitative agreement of the energy differences between different adsorption sites. The pattern of the classical energy landscapes are very similar to the DFT one, compare Fig. 1.6a) with b) and Fig. 1.6c) with d). This is especially important since this ensure a correct sampling of the near-surface conformational energy barriers. Overall, this shows that the QM data sample should not only contain a balanced mixture of low-and high-energy conformations, as shown in the previous paragraph, but furthermore information about the distance dependence of the adsorption energy as well as the molecule's position and orientation with respect to the surface is important. Only this guarantees representable classical force fields. We note that the fitting on a complex set of adsorption energies corresponding to 174 conformations is computationally less feasible and we found that the fitting on a smaller subset of representative QC information provides the best compromise between computational efficiency and quality of the force field.

In other examples, as seen in section 1.2.1, of Schravendijk et al., Alixiadis et al. and Ghiringhelli et al. the interaction of aminoacids, small peptides and alkanethiols

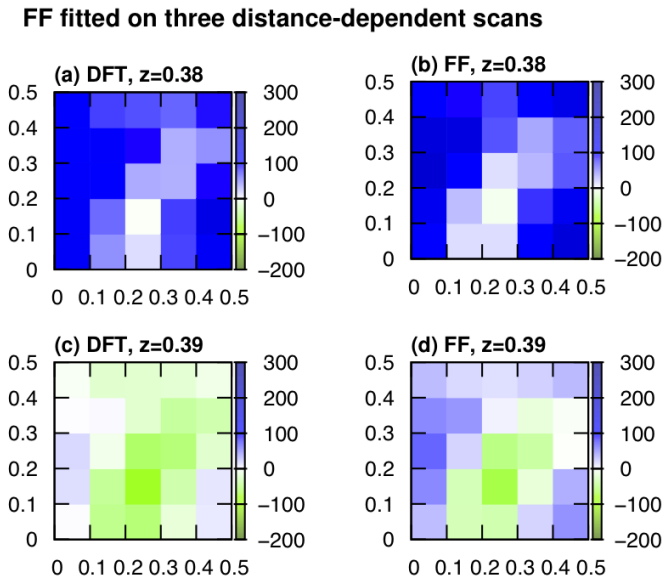

Figure 1.6: Comparison of the DFT adsorption energy landscapes with ones obtained by a force field (FF), which was fitted on three distance-dependent surface scans. Details of the different conformations that were used can be found in Ref. [18]. The energies are reported in kJ/mol.

with metals by are modelled neglecting lateral surface heterogeineities and approximating the surface by a flat wall.[5,9,13,56] This approximation is only valid if the adsorption energies at different surface sites are similar. However, this has to be checked carefully since previous studies of Johnston et al. have shown that such energy differences between adjacent adsorption sites can be of the order of tens of kJ/mol for the benzene interaction with Au(111).[16,19]

1.3.1.1 Quantum chemical calculations of adsorption conformations

In general, one aims at obtaining an accurate description of the electronic structure of the molecule in contact with the surface. Therefore, post Hartree-Fock or DFT methods with large basis sets have been applied in the past. In this way more and more accurate values of the absolute energies are obtained. However, for the classical interface force field it is important that the relative energies between different conformations is described accurately such that a correct classical sampling at the interface is guaranteed. While these absolute energies are strongly dependent on the method, the functional or the basis set, the relative energies between the different adsorption states are less strong influenced by these factors. Johnston et al. have demonstrated this in an extensive DFT study about phenol adsorption on

Si(001).[59] They have considered eight different adsorption states and calculated adsorption energies by using five different DFT functionals or basis set. We refer to Ref. [59] for further details. The adsorption energies for the different the DFT functional are reported in Tab. 1.3.1.1. We note that conformation A and B are the only non-dissociating conformations. For these two conformations the absolute energies can vary up 0.47 eV (for conformations C-H the variation of the absolute energies is even bigger), whereas the relative energy differences between two conformations calculated with different functionals are quite similar for all five functionals. For the other dissociative conformations C-H the absolute and relative energies scatter slightly more depending on the functional. Nevertheless, it is important to note that the energy barriers between the different conformations are still qualitatively captured for all five DFT functionals or basis sets, respectively.

A correct sampling of the different conformations and adsorption strengths are especially important in systems containing multiple adsorbents or macromolecules. The local conformation at the interface is determined by the local adsorption strength and therefore by the competitive ad- and desorption of different functional subunit of the molecule or different molecules as such. The overall chain conformation on the surface can furthermore only be represented correctly if the *relative* adsorption energies of chain subunits in different local conformations are predicted accurately by the QC approach. We discuss the application of the quantum-classical modelling approach to macromolecular systems more detailed in section 1.3.3.

We note that for some interfacial systems, it has been shown that it is important to account for van der Waals interactions, which are standardly not taken into account.[18,19,68–72] Especially for electronically highly conjugated systems the DFT calculations using the van der Waals corrections have proven to be more accurate.[68,70,72]

1.3.2 Automatisation and optimisation of the fitting routine

In the quantum-classical modelling approach, the fitting is often done based on many QC data on conformations and corresponding adsorption energies and it involves the optimisation of a relatively big set of pairwise interaction potentials. Therefore, it is especially for complex systems not feasible to perform the fitting manually so that an optimisation routine has to be applied to obtain a reliable set of force field parameters. Previously, a local minimisation technique, which searches for the optimal set in a given parameter phase space, has successfully been applied to

	PW91[a]	PBE[b]	revPBE[c]	PBE[b] LCAO[e]	B3LYP[d] LCAO[e]
A	1.06	1.01	0.57	0.97	0.66
B	1.27	1.24	0.75	1.26	0.80
C	2.96	2.88	2.65	2.87	3.00
D	2.38	2.30	2.09	2.32	2.58
E	2.61	2.52	2.04	2.47	2.41
F	3.89	3.78	3.20	3.81	4.29
G	5.85	5.68	5.03	5.18	5.52
H	4.82	4.64	4.13	4.40	4.92

a [60]

b [61–63]

c [61,64,65]

d [66,67]

e linear combination of atomic orbitals

Table 1.2: Adsorption energies of phenol on Si(001) calculated with different DFT functionals taken from Ref. [59]. Conformations A-H denote different adsorption states, details can be found in Ref. [59]. All energies are given in eV.

such force field fitting problems.[1,2,15,16] These local optimisation techniques often require an educated guess for the initial parameters, which is close to a local or the global minimum. However, such an initial guess is sometimes not possible, especially when the nature of the interaction is unknown. Global optimisation techniques can provide a way to explore the full parameter phase space and converge to an optimal set of parameters in a fast and efficient way. In previous work, we have shown that a genetic algorithm has proven to be a useful global optimisation algorithm that can deal with such complex fitting problems.[17,18] It is especially useful, since no prior knowledge about the parameters is needed. In any case the optimised force field should be validated after the fitting in order to guarantee that the force field is representable enough to predict the correct adsorption energy landscape. However, since a global optimisation allows for fitting on multiple conformations at the same time, it is more likely that with a representative set of QC data a good representability is reached.

An alternative approach to optimise the fitting procedure was proposed by Schravendijk et. al.[9] In Fig. 1.7 this procedure is schematically shown. Firstly, the classical force field is developed based on only a few QC calculations (as presented in section 1.2). Then classical simulations are used to overcome barriers and

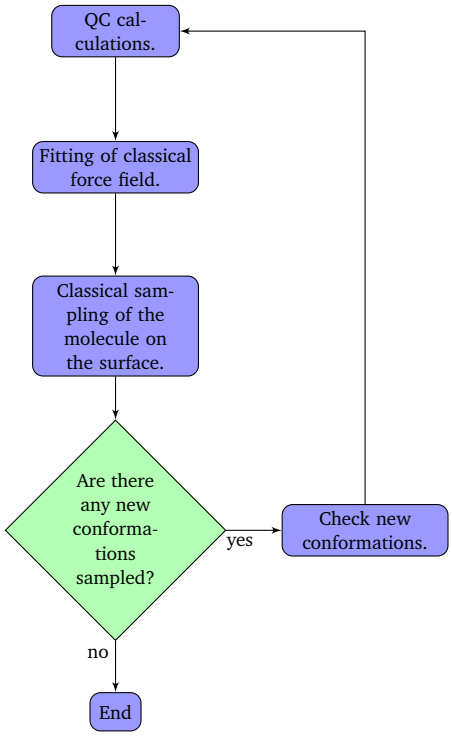

Figure 1.7: Schematic representation of the feedback loop of conformations from the classical FF simulations to QC calculations. [9]

sample further conformations close to the surface. In the case that new conformations, which have not been considered in the initial parameterisation, are sampled, a so called feed back loop is introduced: In an electronic structure calculation it is tested if the conformation is stable and energetically favourable. Based on this criterium the classical force field has to be refitted or not. This approach is very computationally economic, since the number of QC calculations can be minimised by applying a feedback loop. In this way the classical force field is obtained in an iterative and self-consistent way, which results in force fields that predict conformations close to the surface and the corresponding adsorption energies in agreement with QC calculations. Schravendijk et al. applied this iterative scheme to model alanine on nickel (see Fig. 1.8) After fitting an initial force field, they found in the classical sampling adsorption states where the amino nitrogen and carboxylic oxygen of the amino acid are equally strong binding to the surface. However, QC calculations of this conformation showed that the classical force field wrongly predicted this binding state which was actually a nonbonding conformation. A modification of the initial force field was applied to ensure that only one interaction site (either the nitrogen or the oxygen) could bind to the surface. This was achieved by introducing a so called

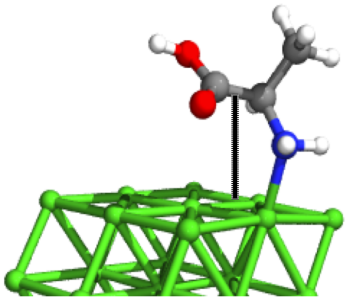

Figure 1.8: Binding conformation of alanine on nickel. The dashed line indicates the repulsive point for the seesaw potential. [9]

seesaw potential, a repulsive site at a position between the nitrogen and the oxygen (shown in Fig. 1.8).

1.3.3 Application to macromolecular systems

In the past, the quantum-classical parameterisation has mostly been used to model systems where the adsorbent is either water or a small organic molecule. In fact, it is not straight forward to apply this methods to systems with bigger adsorbents, like polymers or complex biological macromolecules, since the length scale of the system is limited by the QC calculations. However, most of the interesting and important systems, where interfacial interactions strongly determine the macroscopic properties, are systems containing macromolecules. Polymer coating systems, lacquers, paints, implants or bio-inspired materials are only a few examples. In oder to tackle this problem, Delle Site et. al. have proposed a so called building block approach [4]. Similar approaches were for example used by Borodin et al. model the interaction between polyethylene oxide and TiO_2 [3], Schravendijk et. al. who studied amino acids on metal surface [9] and Johnston et al. who have developed a force field for polystyrene on Au(111) [19]. In this approach, the macromolecule is divided into smaller chemical subunits (the so called building blocks), the interaction of which with the surface can be parameterised separately. Later, these resulting parameters are combined again in order to model the whole macromolecule on the surface. As we discussed earlier in section 1.3.1.1, it is especially important to capture the correct difference in adsorption strength of the chemical subunits in different local conformations. This guarantees that the local conformations at the interface is modelled correctly, which is crucial for a correct prediction of macroscopic proper-

ties. A good example for the importance of a realistic description of the complex entropic and enthalpic interplay of the molecule close to the surface has been given by Delle Site et al., who studied the adsorption of bisphenol-A-polycarbonat (BPA-PC) on Ni(111).[4,21,22,73] They analysed the complex interplay between adsorption energies and overall chain conformations for different chain-end modifications.[4] They showed that the chemical specificity of the polymer, which is related to the adsorption strength and the adsorption site and geometry, strongly influences the local interface morphology. When modelling macromolecule-surface interactions, one has to keep in mind that the conformational phase space of the different chemical subunits on the surface is limited, since they are normally embedded in a bigger macromolecule. Therefore, only some specific conformations of the submolecules on the surface have to be taken into account in the fitting routine. In doing so, the quantum-classical parameterisation can also be used to model polymers or biopolymers interacting with surfaces and the size limitation that is imposed by the QC calculations can be overcome.

1.4 Summary

Atomistic computer simulations have previously been used to model molecule-surface interfaces. This is a non-trivial problem since commonly used force fields are developed to describe bulk fluid or solid properties and can therefore not be applied to interfacial systems. A quantum-classical modelling approach has proven to be a useful tool to obtain force fields that describe molecule-surface interactions. These force fields have been parameterised on QC information on near-surface conformations and the corresponding adsorption energies. When a molecule approaches the surface, the conformational phase space is limited in comparison to the bulk and the molecule adsorbs with a certain energy to specific surface sites. The interfacial force fields should capture both, the conformational phase space of the molecule and the correct adsorption strength. We have seen that previous work has often laid the emphasis on modelling the correct adsorption strength of only a few conformations, therefore lacking an extensive sampling of the conformational phase space. It is a priori not clear how well these force fields can then describe the full underlying adsorption energy surface. We have presented ways to improve upon representability of the force fields and showed ways to minimising the computational effort by applying an iterative dual-scale modelling approach. We furthermore discussed how the method can be used to model more complex systems, such as macromolecule-surface

interactions. These systems are from an application point of view very interesting systems since many important phenomena happen at the interface. However, they have often poorly been understood. Atomistic simulations have great potentials to answer open questions and provide useful insight in order to model new and improved materials.

2 Modelling molecule–surface interactions: an automated quantum-classical approach using a genetic algorithm

We present an automated and efficient method to develop force fields for molecule-surface interactions. A genetic algorithm (GA) is used to parameterise a classical force field so that the classical adsorption energy landscape of a molecule on a surface matches the corresponding landscape from density functional theory (DFT) calculations. The procedure performs a sophisticated search in the parameter phase space and converges very quickly. The method is capable of fitting a significant number of structures and corresponding adsorption energies. Water on a ZnO(0001) surface was chosen as a benchmark system but the method is implemented in a flexible way and can be applied to any system of interest. In the present case, pairwise Lennard Jones (LJ) and Coulomb potentials are used to describe the molecule–surface interactions. In the course of the fitting procedure, the LJ parameters are refined in order to reproduce the adsorption energy landscape. The classical model is capable of describing a wide range of energies, which is essential for a realistic description of a fluid–solid interface.

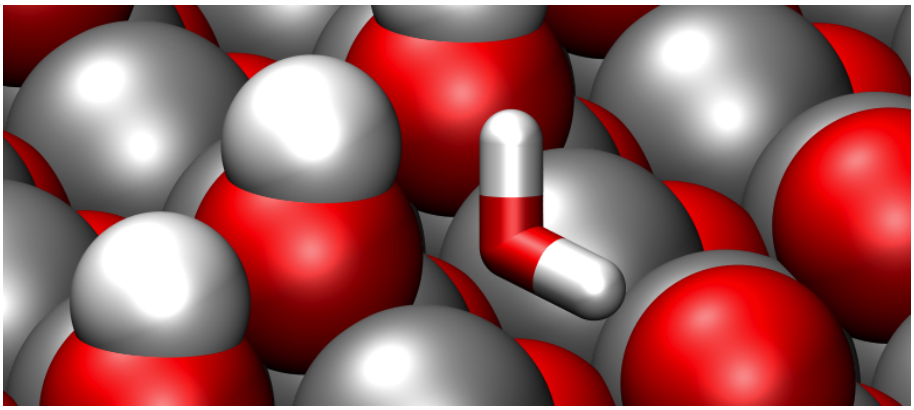

Figure 2.1: A water molecule adsorbed on ZnO(0001).

2.1 Introduction

Surface coatings, biomineralisation, wettability, electrochemical processes, surfactants, catalysis and medical implants are just a few examples where important chemistry happens at the interfacial region[24,74–83]. To understand the influence of the interface on the macroscopic material properties it is essential to have a realistic microscopic description of a fluid–solid interaction. From the perspective of both classical simulations and experiment, a detailed picture of the adhesion of molecules on surfaces is still missing. Molecular modelling techniques are particularly useful in addressing these systems, since they provide a microscopic description of the system of interest.

Classical molecular dynamics (MD) simulations commonly use atomistic force fields that were developed to describe bulk properties of solids or liquids. Intermolecular interactions between different species in the bulk can be modelled by means of simple combination rules. This ansatz is applicable as long as it is validated against some experimental properties. In principle, the same approach can be used to develop fluid–solid interfacial potentials. However, the lack of experimental data describing the interfacial region turns the parametrisation of such surface potentials into a non-trivial problem.

To date, quantum-classical approaches have often been used to model surface interactions. Interfacial potentials have been fitted such that data from electronic structure calculations are reproduced.[1,2,4,5,8,9,13–15] Normally, the data obtained from these calculations include adsorption energies for the minimum energy structure or distance dependent information of the adsorption strength of the molecule with respect to some positions or atomic sites on the surface. In these studies the fitting of the classical potentials is usually based on a fairly limited number of quantum calculations and it is not always clear if the classical potentials obtained in this way are sufficiently transferable to describe the adsorption energy landscape in the x,y-dimension of the surface. In particular for solid-liquid interface systems where this landscape is characterised by a broad spectrum of different energies which are all thermally accessible, new, computationally efficient quantum-classical parameterisation methods need to be considered.

In this work we present a model for a water-ZnO(0001) interaction that is fitted on quantum calculations that attempt to provide a realistic description of the adsorption energy landscape. By doing so, we will demonstrate the importance of the

right choice of the fitted data sample. In order to deal with such a large data set we implemented a genetic algorithm (GA) to automate the fitting procedure.[84] Often, classical interfacial force field parameters are fitted manually. This approach works well for simple systems, but for complicated systems with many atom pairs or many configurations the number of parameters increases rapidly and a manual fit is no longer feasible. A genetic algorithm is well suited for this problem, since it is particularly good at finding the global minimum in a large phase space and, unlike other optimisation techniques, such as local gradient methods, it does not face the problem of getting stuck in a local minimum. Furthermore, an initial starting guess for the parameters is not required, which is particularly important if the nature of the molecule-surface interaction is unknown. While genetic algorithms have been applied to many general optimisation problems and are implemented in other software packages, such as GULP[85] and FFGenerAtor[86], it has never, to the best of our knowledge, been applied to the parameterisation of surface–molecule force fields.

As a benchmark system we have chosen water on a ZnO(0001) ($\sqrt{3} \times \sqrt{3}$) R30°-O+(2x1)-H surface. This surface, which was thoroughly studied by Valtiner and coworkers[87], is stabilized by a partial OH absorption and therefore thermodynamically stable in the presence of water. The electronic structure calculations show no dissociation of water on the surface. The electronic structure and adsorption energy of various configurations of water molecules on the ZnO surface were obtained from DFT calculations. These configurations of water molecules on the surface were used to map out the potential energy landscape of the molecule-surface interaction. The GA was applied to perform a search of the parameter space so that the classical surface potentials reproduce the adsorption energies from DFT. The methodology is presented in detail in section 2.2 and the resulting force field is discussed in section 2.3. We will study the importance of the right choice of the data set, that enters in the GA fitting method.

2.2 Methodology

A schematic representation of the procedure for generating the force field parameters is shown in Fig. 2.2. In the first step an initial set of parameters for the classical force field (FF) is generated. The next step is to calculate the adsorption energy landscape of the molecule in different conformations on the surface using these parameters. The FF and DFT calculations are described in section 2.2.1. The classical energy landscape is compared to the corresponding DFT energy landscape and if the

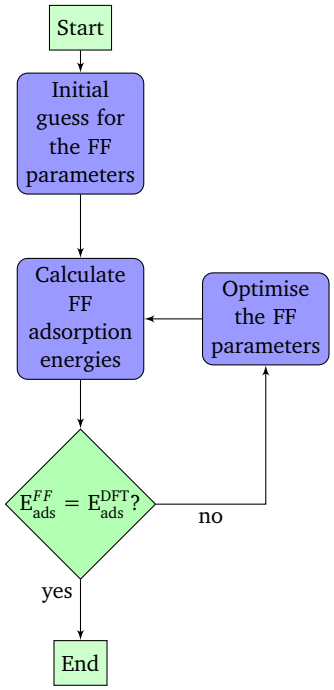

Figure 2.2: Automated procedure to generate classical surface potentials from DFT calculations.

energies differ significantly from the DFT results we refine the FF parameters until the classical and quantum energy landscapes converge. The FF parameters are optimised using a genetic algorithm, which is described in detail in section 2.2.2.

2.2.1 Computational details

DFT calculations: The water–ZnO surface interaction was sampled at 198 evenly spaced positions on the surface. For each configuration the x and y coordinates of the water oxygen atom and the x, y and z coordinates of the surface atoms are held fixed while the z coordinate of the water oxygen and all the coordinates of the water hydrogen atoms are allowed to relax. At each point the structure was optimised using the PBE[61] density functional, PAW[88,89], and a 550 eV plane wave cutoff. The DFT calculations were performed by A. Berezkin *et al.* using the the VASP package[90,91] and will be described in detail in a forthcoming publication[92].

The ZnO(0001) $(\sqrt{3} \times \sqrt{3})$ R30°-O+(2x1)-H surface slab is shown in Fig. 2.3. The ZnO slabs are partially OH-terminated on the surface exposed to water and on the bottom surface the dangling bonds were passivated by pseudo H atoms with the valence of 0.5 e^-. The charge distribution of the ZnO surface is calculated with DFT

by means of modified Mulliken population analysis [93–95]. The partial charges of the surface atoms q_j are obtained from DFT calculations and are shown in Tab. 2.1.

The adsorption energy E_{ads} is defined as

$$E_{\text{ads}} = E_{\text{total}} - E_{\text{slab}} - E_{\text{mol}} \tag{2.1}$$

where E_{total} is the total energy, E_{slab} is the energy of the isolated surface and E_{mol} is the energy of the isolated water molecule. The adsorption energy can be dependent upon the exchange and correlation functional and also on van der Waals forces. In this work the DFT energies do not include van der Waals interactions, however, in a strongly charged system we expect that the electrostatics is the dominant interaction. The 198 configurations cover a range of adsorption energies from around -12 to -55 kJ/mol. The lowest adsorption energy compares well with the experimental results of Schiek *et al.* who studied water adsorption on the H(1×1)O - Zn(0001) surface and found the binding energy of a single molecule to be -55.2 kJ/mol. [96]

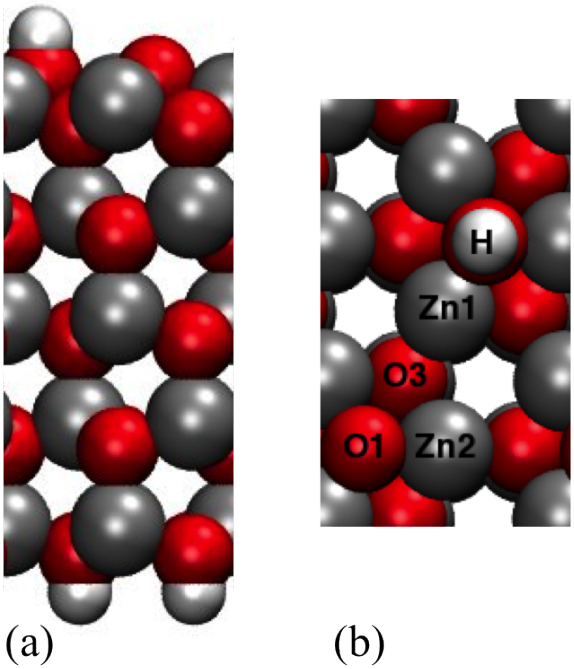

Figure 2.3: The ZnO(0001) $(\sqrt{3} \times \sqrt{3})$ R30°-O+(2x1)-H surface slab viewed in (a) the $y-z$ plane (side view) and (b) the $x-y$ plane (top view). Zn, O and H atoms are coloured in grey, red and white, respectively. The oxygen atom beneath the H is labelled O2. Figure created with VMD. [97]

Classical force field: In order to obtain the water-ZnO adsorption energies for the GA fitting procedure, we performed single point calculations as implemented in the

Layer	Atom	q_j
Top	O1	−0.718
	O2	−0.616
	H	+0.251
	Zn1	+0.760
	Zn2	+0.729
	O3	−0.752
2,3,4	Zn	+0.777
	O	−0.777
Bottom	Zn	+0.740
	O	−0.714
	H	+0.162

Table 2.1: Partial charges for the ZnO slab obtained by Mulliken population analysis. The top surface, which is in contact with the water, is partially hydroxylated and the bottom surface is fully hydroxylated. Each of the central layers is neutral.

GROMACS simulation package[98]. This interaction between the water atoms i and the surface atoms j is described by a potential with a Lennard-Jones 12-6 pairwise nonbonded term and Coulomb term, and has the following form

$$V(r_{ij}) = 4\epsilon_{ij}\left[\left(\frac{\sigma_{ij}}{r_{ij}}\right)^{12} - \left(\frac{\sigma_{ij}}{r_{ij}}\right)^{6}\right] + \frac{1}{4\pi\epsilon_0}\frac{q_i q_j}{r_{ij}}. \tag{2.2}$$

The parameters ϵ_{ij}, σ_{ij} for each type of atom pair are adjusted using the genetic algorithm, which is described in the following subsection. For this system we have six atom pairs, which gives a total of twelve parameters. The nonbonded interactions are cut off at a distance of 0.9 nm. The system is set up in such a way that one water molecule is positioned above a five atomic layer thick ZnO slab, as shown in Fig. 2.3(a). We have used a surface of dimensions 22.794 Å×19.94 Å, which corresponds to 4×2 times the surface unit cell shown in Fig. 2.3(b). Periodic boundary conditions were applied in the x, y and z directions. To avoid image interactions in the z-direction, a vacuum of ≈13 Å is added above the surface. Coulombic interactions were treated with the particle-mesh Ewald (PME) method[99]. The water and surface partial charges were taken from the SPC model[100] and were not modified in the fitting procedure.

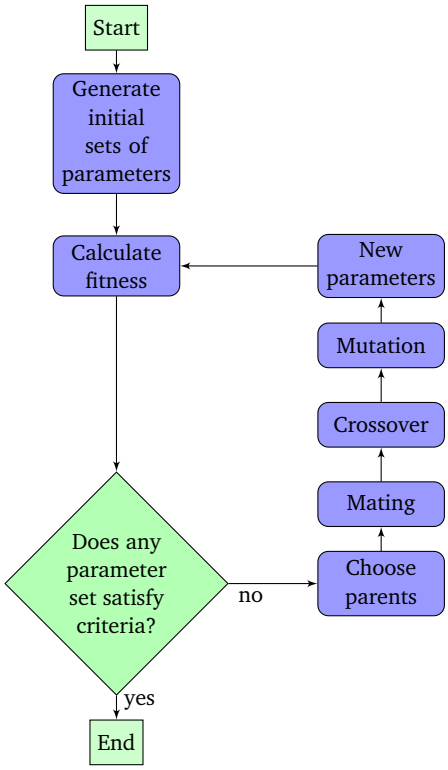

Figure 2.4: Genetic algorithm fitting procedure used to generate classical force field parameters.

2.2.2 The genetic algorithm

The genetic algorithm is based on the principle of evolution, which selects good or 'fit' individuals to be parents and rejects the others. In the present case an 'individual' refers to a particular parameter set and the 'fitness' is the agreement between the classical and DFT energy landscapes. The good parameter sets are then paired 'mated' and they procreate. New sets of parameters are generated, where also 'crossover' and 'mutation' had occurred. The algorithm is shown schematically in Fig. 2.4 and the various terms are described in detail in the text below.

The first step is to generate N sets of parameters. These can be generated randomly since the algorithm will search over all parameter space and does in principle not require an input close to the final results. However, we have chosen the parameters, for convergence reasons, to be in the order of the OPLS-AA force field [36] parameters. The number of sets should be large enough to introduce sufficient variation in the sets and the success of the algorithm depends on N. For each parameter set n we calculate the energy of interaction E^{FF}_{mn} for each single structure m of the total M conformations

of the molecule on the surface. In this implementation the total number of sets is kept constant.

The value that measures the quality of an individual parameter set n is called the fitness, F_n and in our case it depends on the difference between the DFT and classical adsorption energies $\Delta E_{mn} = E_m^{\mathrm{DFT}} - E_{mn}^{\mathrm{FF}}$. The convergence of the method depends critically on the definition of the fitness function. We have used a fitness function of the form

$$F_n = \left(1 - \frac{\Delta_n^2}{\sum_{n=1}^{N} \Delta_n^2}\right)\left(\frac{N}{N-1}\right), \tag{2.3}$$

where $\frac{N}{N-1}$ is the normalisation factor and

$$\Delta_n^2 = \frac{1}{M}\sum_{m=1}^{M} \Delta E_{mn}^2 \tag{2.4}$$

is the mean square deviation of the energy difference. The fitness value ranges from 0 to 1, where $F_n = 1$ corresponds to perfect agreement between the DFT and classical adsorption energy landscapes.

The next step is the selection process, which accepts sets with a certain probability P_n that is based on the fitness. The probability depends on the fitness function as shown

$$P_n = \frac{(F_n)^p}{\sum_{n=1}^{N} (F_n)^p} \tag{2.5}$$

The exponent p is one of the GA convergence parameters and we have chosen p in the order of 500. The selected sets are paired randomly. In the crossover stage the parameters are written in binary and the corresponding numbers from the parents crossed over at a random point along the binary. This crossover point divides the parameters into two parts and the second parts of the parameters are interchanged. The mutation randomly switches 1 to 0 and vice versa with a mutation rate of r. This has a significant influence on the performance. A rate that is too high not likely to converge and a rate that is too low will not introduce enough variation in the parameter sets and the algorithm will stagnate. These last four steps generate

another N sets of new parameters and the procedure is repeated until the criteria is reached, i.e. the root mean square deviation (RMSD), Δ_n, is below a certain value or a maximimum number of iterations has been reached.

The GA convergence parameters, N and r, were tested to find the optimal values for an efficient minimisation. We found that a rate of $r = 1\%$ and $N = 16$ sets was optimal for our system. The initial guesses for ϵ_{ij} and σ_{ij} were chosen randomly but within the range of physically realistic values. If the parameters are treated fully independently in the fitting procedure, the algorithm could converge to a set of parameters where $\sigma_{\mathrm{H_w}j} > \sigma_{\mathrm{O_w}j}$ i.e. the 'size' of the water hydrogen is larger than the water oxygen, which is physically unrealistic. To address this issue, we added a constraint to keep the values of σ_{ij} for the hydrogen atoms smaller than those for the oxygen atoms.

2.3 Results and discussion

The DFT energy landscape for the water–ZnO system was created by placing water molecules on the ZnO surface in 198 different configurations, which differ in position and orientation with respect to the surface. This ensures that the adsorption energy landscape of the water–ZnO surface interaction is well sampled. In this section we will discuss the importance the choice of the sample that is used in the fitting procedure. Furthermore we address the question of the non-uniqueness of the resulting parameters and compare the result to the performance of a standard force field, namely the OPLS force field.[36]

The choice of the sample is an important factor in the fitting procedure. One would assume that the full set of the 198 data points should be used to fit the classical potentials. While this might lead to an improved set of classical force field parameters it is potentially computationally costly, so it is interesting to see if it is possible to reproduce the full DFT data set using only a subset of all the structures. A subset of 100 configurations has been chosen, which is representative of the full energy range of the whole set of 198 configurations. In Fig. 2.5 the fitted and predicted energies obtained by the resulting force field of the GA fitting procedure are shown. It can be clearly seen, that the qualitative agreement between the DFT data and the GA force field is excellent. Quantitatively, the fit (taking into account the fitted and predicted energies) gives an overall RMSD of 3.21 kJ/mol, which is within the error of the DFT calculations. The corresponding force field parameters are reported in Tab. 2.2. In addition, a fit using the full data set of 198 conformations was performed and the

RMSD is 3.37 kJ/mol, which is similar to the result of the 100 structure subset. This leads to the conclusion that a fit with 100 configurations is sufficient to reproduce the full set of energies.

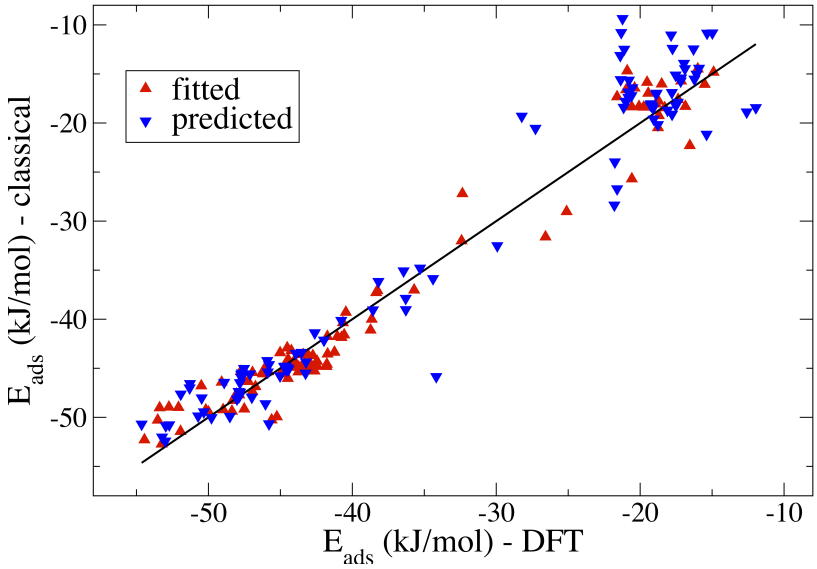

Figure 2.5: Comparison of the DFT results for the adsorption energies with the ones from classical simulations. The black line is the perfect match, where the classical adsorption energies are in full agreement with the DFT results. The red up-triangles represent the results obtained with the GA fitting method (100 different low and high energy conformations). The blue down-triangles are the predicted adsorption energies for the remaining 98 configurations, obtained with the fitted classical force field.

We compared the GA adsorption energies with the adsorption energies one would get from a classical simulation with a standard OPLS force field[36]. We took the Lennard Jones parameters for the Zn, O and H atoms of the surface, the SPC water parameters and used the geometric combination rule to obtain the pairwise interaction potentials i.e. $\sigma_{ij} = \sqrt{\sigma_i \sigma_j}$ and $\epsilon_{ij} = \sqrt{\epsilon_i \epsilon_j}$. The partial charges for the surface are, as previously mentioned, obtained from the DFT calculations. In the SPC water model the LJ parameters of the H_w atoms are zero. Therefore, the LJ part of the force field is described by only four parameters, namely $\sigma_{O_wO_s} = 0.3143$ nm, $\epsilon_{O_wO_s} = 0.6801$ kJ/mol, $\sigma_{O_wZn_s} = 0.2486$ nm and $\epsilon_{O_wZn_s} = 0.7975$ kJ/mol. In comparison to the GA fit the OPLS force field performs worse with an RMSD of 7.49 kJ/mol. Nevertheless, it seems that the OPLS force field is not completely wrong. This is mainly due to the strong electrostatic contribution. If one considers only the electrostatic interaction, the RMSD is 6.10 kJ/mol. The predicted energies from the electrostatics, OPLS and GA force field are shown in Fig. 2.6 . The Coulombic interaction alone is already a good estimate for the adsorption energies.

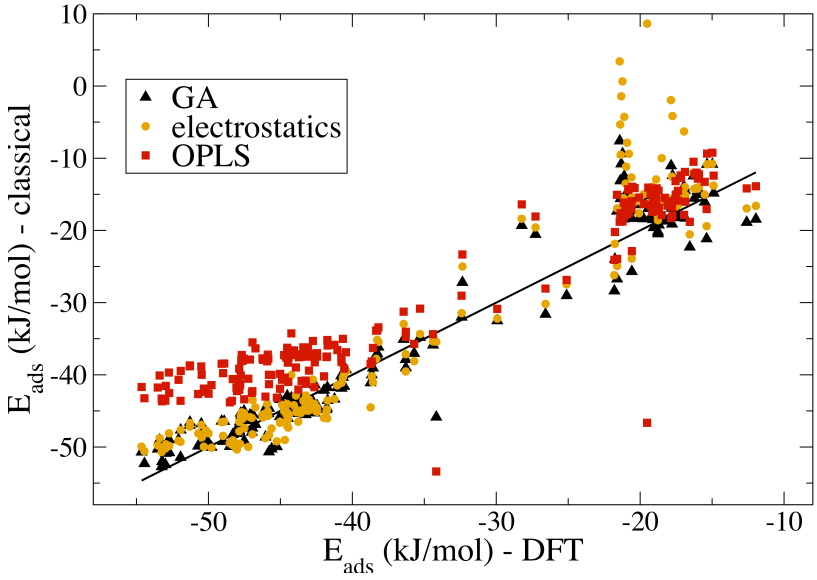

Figure 2.6: Comparison of the DFT adsorption energies (black line) for the 198 configurations with the results from the GA fitting method (black triangles) and the OPLS force field (orange circles). Further we showed the contribution of the electrostatic interaction (red squares) for the different configurations.

By modifying the LJ parameters for the surface potentials, one can further improve the force field so that the GA converges to a lower RMSD than the pure electrostatic contribution. This improvement can be also qualitatively seen in Fig. 2.6. On the contrary, the LJ parameters of the OPLS force field deteriorate the overall results and systematically predict too high energies for the deep minima of the potential energy surface.

Generally, the genetic algorithm converges to a non-unique set of parameters, but the results are comparable. To get a better idea of the spread of the parameters, we run 50 independent GA fits using the same configurations. The average value and standard deviation of each of parameters σ_{ij} and ϵ_{ij} are reported in Tab. 2.2. For each pair interaction the spread of ϵ_{ij} is larger than that of σ_{ij}. We have calculated the energies for the 198 structures using a force field with the average parameters and the RMSD is 5.01 kJ/mol. Taking the average parameters, therefore, does not lead to any improvement in the RMSD.

We have investigated the importance of choosing a data set that is representative with respect to the to the adsorption energy landscape. In the case of liquid water in contact with a solid this means that not only the deep but also the shallow minima of the potential energy surface must be sampled. To study the dependence of the choice of the parameter set thoroughly, we compare two more data subsets. The first subset

	$\sigma_{ij} * 10^{-1}$ (nm)						$\epsilon_{ij} * 10^{-1}$ (kJ/mol)					
	O_wO_s	H_wO_s	O_wH_s	H_wH_s	O_wZn_s	H_wZn_s	O_wO_s	H_wO_s	O_wH_s	H_wH_s	O_wZn_s	H_wZn_s
lowest RMSD	2.410	2.215	1.982	1.767	2.698	2.536	8.893	5.516	8.495	9.249	8.339	3.129
average	2.567	1.251	2.060	1.402	2.290	1.237	6.814	4.777	5.770	7.082	6.449	5.178
stand. deviation	0.537	0.735	0.224	0.702	0.752	0.926	3.109	2.763	3.291	3.118	3.216	2.456

Table 2.2: 50 GA fits using the subset of 100 low and high energy structures. In the first row the parameters corresponding to the lowest RMSD of the fitted set (2.264 kJ/mol) are reported. In the second row the average parameters over all 50 different GA fits are shown and in the third row the standard deviation is reported.

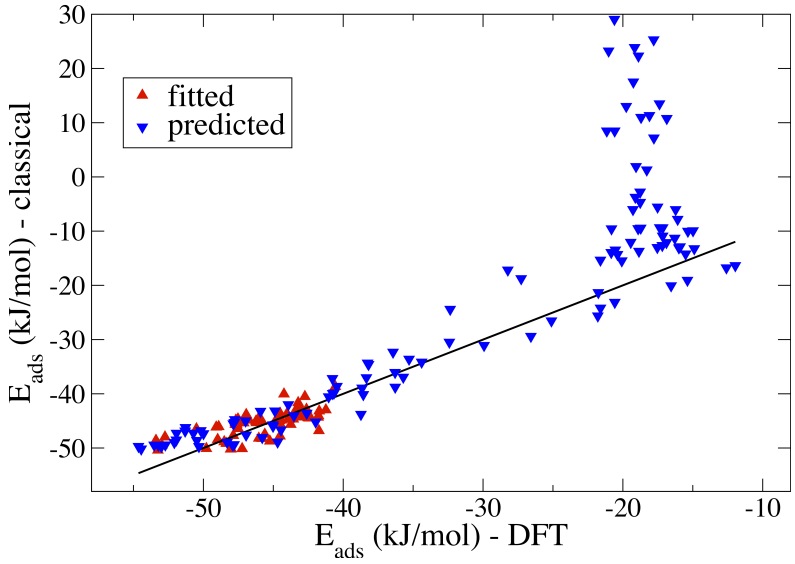

Figure 2.7: Comparison of the DFT results for the adsorption energies with the ones from classical simulations. The black line is the perfect match, where the classical adsorption energies are in full agreement with the DFT results. The red up-triangles represent the results obtained with the GA fitting method (70 different low energy configurations). The blue down-triangles are the predicted adsorption energies for the remaining 128, mostly high energy configurations, obtained with the fitted classical force field. 15 data points, for which the energy is higher than 30 kJ/mol, are not shown.

contains mostly low energy structures (70 different configurations) and the second contains mostly high energy structures (70 different configurations). In Fig. 2.7 the result of the fit using the subset of lower-energy structures are shown. One can clearly see, that the fitted energies are in good agreement with the DFT energies.

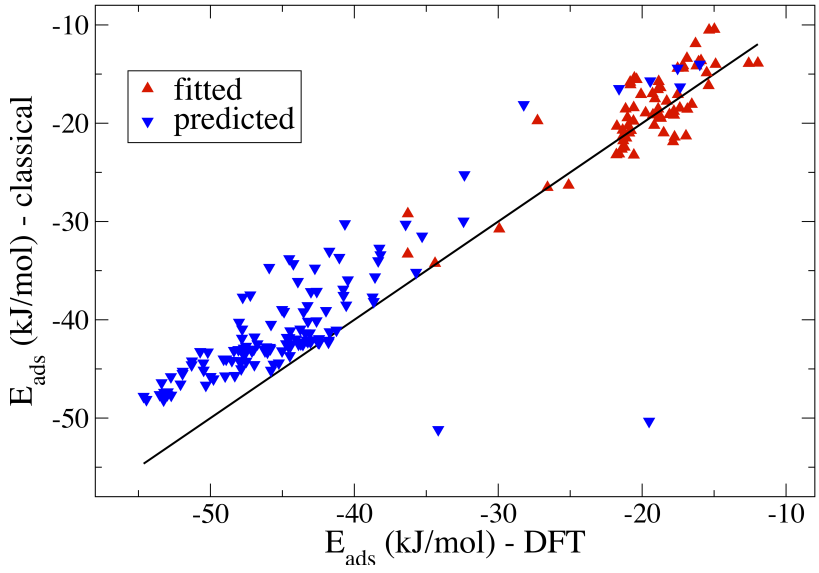

Figure 2.8: Comparison of the DFT results for the adsorption energies with the ones from classical simulations. The black line is the perfect match, where the classical adsorption energies are in full agreement with the DFT results. The red up-triangles represent the results obtained with the GA fitting method (70 different high energy configurations). The blue down-triangles are the predicted adsorption energies for the remaining 128, mostly low energy configurations, obtained with the fitted classical force field.

The resulting RMSD deviation for the 70 fitted structures is 2.11 kJ/mol. Also shown are the predicted energies, which deviate significantly from the DFT energies. The total RMSD with respect to all 198 configurations is 39.14 kJ/mol. Fig. 2.8 shows the fitted and predicted energies for the second subset. The RMSD for the fitted points is 2.63 kJ/mol and the RMSD for the full data set is 5.31 kJ/mol. The quantitative agreement with the DFT energies is reasonably good, although especially in the very low energy cases one can see a clear deviation from the DFT results. However, this good result is by chance and by performing 15 GA fits, using the same subset of structures, we get very different results. In each case the GA converged to approximately the same RMSD for the fitted subset, however, the RMSD of the entire set of 198 DFT energy points varies widely. For example, in one fit to the subset 70 low energy points, the RMSD of the fitted set is 2.33 kJ/mol, but the fit to the the full set of 198 configurations results in an RMSD of 2171.40 kJ/mol. This clearly demonstrates the importance of choosing a sample that is representative of a wide range of structures and energies. Therefore the quality of the resulting parameter sets must be rechecked after the fitting procedure, especially when the fit is performed on a

subset of energies, but by using the GA fitting method this can be done in a fast and efficient way.

2.4 Summary and outlook

A genetic algorithm was used to optimise classical force field parameters to model molecule–solid interfaces. We took a water-ZnO(0001) system as a benchmark system to test the performance of the method. The adsorption energies from the classical force field were matched to the DFT calculations for various conformations of the water molecule on the surface. In order to describe the fluid–solid interface realistically, the force field must be capable of reproducing a wide range of structures and energies and we have shown that the GA method can efficiently handle a large data set. A subset of 100 low and high energy configurations of water molecules on the ZnO(0001) surface resulted in a classical force field that reproduced well the DFT potential energy landscape of the water/ZnO interfacial interactions and predicted good adsorption energies for a further 98 conformations that were not used in the fit. We also demonstrate the importance of the right choice for the fitted data sample. If the subset contains mostly low energy configurations the fitting procedure does not necessarily lead to good results for the high energy configurations and vice versa. This means that fitting to a non-representative sample of the adsorption energy landscape could lead to wrong predictions of physical properties in a molecular dynamics study.

Although this work has been applied to the specific system of water on a ZnO surface, the method can be used to model any system. It is especially suitable for more complicated systems where there are a large number of interaction parameters, such as the adsorption of complex molecules on surfaces with a variety of adsorption sites. Although large systems are beyond the reach of density functional calculations the algorithm can be used in combination with the 'building block approach'[4,9,13], where the macromolecules are broken down into smaller chemical subunits. The GA fitting procedure can be applied to these smaller sub-molecules and, assuming transferability of the parameters, the classical force field of the whole macromolecule can be developed.

We presented a method that generates surface potentials for interfacial systems in a very fast and efficient way. A standard LJ and Coulombic potential is able to capture the complexity of the interfacial interaction over a broad energy distribution. However, the method is implemented in a flexible way so that other potential forms could

be used. Additionally, the GA is in principle capable of fitting the partial charges, assuming neutral conditions at the surface, without having any pre-information from DFT calculations. In this work the fit is based on energy differences for a variety of conformations, however, other data, such as structural information, could be used by modifying the information that enters the fitness function.

3 Development of classical molecule–surface interaction potentials based on density functional theory calculations: investigation of force field representability.

A simple classical force field, based only on Coulomb and Lennard-Jones potentials, is developed to describe the interaction of an ethanol molecule physisorbed on the α-alumina (0001) surface. A range of adsorption structures are calculated using density functional theory (DFT) and these results were used for the force field parameterisation. This system has a very inhomogeneous adsorption energy landscape and the importance of the choice of data set used for fitting the force field is investigated. It was found that a Lennard-Jones and Coulombic potential can describe the ethanol-alumina interaction in reasonable qualitative agreement with the DFT reference provided that the data set is representative of both short and long range interactions and high and low energy configurations. Using a few distance-dependent adsorption energy curves at different surface sites gives the best compromise between computing time and accuracy of the force field. This approach demonstrates a systematic way to test the quality of a force field and provides insight into how to improve upon the representability of the force field for a complex adsorption energy landscape.

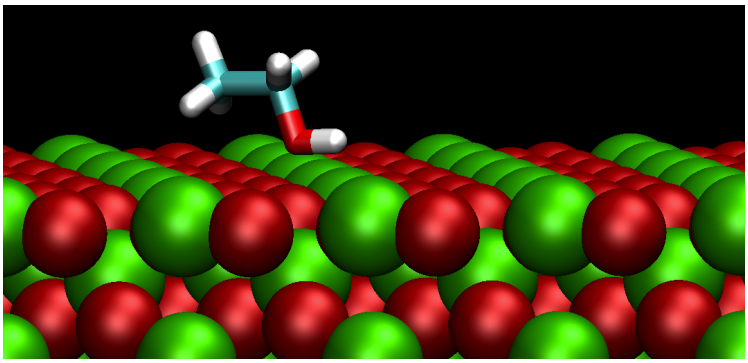

Figure 3.1: An ethanol molecule adsorbed on α-alumina.

3.1 Introduction

The interaction of soft matter with inorganic surfaces is of importance in many applications such as biomineralisation, composite materials and self-assembled monolayers. For protective polymeric coatings strong adhesion between soft matter and inorganic surfaces is essential. As a specific example polyurethane coatings are often applied to a surface as a mixture of dialcohols, trialcohols and dicyanates, which polymerise in situ. The interaction of the individual components with the surface will determine whether the mixture becomes segregated, which will affect the quality of the polymer, and how the final polymer bonds to the surface.

To understand the behaviour of such a system it is necessary to consider both the detailed chemical interaction at the surface, as well as the properties of the polymer or mixture. Classical molecular dynamics simulations can be used to understand the structure and dynamics of liquids on surfaces. However, the results of such simulations depend on the classical force field used to describe the adsorbate–surface interaction. Often, the interaction between the liquid and the surface is modelled using standard force fields, such as OPLS, GROMOS or AMBER with combination rules. However, these force fields were developed to describe bulk properties of liquids or solutions and it is unlikely that this approach would provide a qualitatively correct physical picture of the interface.

A better approach for developing a classical force field is to fit the parameters such that the results from the force field agree with the results of quantum chemistry or density functional theory (DFT) calculations.[1–3,5,8,12–17] Often, the interaction energy as a function of distance from the surface to the molecule at only a single or a few surface sites is considered. For relatively homogeneous surfaces, such as metallic surfaces, this might be a reasonable approximation. However, in the case of oxide surfaces, where the surface is very inhomogeneous, this inhomogeneity could strongly affect properties such as diffusion along the surface, local structure or adhesion strength. Thus, it is not a priori clear if force fields that are fitted to only a few adsorption states represent different adsorption states correctly. In this work, we study the representability of force fields that are fitted to a subset of the adsorption energy landscape and investigate the optimal set of DFT data needed to obtain a representative force field. This work thematically follows a previous study of a water molecule on ZnO(0001), which investigated the effect of fitting the force field parameters to a horizontal scan of the surface at constant height (xy-scan)[17] and it was

found that fitting to only a few adsorption configurations can bias the resulting force field and is, therefore, not representative of the full adsorption energy landscape. Here, we go a step further and compare the pros and cons of fitting to horizontal surface scans versus fitting to z-dependent adsorption curves, which are often used in the literature to obtain classical force fields.[1,3,5,8,15,16] As a model system we take ethanol on the well-studied Al-terminated α-Al_2O_3(0001) surface, shown in Fig. 3.2. The –OH group of the ethanol interacts via electrostatic interactions with the surface Al and O atoms and therefore the energy will vary considerably as the molecule moves across the solid surface. In total, we fit to 10 pair potentials (20 force field parameters) and the representative sample of adsorption energy landscape, which includes 174 adsorption configurations (containing z-dependent and horizontal xy surface scans). The many adjustable parameters and the amount of DFT data makes a manual fit unfeasible and, therefore, we apply a genetic algorithm to optimise and automate the procedure, which has proven to be a useful tool in our previous work.[17]

This paper is organised as follows. First, in section 3.2, we outline the technical details of the DFT calculations and the classical force field. Next, we present DFT results for the interaction of the ethanol molecule with the surface (section 3.3.1), which is followed by a discussion of the fitting procedure and an evaluation of representability of the force fields (section 3.3.2). The summary is presented in section 3.4.

3.2 Method

The density functional theory calculations were performed using the VASP code[90,101], with a self-consistent van der Waals implementation[102,103] and PBE exchange.[61–63] The core electrons were described using projector augmented waves (PAW).[88,89] A planewave energy cutoff of 500 eV was used and all calculations used a Brillouin zone mesh equivalent to $4 \times 4 \times 1$ for the surface unit cell. Bulk alumina is hexagonal with an equilibrium lattice constant of a_0 =4.82 Å and $c/a = 2.73$. For the adsorption calculations we used a AlO_3Al-R slab, 18 atomic layers deep and 2×2 surface unit cells wide, which has lateral dimensions of $a = b = 9.64$ Å. Relaxation of the isolated molecule and surface was stopped when the maximum force on any atom was less than 10 meV/Å. For all adsorption configurations the surface and molecule atoms were fixed. Partial charges were calculated using the Bader analysis method.[104–106]

The classical calculations were performed using GROMACS 4.[98] The cutoff for the short range potentials was 13 Å and the electrostatics are calculated using the Ewald method with a force and potential correction to avoid interactions between slab images in the z direction. The alumina surface was described by placing Al and O atoms in the relaxed positions of the isolated surface that were found from the DFT calculations. The classical simulations require a cell larger than the cutoff distance so the surface was multiplied by 3×3 along the a and b axis. The resulting simulation box is hexagonal with $a = b = 28.92$ Å and c =39.48 Å. Otherwise the molecule and surface atom positions are identical to those used in the DFT calculations.

For the classical force field we represent the interaction between the molecule and the surface using electrostatic interactions and the well-known Lennard-Jones 12–6 potential

$$V_{ij}^{\mathrm{LJ}} = 4\epsilon_{ij}\left\{\left(\frac{\sigma_{ij}}{r_{ij}}\right)^{12} - \left(\frac{\sigma_{ij}}{r_{ij}}\right)^{6}\right\} \tag{3.1}$$

with two parameters, σ_{ij} and ϵ_{ij}, per atom pair ij. The system has 7 atom types and 10 atom pairs, which results in the 20 different force field parameters listed in Tab. 3.4. Many force fields use the ionic formal charges, which are much higher than the actual charges present in the system. For the alumina surface, the currently developed force fields use the DFT Bader partial charges, presented in Tab. 3.1, which correspond to the charge contained between the charge density minima contours around the atoms. Each layer in the surface contains a formula unit of alumina containing the atomic layers [$\mathrm{Al_{upper}}$–3O–$\mathrm{Al_{lower}}$], as shown in Fig. 3.2(a). The data in Tab. 3.1 gives the average value of the three coplanar oxygen atoms. For the partial charges of the molecule the OPLS parameters were used, which are given in Tab. 3.2. This ensures that we do not alter the properties of liquid ethanol as predicted by the OPLS force field.[36]

The genetic algorithm used here has been described in detail in Ref. [17]. The difference between the classical and the DFT energy landscape is $\delta E_j = E_{\mathrm{DFT}} - E_{\mathrm{class}}$ for a particular adsorption configuration j. The root mean square deviation (rms) of the energy difference for the ith parameter set is

$$\Delta_i = \sqrt{\frac{1}{M}\sum_{j=1}^{M}\delta E_j^2}, \tag{3.2}$$

	Atom		
Layer	Al_{upper}	O	Al_{lower}
1	+2.42	−1.63	+2.49
2	+2.50	−1.66	+2.49
3	+2.49	−1.66	+2.49
4	+2.49	−1.66	+2.49
5	+2.49	−1.65	+2.49
6	+2.48	−1.57	+2.17

Table 3.1: Partial charges of isolated surface calculated using density functional theory. Al_{upper} (Al_{lower}) refers to the Al atom just above(below) the O atomic layer.

Atom	Partial charge
C_{OH}	+0.145
C_{H_3}	−0.180
H_C	+0.060
O_H	−0.683
H_O	+0.418

Table 3.2: Partial charges of ethanol used in the OPLS force field.

where M is the number of DFT data points used in the fitting procedure. The rms value is used to assess the accuracy of the force field.

3.3 Results and Discussion

3.3.1 Density functional theory

In a simulation of liquids on surfaces it may be necessary to use a classical potential that describes the vibrational and dynamical properties of the solid substrate. However, this work addresses only the interaction between the surface and the molecule. Furthermore, we we restrict the configurations to non-dissociative adsorption structures of ethanol on alumina. In order to exclude any strain energy for surface relaxations, a series of unrelaxed configurations is used for the surface–molecule interaction. The surface atoms are fixed in the positions corresponding to that of the isolated surface. For the isolated surface the top Al_{upper} atom sinks into the O layer to minimise the surface dipole, which can be seen in Fig. 3.2. The

molecule is translated rigidly in the x, y and z directions and both horizontal and vertical orientations are considered. This includes five different surface scans in the xy-plane with different heights from the surface and different molecular orientations and seven scans along the z direction at different surface sites. The various configurations are summarised in Tab. 3.3. For convenience x, y and z are given in fractional coordinates, which are in units of the simulation cell along the a, b and c axes.

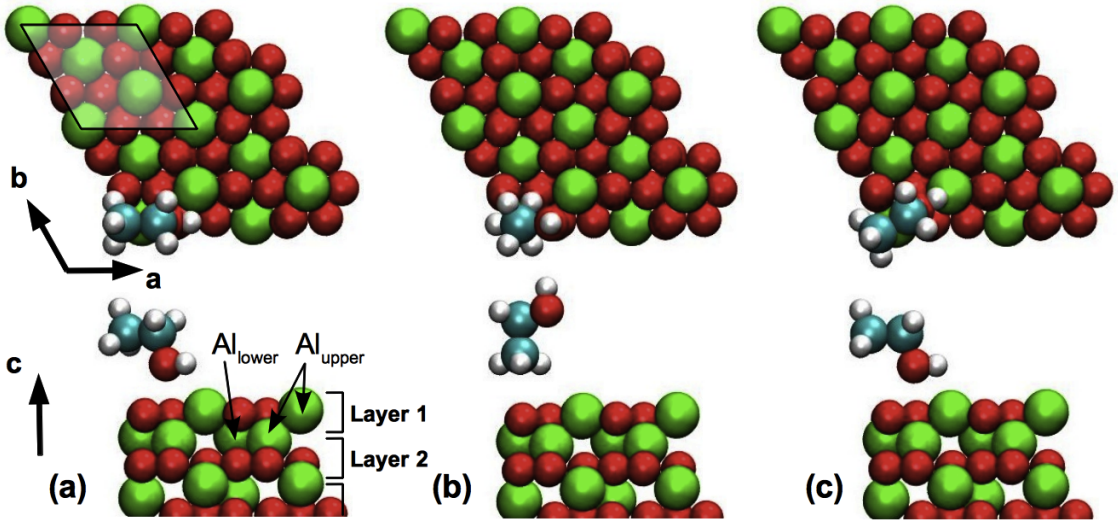

Figure 3.2: Three different orientations of ethanol on the alumina surface (a) $\theta = 0^o$, $\phi = 0^o$, corresponding to configurations xy-a, xy-b and xy-c (b) $\theta = 90^o$, corresponding to xy-d and (c) $\theta = 0^o$, $\phi = 30^o$, corresponding to xy-e. The rhombus in (a) shows the surface unit cell of alumina.

First we consider the xy-scans. In Fig. 3.2(a) the molecule has the C–C bond parallel to the surface plane ($\theta = 0$) and the a direction ($\phi = 0$) and the –OH group points towards the surface. Three different z values for this configuration were used, namely, $z = 0.375$, $z = 0.380$ and $z = 0.390$, corresponding to the carbon atoms being a distance of 2.84 Å, 3.03 Å and $z = 3.43$ Å from the surface. In Fig. 3.2(c) the orientation is similar except that the C–C bond makes an angle of $\phi = 30$ with the a-axis and in this case $z = 0.390$. In Fig. 3.2(b) the molecule is in a vertical orientation with the C–C bond perpendicular to the surface plane $\theta = 0$, the –OH group pointing away from the surface and $z = 0.390$.

Three of these scans are shown in Fig. 3.3. Although the surface unit cell is hexagonal the scans are shown using orthogonal axis, where the x and y coordinates are the fractional coordinates of the unit cell along the a and b directions. Fig. 3.3(a) is at $z = 0.380$ with molecular orientation $\theta = 0$ and $\phi = 0$, and is mainly repul-

	x	y	z	θ	ϕ
xy-a	–	–	0.375	0	0
xy-b	–	–	0.380	0	0
xy-c	–	–	0.390	0	0
xy-d	–	–	0.390	90	–
xy-e	–	–	0.390	0	30
z-a	0.00	0.00	–	0	0
z-b	0.20	0.10	–	0	0
z-c	0.20	0.30	–	0	0
z-d	0.25	0.25	–	0	0
z-e	0.20	0.00	–	0	0
z-f	0.00	0.00	–	90	–
z-g	0.00	0.00	–	0	30

Table 3.3: Summary of the various scans used for the adsorption energy landscape. x, y and z are in fractional coordinates and angles are in degrees.

sive except at (0.2,0.1), which corresponds to the ethanol oxygen being close to the surface aluminium atom. Fig. 3.3(b) is slightly further from the surface at z=0.390 and shows a mixture of attractive and repulsive sites. The shape of the landscape is similar to Fig. 3.3(a) but shifted to lower energies. Fig. 3.3(c) is at the same height as Fig. 3.3(b) but with the molecule rotated by $\phi = 30^{o}$ in the xy-plane, as shown in Fig. 3.2(c). In summary, the attractive regions correspond to configurations where the O_C is close to an Al atom and far from the O_s atoms. The xy-scans that are not

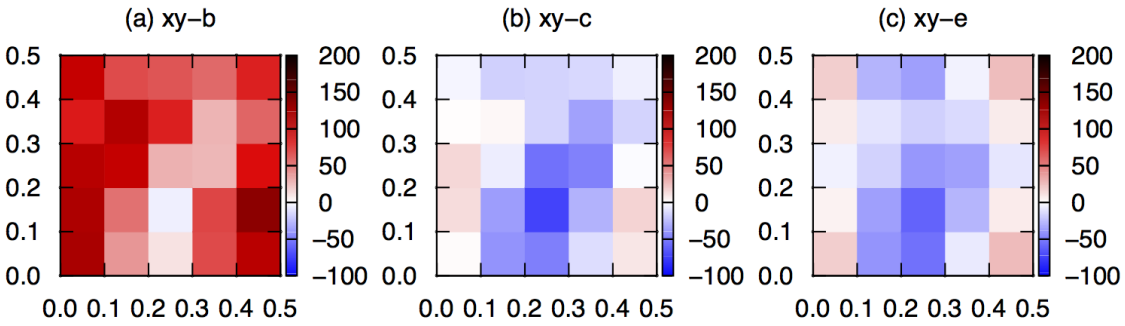

Figure 3.3: Horizontal scans of the interaction energy of ethanol on the alumina surface corresponding to (a) xy-b, (b) xy-c and (c) xy-e. Red corresponds to a repulsive interaction and blue is an attractive interaction. The x and y axes represent fractional coordinates along the a and b axes, respectively and the color bar range is in kJ/mol.

shown are xy-a, which is entirely repulsive, and xy-d (shown in Fig. 3.2(b)), whose

adsorption energy only varies between −20.94 and −29.52 kJ/mol and is nearly featureless.

Next, we consider the seven different z-curves, which are shown in Fig. 3.4. The most attractive site is at (0.20,0.10), as seen before in Fig. 3.3, with a configuration of $\theta = 0^o$, $\phi = 0^o$ and with a minimum adsorption energy of around -90 kJ/mol at $z = 0.390$ (2.84 Å from the surface). The configuration with a vertical orientation of the molecule has the –OH group oriented away from the surface and the curve is weaker and broader. The most weakly attractive site is at (0.0,0.0) with $\theta = 0^o$ and $\phi = 30^o$.

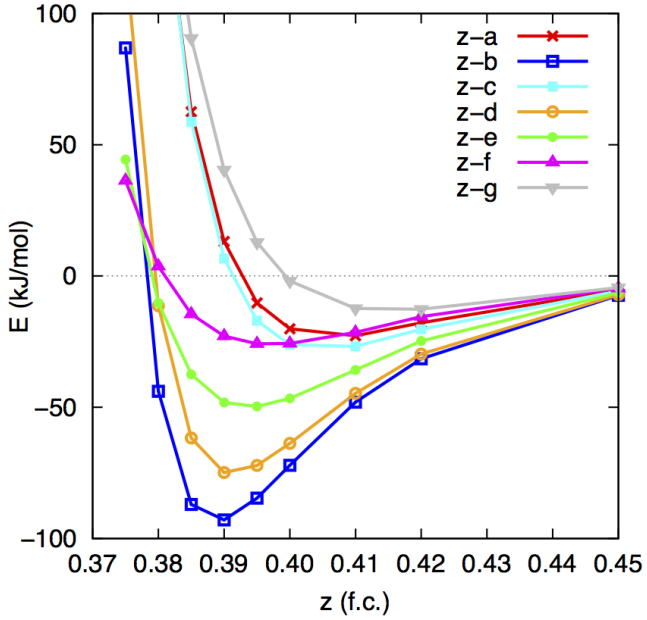

Figure 3.4: Vertical scan of the interaction energy of ethanol at different points on the alumina surface.

3.3.2 Force field optimisation

The density functional calculations in the previous subsection provide a good representation of the adsorption energy landscape. In this section we investigate whether the simple Lennand-Jones and Coulomb force field can represent the DFT data and the importance of the size and choice of the data set used for optimisation. Additionally, we compare the performance of our present force fields with the results using a parameter set that was proposed by Youngs et al. in a previous study of isopropanol on γ-alumina.[14]

For the genetic algorithm we used 64 parameter sets and a mutation rate of 3%. Sets 1 and 2 were run for 900 iterations and set 3 for 236 iterations. The reduced number of iterations for set 3 is because the large number of configurations is more computationally demanding than the other sets. The lowest rms values were reached after 137, 93 and 117 iterations for sets 1, 2 and 3, respectively.

Since the electrostatics is a significant part of the interaction, we start by looking at the rms values obtained from the electrostatic interaction only. This gives rms values of 95 kJ/mol and 91 kJ/mol for the formal charges and DFT partial charges, respectively. By looking at the z-scans in Fig. 3.5 it is clear that in some cases the electrostatics predict an unrealistic attractive interaction at short range, most notably in Fig. 3.5(a). It is this short-range attraction that the repulsive part of the Lennard-Jones pair potential must balance. The force field by Youngs et al. reproduces the Al-O distance and interaction energy for one configuration of a water molecule adsorbed on α-alumina.[14] These parameters are listed in Tab. 3.4. Using these parameters with the formal charges results in an rms of 290 kJ/mol and with partial charges the rms is 295 kJ/mol, which are both worse than using only electrostatics. The reason for this high rms is due to inaccuracy of the close-range repulsion, which in Fig. 3.5(b) swamps the attraction completely and in Fig. 3.5(c) overestimates the adsorption energy.

To develop an accurate force field it is necessary to optimise the Lennard-Jones pair potential parameters. In our previous paper for water on ZnO[17], we optimised the parameters so that the force field reproduced DFT results for an energy landscape in an xy-plane. The importance of fitting a wide range of adsorption configurations was highlighted. Here we take the work a step further by using a DFT data sets in xy and z and with with various configurations. The results obtained using the entire set and two subsets are compared. In total there are five scans of the adsorption energy in the xy-plane and z-scans for seven different configurations, which altogether gives 174 distinct data points. We have used the following three data sets for fitting (see Tab. 3.3):

- Set 1: One xy-scan: xy-c (25 points).
- Set 2: Three z-scans: z-b, z-c, z-f (27 points).
- Set 3: Full data set (174 independent points).

The xy-scan in set 1, shown in Fig. 3.3(b), was chosen because it has both repulsive and attractive sites and contains the most strongly attractive site. The three

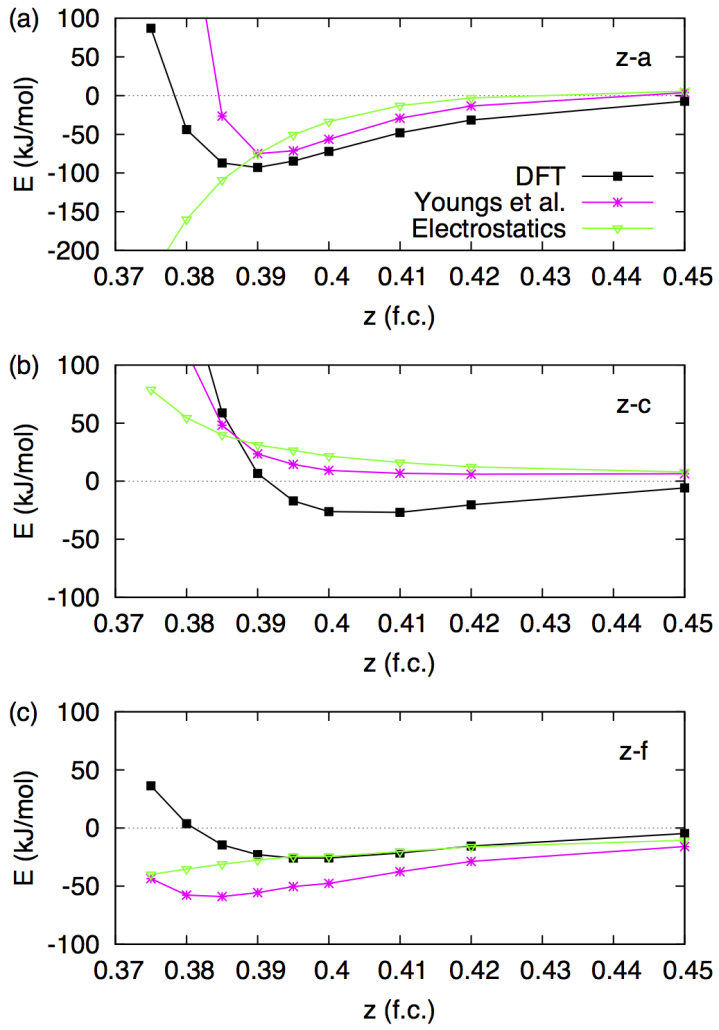

Figure 3.5: Comparison of DFT, electrostatics and classical energies using the parameter set from Youngs et al.[14] The three panels correspond to the three different configurations labelled in the graphs, corresponding to (a) z-b (b) z-c and (c) z-f.

z-scans of set 2 were chosen to represent both strongly and weakly attractive sites, as seen in Fig. 3.4. The number of points in both of these sets is similar, which makes the comparison between these two optimised force fields fair.

All configurations with energies over 100 kJ/mol were weighted in the fitting procedure by 0.1 to account for the fact that the short-range behaviour of the Lennard-Jones potential is generally too repulsive. These very high energy configurations (in the order of tens of kT) are not likely to be accessed in molecular dynamics simulations and therefore the accuracy of these energies is less important. Nevertheless, the resulting force field should predict these configurations to be repulsive in order to avoid sampling unrealistic configurations. To compare the quality of the three

		Ref. [14]		Set 1		Set 2		Set 3	
Mol	Surf	σ	ϵ	σ	ϵ	σ	ϵ	σ	ϵ
C_{OH}	Al	0.30650	0.65	0.1148	0.8593	0.6245	0.0006	0.3375	1.0490
C_{H_3}	Al	0.30000	0.65	0.3837	1.0060	0.1304	0.3597	0.5079	0.0087
H_C	Al	0.30000	0.65	0.0187	0.5574	0.3117	0.6052	0.0239	0.1899
O_C	Al	0.26778	0.65	0.1251	0.1812	0.2684	0.0751	0.0130	0.5910
H_O	Al	–	–	0.2387	0.3063	0.2126	0.1280	0.3095	0.0409
C_{OH}	O_s	0.30000	0.65	0.3952	0.7475	0.3353	0.6278	0.1556	0.0088
C_{H_3}	O_s	0.30000	0.65	0.3670	0.8590	0.4448	0.2117	0.2019	0.3254
H_C	O_s	–	–	0.3393	0.4304	0.1244	0.1974	0.2120	0.5181
O_H	O_s	–	–	0.1026	0.2138	0.0114	0.6335	0.2295	0.6658
H_O	O_s	0.28000	0.65	0.0071	0.9407	0.2632	0.7019	0.2492	0.4860

Table 3.4: Force field parameters for molecule–surface interaction. Units of σ and ϵ are nm and kJ/mol, respectively.

parameter sets we use the unweighted rms value for the entire set. Tab. 3.5 shows the rms value for the weighted, fitted set (rms-fit), the total, unweighted rms value (rms-full), the rms values for short- and long-range and higher and lower energy configurations. Note that in set 1, all values are below 100 kJ/mol and, therefore, no weighting was required.

The resulting parameters are not "physical" in the sense that the σ values are not proportional to the ionic radii. However, in the context of fitting simple pair potentials to describe electronic structure data there is no reason to believe that the interactions should be simply represented by ions of a particular size. These potentials encompass a range of multibody interactions and therefore the parameters should be allowed to vary freely so that they give the best fit to the available data. We also note that many different parameter sets can give similar rms values and there is no unique solution.

The rms values for the three fitted sets are shown in Tab. 3.5. For set 1, which is the fit to the adsorption energy landscape xy-c, we obtained an rms value for the fitted set of 21 kJ/mol and an rms value of 108 kJ/mol for the full set. This is an improvement over the parameter set used in Ref. [14] but is worse than the rms value obtained by using only the electrostatics without the pair potential. The reason for this is that the electrostatics appear to describe well the long range energies but not the short range energies, as discussed previously. Sets 2 and 3 give an improved fitting, resulting in rms values for the full data set of 88 and 77 kJ/mol, respectively. Nevertheless, the rms difference between the DFT and classical energies is still quite large and the source of this inaccuracy will be analysed in more detail in the following text.

LJ	Charges	rms-fit	rms-full	$z \leq 0.390$	$z > 0.390$	$E_{\mathrm{DFT}} < 100$	$E_{\mathrm{DFT}} > 100$
Ref. [14]	Formal	–	289.63	–	–		
None	Formal	–	95.03	–	–	–	–
None	Partial	–	90.52	99.83	33.90	57.87	165.62
Set 1	Partial	20.96	107.70	120.03	21.36	83.09	173.93
Set 2	Partial	18.67	87.85	97.59	23.39	57.94	158.23
Set 3	Partial	40.85	76.79	84.71	28.53	39.08	152.47

Table 3.5: Energies and rms differences of the classical energies vs. DFT energies for different charge and parameter sets in kJ/mol. The rms-fit is for the fitted set of data whereas rms-full is for the full dataset. The rms values are also given for the short-range ($z \leq 0.390$), long-range ($z > 0.390$), low energy (< 100 kJ/mol) and high energy > 100 kJ/mol configurations.

First, we compare the results of the three parameter sets for the z-curves, shown in Fig. 3.6. For set 1, which was fit to the xy-plane at $z = 0.390$, the energies at $z = 0.390$ are in excellent agreement with the DFT data and also agree reasonably well at longer distances. However, for short distances the curves diverge from the DFT data and can be very unphysical, as in Fig. 3.6(a). Clearly, set 1 does not reproduce the z-dependence. This is likely to be true in our previous work on water on ZnO[17] where the fit to the data in the xy-scan was good but the z-dependence was not tested. Unsurprisingly, set 2, which was fitted to these three curves, reproduces the energies rather well over the entire range, although it misses the weak attraction in Fig. 3.6(b). Set 3, which was fitted to the entire DFT data set, does not give a good fit to the z-curves and in both Figs. 3.6(a) and (c) it seriously underestimates the short range repulsion.

Next, we compare how well the three parameter sets reproduce the xy-scans at $z = 0.380$ and $z = 0.390$, both with $\theta = 0^{\mathrm{o}}$ and $\phi = 0^{\mathrm{o}}$. Set 1 was fitted to xy-c, shown in Fig. 3.7(e), and reproduces the DFT energies reasonably well (compare Figs. 3.7(e) and (f)). However, this set does not reproduce well the xy-scan at $z = 0.380$ (compare Figs. 3.7(a) and (b)), which is consistent with the results of the z-scans, where the energies at short distances are unphysical. Set 3 reproduces both energy landscapes better than set 1 (compare Figs. 3.7(a) with (d) and (e) with (h)) but underestimates the short range repulsion. Set 2 gives the best agreement with the DFT data for both xy-scans. This is surprising given that the rms value for set 3 is lower than for set 2 and to understand this we must consider the full set of data.

The full data set for all parameter sets is shown in Fig. 3.8. As mentioned before the electrostatics alone give a low rms value of 91 kJ/mol and the DFT adsorption

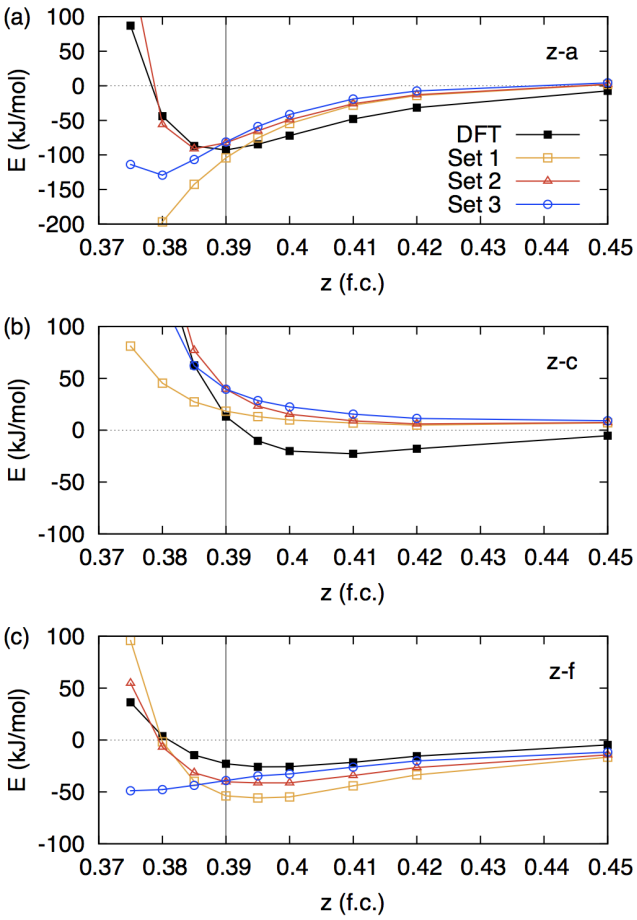

Figure 3.6: Comparison of DFT and classical energies for the z-scans (a) z-b (b) z-c and (c) z-f, using set 1 (xy-scan), set 2 (z-scan) and set 3 (full set).

energies in the range -100 to $+100$ kJ/mol are reproduced reasonably well. However, in Fig. 3.8(a) one can clearly see that the problem with the electrostatics is in the high DFT energy range, which corresponds to the repulsive regime close to the surface. In addition, there are some outlying points not shown on the graph with classical energies below -200 kJ/mol but higher DFT energies. For these higher energy configurations electrostatics alone predict much too low energies as we have already seen before in Fig. 3.5. The results from set 1 are shown in Fig. 3.8(b) and, similar to the electrostatics, it seriously underestimates the energy of many high energy structures. As mentioned previously, this would lead to incorrect sampling of high energy states and unrealistic simulations. Set 2 and set 3 have corrected this behaviour by giving a more accurate description of the repulsive configurations. Sets 1 and 2 have 5 and 3 outlying points, respectively, with very high energy classical energies that are not shown in the graphs. However, these points have DFT energies above 100 kJ/mol, except for one point in set 2 that has $E_{\mathrm{DFT}} = 78.9$ kJ/mol, and,

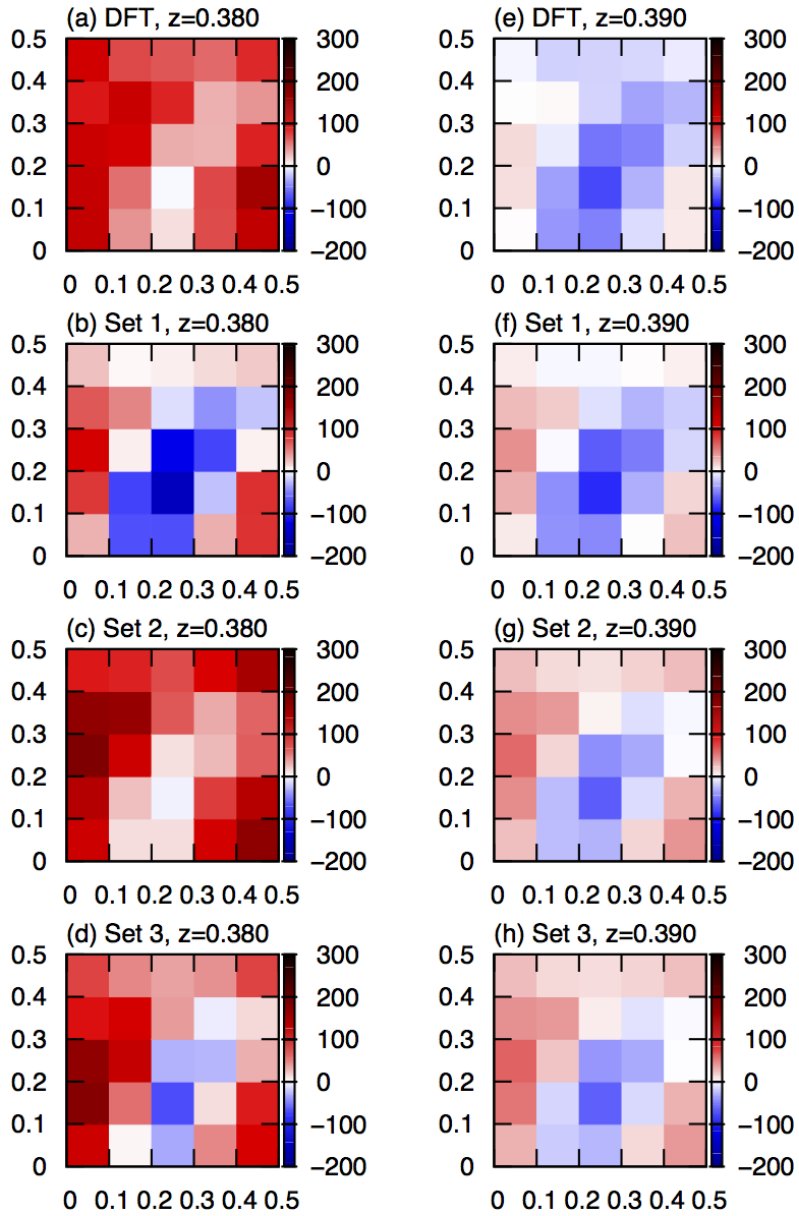

Figure 3.7: Adsorption energies for dataset xy-b using (a) DFT, (b) set 1, (c) set 2, (d) set 3 and for dataset xy-c using (e) DFT (f) set 1, (g) set 2 and (h) set 3. The x and y axes are in fractional coordinates and the color bar range is in kJ/mol.

therefore, these configurations have a low sampling probability in molecular dynamics simulations at ambient temperature. In the regime below 100 kJ/mol (to the left of the dashed line in Fig. 3.8), set 3 has a lower rms value than set 2, as seen in Tab. 3.5. It can also be seen in Fig. 3.8 that set 3 tends to underestimate the energies whereas set 2 tends to overestimate them.

For all three sets the biggest discrepancy between the classical and DFT energies originates from the regime where the molecule is in close proximity to the surface,

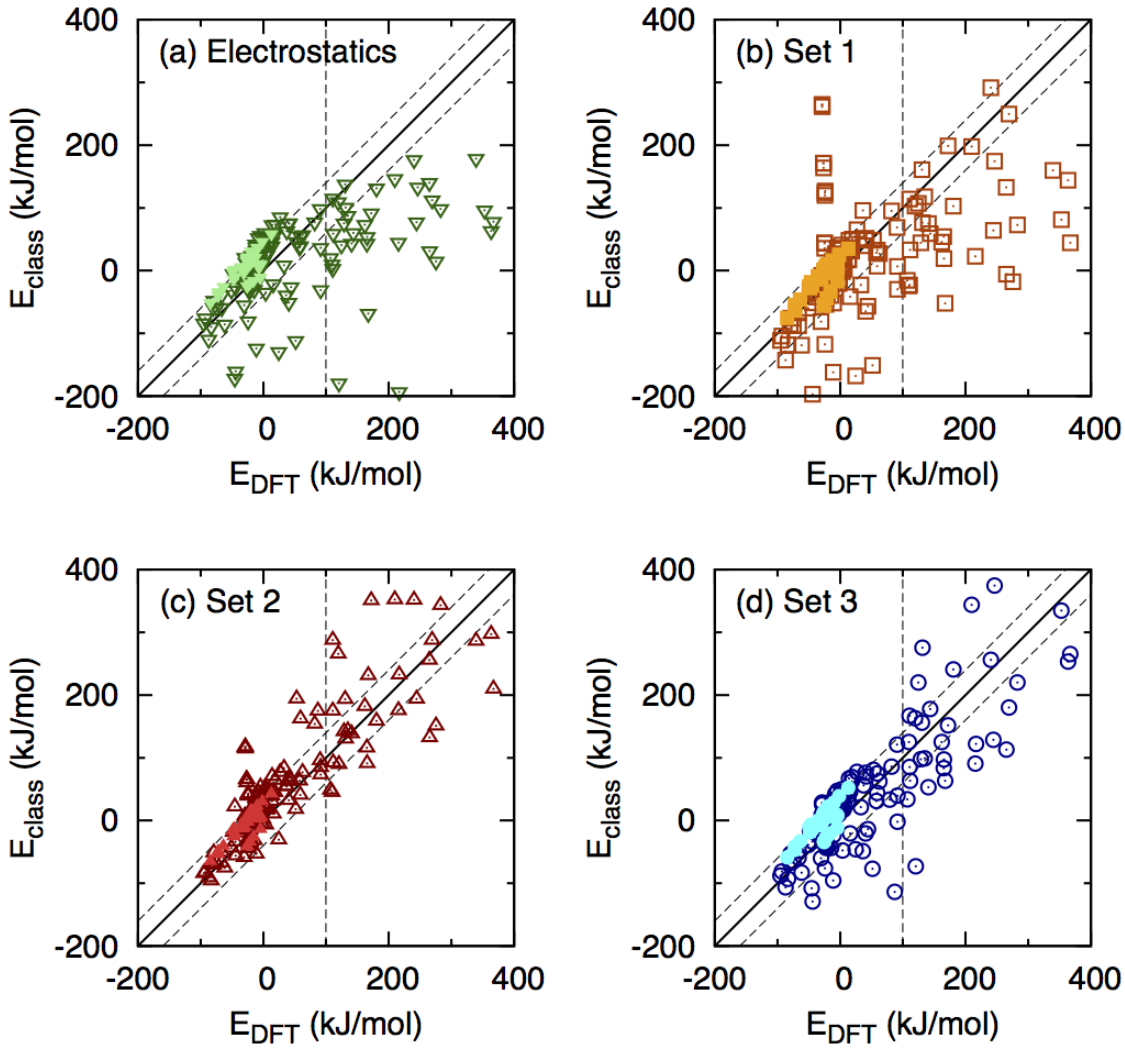

Figure 3.8: The classical energies shown against the DFT energies for all the data points using (a) electrostatics only, (b) set 1 (xy-scan), (c) set 2 (z-scans) and (d) set 3 (full set). The long range configurations are presented as filled symbols and the short range configurations as open symbols. The dashed lines are guides for the eye and correspond to an energy difference of ± 40 kJ/mol.

as seen in Fig. 3.8. In Tab. 3.5 we reported separate rms values for configurations in two different regimes. The first regime corresponds to configurations close to the surface ($z \leq 0.390$) and the second regime to configurations at distances $z > 0.390$. We have seen that sets 2 and 3 reproduce these short-range configurations better than set 1 and the electrostatics.

Although the overall rms for set 2 is slightly higher than the one for set 3, as shown in Tab. 3.5, this should not be the only criteria for judging the representability of the force field. For example, set 2 was fitted to three z-scans but also obtained xy-scans

in qualitative agreement with the DFT results, whereas set 3 was fitted to all the data but failed to qualitatively predict the xy-c, z-b and z-f data. Furthermore, the targeted optimisation of set 2 in comparison to the full set is computationally more feasible.

3.4 Summary

In this paper we have presented interface force field optimisations for ethanol on an alumina surface using a genetic algorithm. Density functional theory including van der Waals interactions was used to calculate the binding energies of a series of configurations of ethanol on alumina and the partial charges of the alumina surface. Three datasets were used for the fitting procedure: 1) an xy-landscape 2) three z-dependent scans of the adsorption energy at different surface sites and 3) a larger dataset contains five xy landscapes and seven z-dependent adsorption energy curves. The force field consists of electrostatic interactions and a nonbonded Lennard-Jones 12–6 pair potential.

An appropriate reference dataset is essential for obtaining a representative force field. A dataset only reproduces the entire adsorption energy landscape well if the dataset contains both short- and long-range and low and high energy configurations. Fitting to a single xy landscape resulted in a force field that did not reproduce the z-dependence, whereas fitting to a few z-curves on both repulsive and attractive sites gave qualitatively good agreement for the xy energy landscapes. Fitting to the entire dataset is computationally costly and did not significantly improve the fit, compared with fitting to the three z-curves.

Despite the simplicity of this force field, we have shown that by optimising the force fields parameters it is possible to obtain reasonable agreement with DFT data and, hence, to avoid sampling of unrealistic configurations in molecular dynamics simulations. Unfortunately, the validity of interface force fields in the literature has rarely been thoroughly checked. This work illustrates the difficulties involved in developing a force field that describes accurately an inhomogeneous adsorption energy landscape. Nevertheless, we have clearly demonstrated a systematic approach for checking and improving upon the representability of such a force field.

Clearly, this simple force field does have limitations, especially in the short range regime. This force field development could be improved by changing the type of pair potential used. The Lennard-Jones 12-6 potential is known to be too repulsive at short distances and the use of a different pair potential form, such as the Morse

potential[16], could give better agreement in the short-range regime. A further improvement would be to include polarisability in the force field.

4 Atomistic modelling of polyurethane coating systems

We have studied a model system for a polyurethane (PUR) coating on ZnO. Typically, PUR coatings are cured in situ on the surface via a polyaddition of a bi- or higher functionalised isocyanate and an alcohol (in this work we use a hexandiol and a hexandiisocyante). To mimic the curing process we simulate three PURs of different chain length and analyse the local structure at the interface. Since PURs are commonly used as protective, anti-corrosive coating, we furthermore study the permeation of water in these systems. Especially at the early stages of the curing process the presence of water could influence the morphology of the polymer film quite drastically. In this work, we will present preliminary results on analysis of the structure and the water permeation in these systems. We identity open questions and propose ways to address these.

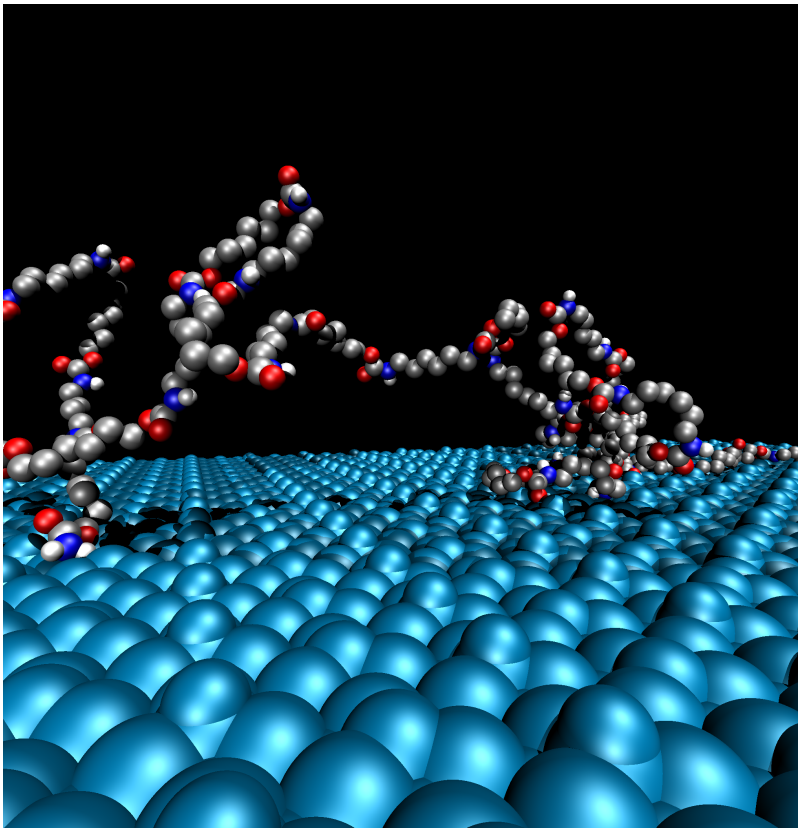

Figure 4.1: A polyurethane 20mer adsorbed on a ZnO(0001) surface.

4.1 Introduction

Polyurethanes (PURs) are commonly applied as protective coatings for vehicles and widely used in construction applications, e.g. as pipeline coatings. These coatings are applied as a mixture of two components, bi- or higher functionalised isocyanate and alcohols, which cure in situ on the surface to form a thin polymeric film. Macroscopic properties of the coating, such as the abrasion or the corrosion resistance, is on the one hand strongly dependent on the type of isocyanate and alcohol that are applied and on the other hand on the microscopic interplay between the surface and the polymeric mixture.[80,107–112] Since the PUR cures on the surface it is necessary that the mixture is homogeneously dispersed. Molecular dynamics (MD) simulations can provide a microscopic insight into how the PUR adsorbs on the surface. Bulk PURs have been studied in the past using experimental techniques[113–118] or quantum and classical simulations.[119–126] The hydrogen bonding in the polyurethane network is a central topic in the literature since the specific hydrogen bond pattern is believed to determine the mechanical properties of the PUR. In this work, we studied a model system for a PUR coating on ZnO(0001), which is formed by a polyaddition of hexandiisocyanate (HDI) and hexandiol (HD). We note that experimentally used PUR coatings can consist of higher molecular weight precursor units such as polyester- or polyether-diols, which are also widely studied in the literature.[113–115,119–122,124,126] The additional ether or ester group in polyester or polyether PURs provide another hydrogen bond acceptor and therefore the inter- and intra-molecular conformations can be different from the PURs ones. However, a less complex model, which we studied in this work, contributes in a similar way to analyse the hydrogen bond network and the influence of water in these networks.

In previous work, we have developed a force field to model the adsorption of water on ZnO(0001).[17] This surface is experimentally very well characterised[87] and can often be found as the top layer of vehicle bodies. To mimic the different stages of the curing process, we have simulated three different PURs in contact with ZnO(0001), which differ in chain length of the PUR: N-Ethylurethane (N-EU) (a short carbamate), a 3mer and a 20mer. We have furthermore studied the water permeation in these systems by adding a weight fraction of 5% water to the systems. In the past, atomistic MD simulations have proven to be a powerful tool to study permeation of additives in polymers in the past.[127–138] In a PUR coating system, water should be ideally be avoided in the coating process since it can react with the

isocyanate group to form a urea component and carbon dioxide. This does not only influences the reaction equilibrium of the polymerisation process but also bubbles can occur in the coating layer due to the escaping carbon dioxide. Therefore, we have analysed the water structure and permeation at different stages of the curing process. We note that HDI can in principle react with the hydroxyl groups of the ZnO surface. We will not consider chemisorption in our simulations and just focus on the nonbonded interaction between the PUR and the substrate. This work presents the first, preliminary results of our research and can therefore give only at most a rough, qualitative picture. However, we will discuss in the outlook, section 4.5, which analysis are still missing to complete the research picture.

This work is structured as follows: In section 4.2 we discuss the PUR model used in this work. In section 4.3 details about the simulations are provided. This is followed by a discussion about the local structure of the PUR-water systems and PUR-ZnO systems with a weight fraction of 5% water (section 4.4.1) and a qualitative study of the water permeation of the PUR in contact with ZnO (section 4.4.2). A summary and an outlook is given in section 4.5.

4.2 Model

We have performed simulations of PUR of different chain length in contact with partially OH-terminated ZnO(0001) [17]: The short carbamate, which is represented as N-Ethylurethane (N-EU), a 3mer and a 20mer. The PUR is formed by a polyaddition of two components, hexandiol and hexandiisocyanate. Structural formulas are shown in Fig. 4.2 and Fig. 4.3.

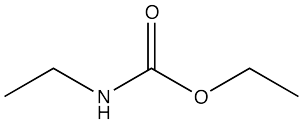

Figure 4.2: Structural formula of N-Ethylurethane.

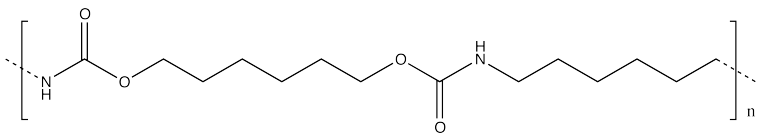

Figure 4.3: Structural formula of the polyurethane formed by a reaction of hexandiol and hexandiisocyanate.

For the atomistic simulations of the N-EU and the PUR 3mer and 20mer, we used the OPLS united-atom (UA) force field.[35] We have validated the force field against experimental data for density and surface tension[139]. Detailed information about the nonbonded parameters of the force field can be found in Tab. 4.1. The partial charge of the CH_2 UA, which is bonded to the oxygen of the carbamate group was set to 0.4 to guarantee intermolecular charge neutrality. The bonded parameters have not been modified in the course of the force field development and have been taken from the OPLS-UA force field.[35]

atom type	σ (nm)	ϵ (kJ/mol)	partial charge
CH_3	0.39050	0.73220	0.00
CH_2	0.39050	0.49371	0.20
N	0.32500	0.71128	-0.57
H	0.0	0.0	0.37
OC	0.29600	0.87864	-0.50
C	0.37500	0.43920	0.50
OS	0.30000	0.71128	-0.40
CH_2	0.39050	0.49371	0.40
CH_3	0.39050	0.73220	0.00

Table 4.1: Nonbonded force field parameters..[35] The atom types are listed according to their connectivity in the molecule. OC refers to the carbonly oxygen and OS to the oxygen connected to the alkyl group (see Fig. 4.2 and Fig. 4.3).

The force field for N-EU predicts the density at room temperature in close agreement with experiments (see Tab. 4.2). Furthermore, the surface tension at various temperatures is in good agreement with the experimental values. All data can be found in Tab. 4.2. At 333 K we observe the biggest discrepancy, which is close the freezing point (336 K) and hence the system exhibits slower dynamics, which makes equilibration harder.

	Temp. [K]	Experiment	Simulations
Density [g/cm^3]	298	983.8	981.0
Surface tension [dyn/cm]	333	31.8 ± 0.3	29.4 ± 2.1
	353	29.9 ± 0.3	29.6 ± 2.0
	373	27.9 ± 0.3	30.8 ± 1.9
	423	22.9 ± 0.3	19.0 ± 2.3

Table 4.2: Density and surface tensions obtained by simulations with a UA force field and experiments.[139]

The force field of the PUR is based the N-EU force field. The missing bonded potentials for the alkyl units are taken from the OPLS-UA force field as well. The

interaction of the PUR with the surface is modelled using a geometric combination rule. At this point of the work, the accuracy of the PUR-ZnO force field cannot be entirely judged. With adsorption energies for N-EU in contact with ZnO of around 80 kJ/mol, we are confident that we reach qualitative agreement. However, further detailed quantum calculations are still in progress in order to validate the results found in this work.

Since there are no experimental data for this specific PUR system available, we have simulated a system of 25 chains of PUR 20mers at different temperatures to determine the glass transition temperature for this system. In Fig. 4.4 the temperature dependence of the density is shown. The glass transition temperature for this systems is around 400 K, which motivated us to use a temperature of 500 K for the subsequent simulations of the PUR melt.

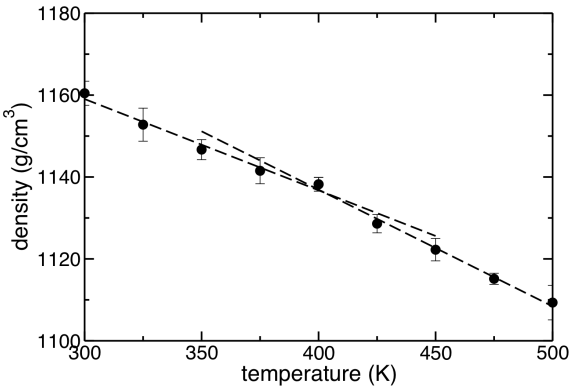

Figure 4.4: Temperature dependence of the density for a system of 25 chains of PUR 20mers. The dashed lines show a linear fit of two temperature regimes. All systems were equilibrated 5 ns each temperature.

4.3 Computational details

For equilibration we have performed NpT simulations of bulk systems of N-EU, 333 chains of a PUR 3mer and 25 chains of a PUR 20mer using the GROMACS simulations package.[98] Details of the force field can be found in the previous section 4.2 All simulations are done at a pressure of 1 atm using a Parinello-Rahman barostat[140,141] (τ_p=1ps) and at 298 K and 500 K for a liquid of N-EU and the PUR melts, respectively. The temperature coupling is performed using a Nose-Hoover thermostat[142,143] with a $\tau_t = 0.1ps$. The bonds are constrained using the LINCS algorithm[144] and the integration time step is 2 fs. The equilibration times are 50 ns.

For the systems in which the polymer is in contact with the ZnO(0001) surface, we add a vacuum in the z-direction to the simulation box and equilibrated the free standing polymer surfaces. Two layers ZnO(0001) are afterwards added to both sides of the system in z-direction. An energy minimisation of the systems are followed by a 50 ns equilibration run under NVT conditions.

For the systems which include 5% of water by mass the SPC water model[100] is applied. Initial configurations are obtained using the Packmol software.[145] The production runs are performed for 60 ns.

Details about the ZnO(0001) surface can be be found in Ref. [17].

4.4 Results and discussion

We have simulated three ZnO-PUR systems, which differ in the chain length of the PUR in order to mimic the different stages of curing of PUR on the surface: N-EU, PUR 3mer melt and PUR 20mer melt. 5% of water by mass is added to these systems to study the influence of water during the curing process and in the final PUR coating.

In the following section 4.4.1, we will firstly study the local structure and the hydrogen bonding network in the bulk PUR systems with a water content of 5%. Secondly, we analyse the local structure of three different PURs and water at the interface. The permeation of water in the three different systems is discussed in section 4.4.2. As mentioned before, the results, which are presented in this section, should be seen as preliminary work for a further, more detailed study. Therefore, we can only draw qualitative conclusions, which are then validated and extended in future work.

4.4.1 Structure

4.4.1.1 Bulk PURs-water sytems

We study the local structure of water in the three different bulk PUR systems with a 5% water content to analyse the influence of water on the PUR hydrogen bonding network. From the analysis of the radial distribution functions (RDFs) of bulk PURs systems, we can see that hydrogen bonding occurs predominately between the carbonyl oxygen and the hydrogen of the urethane group. This is in agreement with what has been found in the literature.[114,115,120,122] For the shorter chain PURs this

hydrogen bond is more pronounced, which is probably due to the local packing and steric differences between the three PURs.

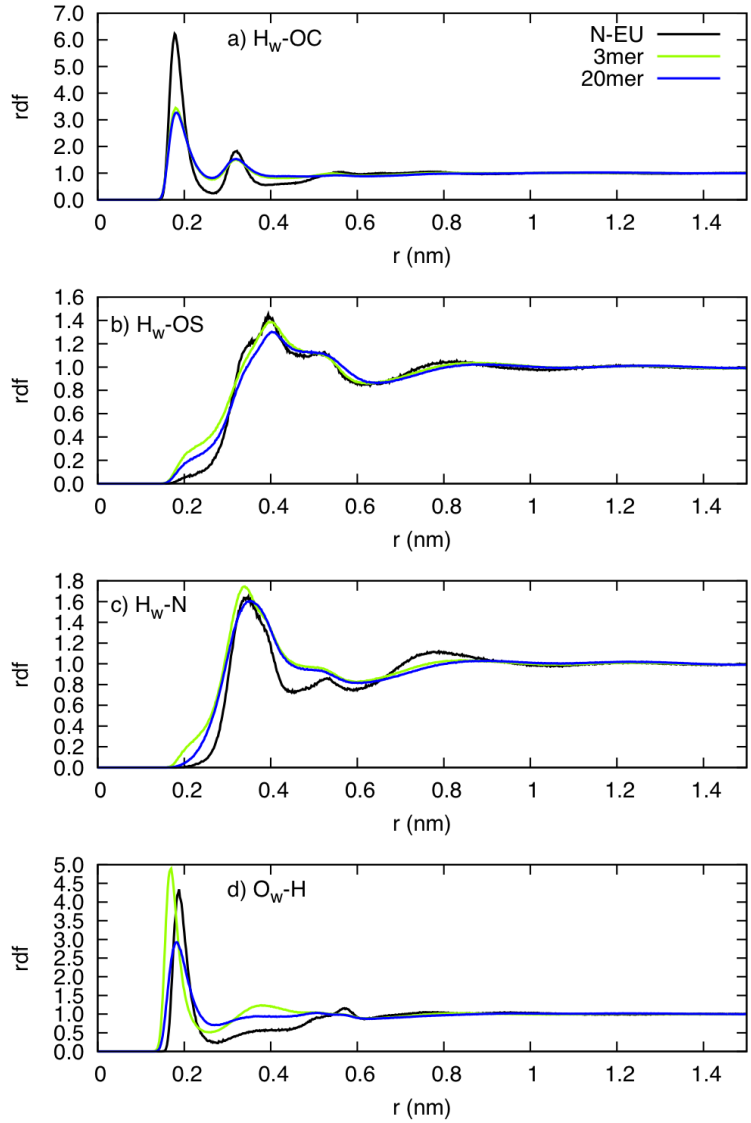

Figure 4.5: Radial distribution functions of different atom types of the urethane group with water for the three different PUR systems. OC refers to the carbonyl oxygen and OS to the oxygen bonded to the alkyl group (see Fig. 4.2 and Fig. 4.3).

To study the influence of water on the hydrogen bonding network, we calculated the RDFs for the different atom types of the urethane group and water, which are shown in Fig. 4.5. Characteristic hydrogen bonding can be observed between the water oxygen (O_w) and the urethane hydrogen (H) as well as between the water hydrogen (H_w) and the carbonyl oxygen (OC). It is especially striking that the peak height of the H_w-OC RDF decreases for the 3mer and 20mer system in comparison to the liquid N-EU. We speculate that due to higher thermal motion in the liquid it is

easier for water to break the hydrogen bonding network of N-EU. In the PUR 3mer and 20mer systems, breaking of an hydrogen bond is accompanied by local conformational changes of the polymer, which might be energetically less favourable. In this context it would be interesting to analyse the fraction of saturated and unsaturated hydrogen bonding donors and acceptors in the pure PUR system and in the one containing 5% water. This would show if water indeed breaks up the hydrogen bonding PUR network or if it forms hydrogen bonds with mostly previously unsaturated carbonyl oxygens of the urethane group. From the calculation of the average number of hydrogen bonds per 10 ps timeframe in the bulk PUR systems and in the systems containing additionally 5% water by mass, we can observe a decrease of the average number of hydrogen bonds in the systems containing water in comparison to the pure PUR bulk systems. The decrease is around 17% for N-EU and 25% for the 3mer and 20mer systems. This indicates that indeed water breaks up the PUR hydrogen bond structure. However, further analysis are needed to quantify these results.

4.4.1.2 PURs-ZnO systems

In this section we analyse the local structure at the interface of the N-EU, a PUR 3mer and a PUR 20mer in contact with ZnO. These systems contain additionally of 5% water by mass. By studying the number density profiles of different atom types of the urethane group (H, OC, OS and N), we can get a first idea of how the PUR adsorbs to the substrate. The corresponding density profiles in Fig. 4.6. In the case of N-EU, the shortest urethane molecule, the number density in in the direct proximity to the surface is similar for all four atom types. Due to thermal motion the liquid, no preferential adsorption for either of the urethane atoms can be observed. The N-EU density profile shows secondary peaks only in the N-EU. This is typical for a liquid structure and it is therefore no longer present in systems with a higher molecular weight PUR. In PUR 3mer and 20mer we can see more differences in the density profiles in comparison to the N-EU system. The nitrogen, the carbonyl oxygen (Fig. 4.6b) and d)) and the hydrogen (Fig. 4.6a)) of the urethane group are closest to the ZnO surface, whereas the oxygen, which is bonded to the alkyl group and indicated as OS in Fig. 4.6c), is on average further away from the surface. This is most likely due to sterical hindrance of the alkyl group. In the simulation of the 20mer PUR melt on ZnO we predominantly find structures, in which the polymer forms so called loop conformations. An example of such a conformation can be seen

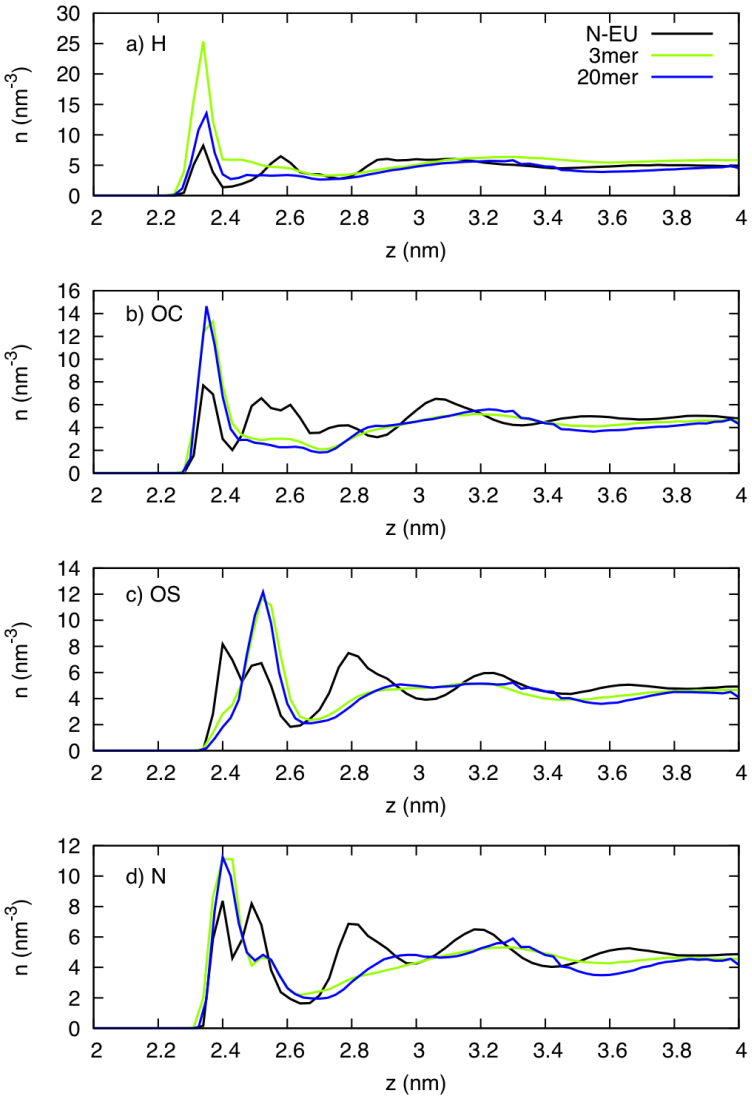

Figure 4.6: Number density profiles n of different atom types of the urethane group for three differ PUR-ZnO systems. OC refers to the carbonyl oxygen and OS to the oxygen bonded to the alkyl group (see Fig. 4.2 and Fig. 4.3). For all three systems the surface is 2.321 nm thick.

in Fig. 4.1. To strengthen these results, we plan to analyse the inclination of the planar urethane group with respect to the surface.

Furthermore, we have calculated RDFs between the urethane group and the surface hydrogen (H_s) and oxygen (O_s) as shown in Fig. 4.7 and 4.8. By doing so, we can determine preferential adsorption sites of the three different PURs on the surface. We note that the normalisation has been performed based on a homogeneous systems, whereas in fact the system is heterogenous due to presence of the surface. This is the reason why the RDFs in Fig. 4.7, 4.8 and 4.9 do not converge to one but show multiple peaks at larger distances r. However, the first peaks of

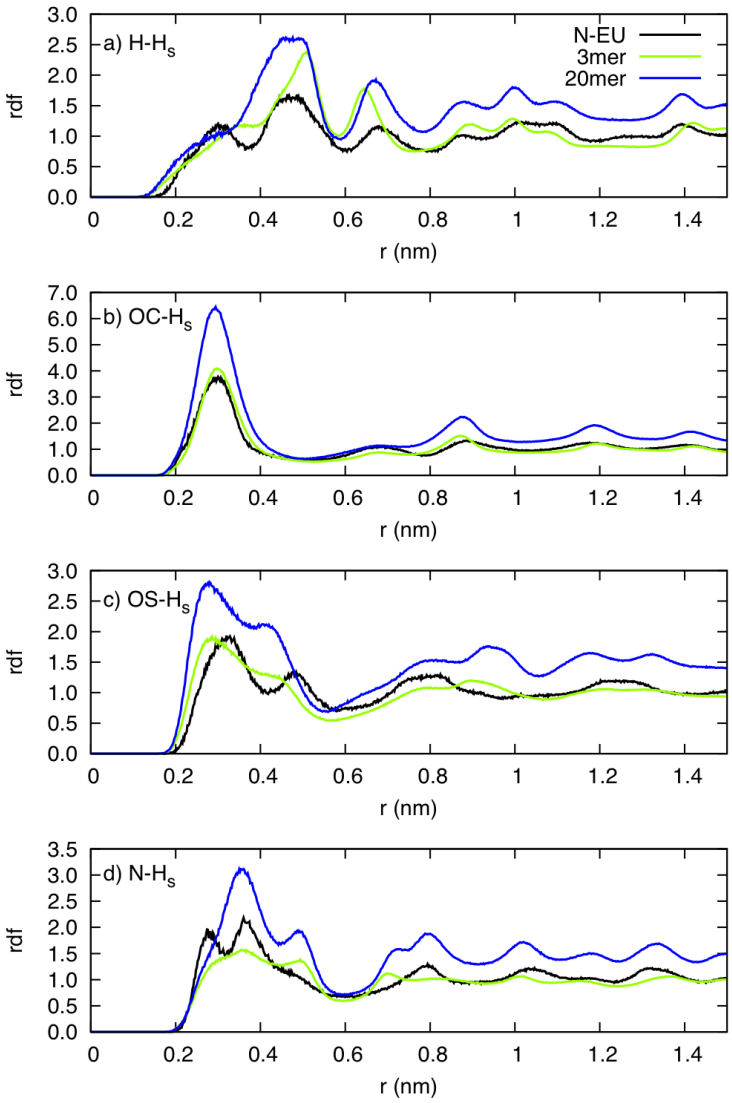

Figure 4.7: Radial distribution functions of different atom types of the urethane group and the surface hydrogen for the three different PUR in contact with ZnO(0001). OC refers to the carbonyl oxygen and OS to the oxygen bonded to the alkyl group (see Fig. 4.2 and Fig. 4.3).

the RDFs are still meaningful since they correspond to the closest distance of the atoms of the urethane group to the different surface atoms. Firstly, we focus on the RDFs of the urethane group with surface hydrogen. Also here, we can observe more distinct trends for PURs with longer chain lengths. For example, in Fig. 4.7a) and d) we can see for the N-EU system a peak around 0.3 nm, which appears only as small shoulders in the 3mer and 20mer systems. This means that preferential adsorption sites are more noticeable in the PUR 3mer and PUR 20mer systems. One of which can be determined as the interaction of carbonyl oxygen with the surface hydrogen, indicated by the highest peak intensity of the RDFs for all three systems

(see 4.7b)). Furthermore, the nitrogen and oxygen, which is bonded to the alkyl group, also shows a relatively strong interaction with the surface hydrogen. These are hydrogen bond donor-acceptor interactions. In Fig. 4.8 we show the RDF of the

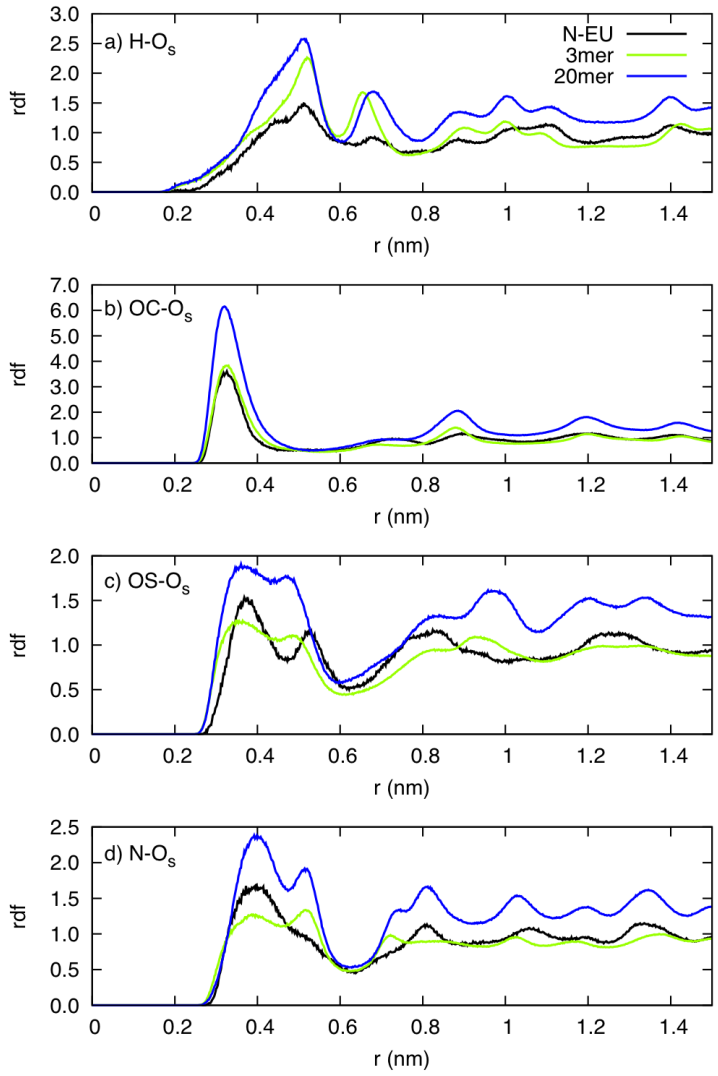

Figure 4.8: Radial distribution functions of different atom types of the urethane group and the surface oxygen for the three different PUR in contact with ZnO(0001). OC refers to the carbonyl oxygen and OS to the oxygen bonded to the alkyl group (see Fig. 4.2 and Fig. 4.3).

urethane group with the surface oxygen. The peak structure of the RDFs is similar to the one with surface hydrogen H_s (compare Fig. 4.7 and 4.8). We note, that the hydrogen bonding between the urethane hydrogen and the surface oxygen O_s cannot be observed.

Overall, one can see from the analysis of the RDFs and the number density profiles that the urethane group adsorbs on the surface. While urethane oxygens, especially the carbonyl oxygen, show strong interactions with the surface hydrogen, we cannot

find an indication for a hydrogen bond of the urethane hydrogen with the surface oxygen. However, as already mentioned throughout this work, further structural investigations, which can strengthen this results, are needed to draw quantitative conclusions.

Lastly, we show in Fig. 4.9 the RDFs of the surface hydrogen H_s with the water oxygen O_w as well as the RDFs of the surface oxygen O_s with the water hydrogen H_w. The RDFs of the water oxygen O_w show a peak at the classical hydrogen bonding distance of about 0.19 nm for all three systems, respectively (see Fig. 4.9b)). A second and third peak of a higher intensity occurs at larger distances, which shows high structuring of water at the interface. Fig. 4.9a) indicates that there is no direct interaction between the water hydrogen H_w and the surface oxygen O_s, which is consistent with the results from the RDF of the urethane group with the surface hydrogen and oxygen (compare Fig. 4.7 and 4.8). Overall, we can see in Fig. 4.9 that

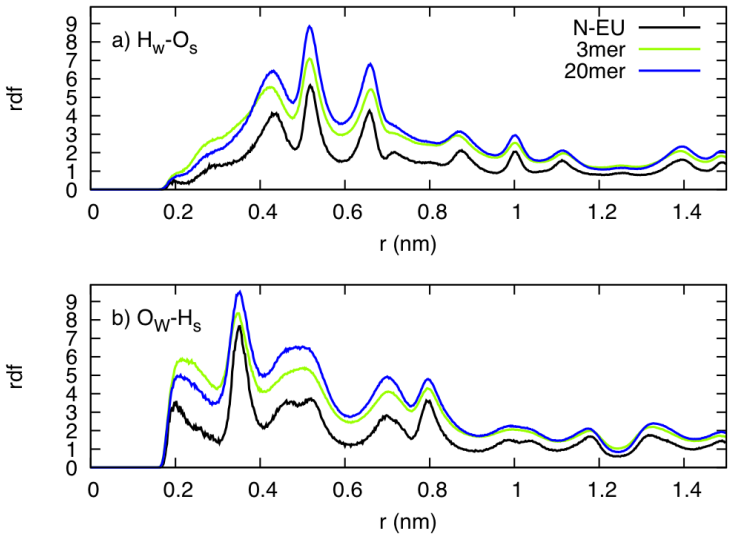

Figure 4.9: Radial distribution functions of the water hydrogen H_w with the surface oxygen O_s and the water hydrogen O_w with the surface oxygen H_s for the three different PUR in contact with ZnO(0001).

the peak structure is similar for all three PUR systems. However, the peak intensity is different. It increases with the length of the PUR chain. This can be due to difference in the local packing, which consequently results in a the free volume differences of the PUR chains at the interface.

4.4.2 Water permeation

PURs are commonly used as protective, barrier coatings to prevent water from permeating through the polymer towards the surface. However, since they are cured in situ on the surface at ambient temperatures the presence of water cannot be ruled out completely during this process. Ideally, the presence of water should be avoided because side reactions of the isocyanate group with water can influence the curing process. To understand and optimise such curing processes it is important to have a microscopic insight into these systems. Therefore, we have studied the permeation of water in three different PUR-ZnO systems.

In Fig. 4.10 the amount of water in the bulk region of the PUR and at the interface with ZnO is determined over a simulation time of 60 ns. The bulk and the interface region are defined as slabs of 1 nm thickness. In the starting configurations the water is randomly positioned in the PUR. For all three systems we can observe the trend that over time the water concentration at the interface increases, whereas the concentration in the bulk polymer decreases. The directional diffusion towards the interface is fastest for the PUR 20mer system and the slowest for the system containing the liquid of N-EU. A reason for this can be the difference in the local packing of the PUR systems with different chain length. We can observe this trend also in the diffusion of water in bulk PUR systems. Water in bulk N-EU has a diffusion coefficient of 0.169×10^{-5}cm/s, in the 3mer the diffusion is 1.015×10^{-5}cm/s and in the 20mer 1.623×10^{-5}cm/s.

As mentioned before, the PUR curing should ideally be carried out in absence of water since the isocyanate can react with water to form a urea derivate and carbon dioxide. However, it is experimentally very difficult to provide these conditions. We study the water permeation in the early stages of the curing process, mimicked by the N-EU-ZnO system, to understand the influence of water on the curing process. We consider two different initial configurations: A layer of water in the bulk (shown in the inset of Fig. 4.11c)) and a water layer at the interface mimicking a prewetted surface (shown in the inset of Fig. 4.11b)). The permeation of water in these systems is then compared to the results from simulations where the water is randomly distributed in the liquid of N-EU (see inset of Fig. 4.11a)). Fig. 4.11c) shows that on a time scale of 60 ns most of the water permeates from the bulk to the interface and accumulates there. Similar behaviour can be observed in the system where the water is randomly distributed across the N-EU (compare Fig. 4.11a)). In case of a

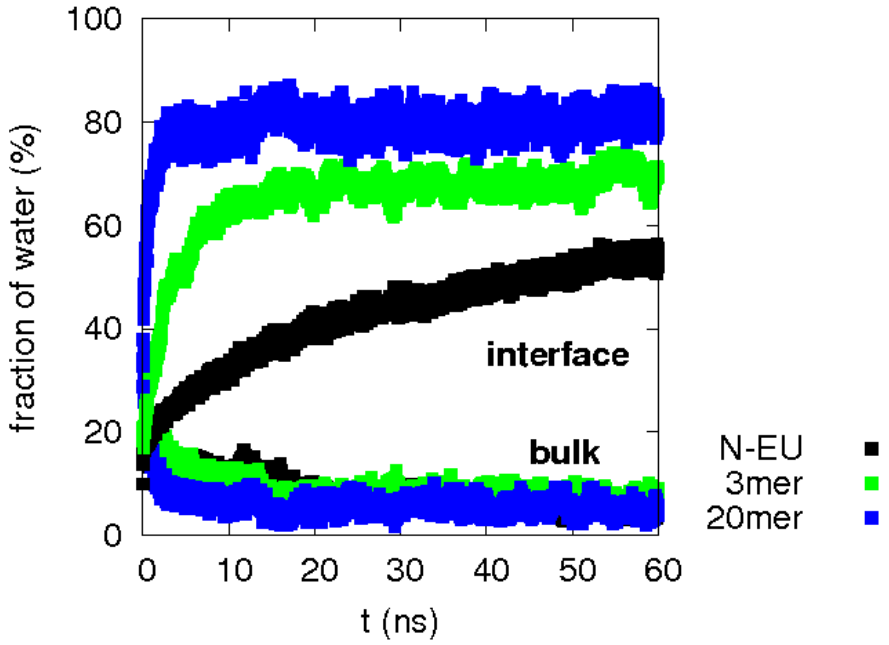

Figure 4.10: Water permeation in the three different PUR systems. The fraction of water at the interface (upper three curve) and in the bulk (lower three curves) is plotted against the time. The interface and bulk region are defined as slabs of 1 nm thickness.

prewetted surface, shown in Fig. 4.11b), the water stays at the interface and does not diffuse to the bulk over a period of 40 ns. In a real application of a curing process of a PUR a prewetted layer on the surface is likely to be present due to atmospheric humidity. A competative situation regarding the adsorption on the surface between water and PUR might occur, which can influence the stability and adhesion of the polymer film. However, this result is strongly dependent on the interaction strength of the adsorbent with the surface and how well the force field can describe it. At this point of the work, the accuracy of the PUR-ZnO force field cannot be entirely estimated. With adsorption energies for the N-EU in contact with ZnO of around 80 kJ/mol, we are confident that we reach qualitative agreement. However, further detailed quantum calculations are to be made to validate the results found in this work.

4.5 Summary and outlook

We have presented preliminary results for a model system for a PUR coating on ZnO. Commonly, the PUR is cured in situ on the surface. To study the different

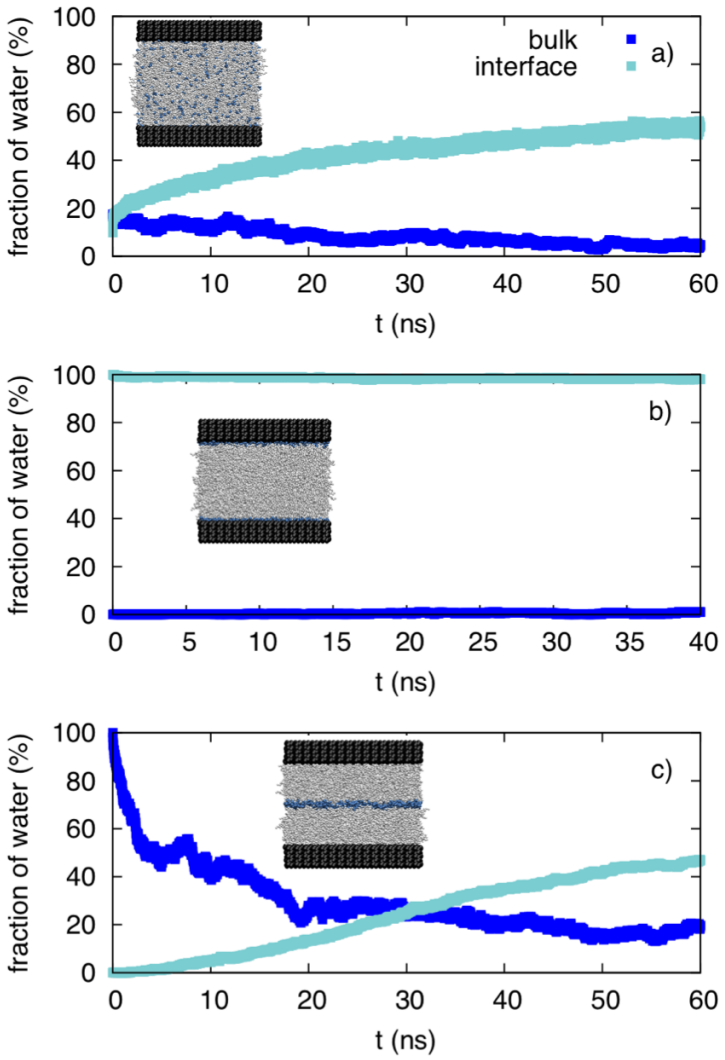

Figure 4.11: Water permeation in three N-EU-ZnO system with different starting configurations (shown in the insets). The fraction of water at the interface and in the bulk is plotted against the time. The interface and bulk region are defined as ares of 1 nm thickness. The water layer is 0.5 nm thick.

curing stages, we simulated systems containing PUR of different chain lengths: the short carbamate N-EU, a PUR 3mer and a 20mer. The three PURs are in contact with ZnO and contain 5% water by mass. Radial distribution functions and density profile analysis showed that the urethane group is adsorbing on the surface, whereby the urethane oxygens, especially the carbonyl oxygen, can be found in closest proximity to the surface hydrogen. The water oxygen hydrogen bonds with the surface hydrogen and forms a layer on the surface. Analysis of the water permeation have shown that independently of the starting configuration, a stable water layer is formed at the surface with time. This is especially important since the presence of water can

influence the curing process and therefore the adhesion and stability of the polymer film. However, at this point of the work we still face some open questions, some of which we have addressed throughout this paper. A detailed study about the lateral water diffusion along the surface and the perpendicular water diffusion away from the surface is needed to quantify the stability of the first water layer at the interface. During the curing of the coating, we assume to have a competitive adsorption situation between water and PUR on the surface, which strongly influences the stability of the polymer film and should be analysed in more detail in order to get a better microscopic picture of the curing and adsorption processes. In order to describe the competitive adsorption between between water and PUR accurately it is important that the force field can model the energy barriers between different adsorption states correctly. Therefore, further validation using quantum calculations are needed to validate the PUR-ZnO force field. Additionally, simulations of the curing reactants, the diisocyante and the diol, would give further insight into preferential adsorption behaviour and the subsequent starting conditions for the curing process.

5 Hierarchical modelling of polymer permeation

We propose an hierarchical modelling approach to calculate diffusion coefficients and excess chemical potentials of large (non-gaseous) penetrants in polymer melts. The sequence of procedures described in this work includes accelerated, coarse-grained molecular dynamics simulations of penetrant diffusion, inverse mapping of coarse-grained melt structures, and application of nonequilibrium free energy calculations to determining penetrant excess chemical potentials in well-relaxed atomistic melt configurations. Based on the application to ethylbenzene permeation in polystyrene melts, we discuss how the use of hierarchical models leads to a computationally efficient prediction of permeation data in quantitative agreement with experiments. The procedures outlined in this paper may find future application in modelling permeation in complex, soft matter systems.

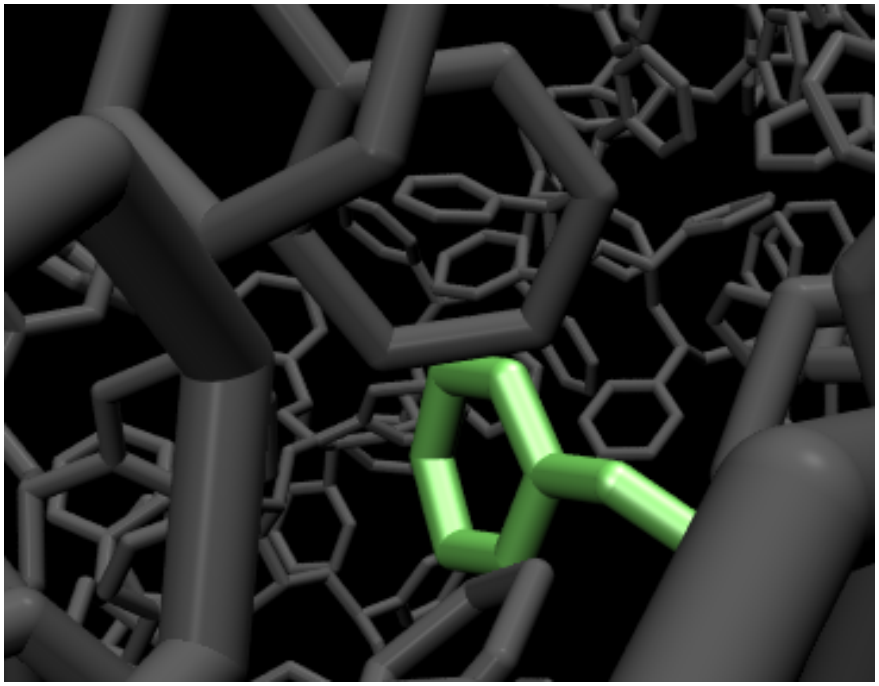

Figure 5.1: Ethylbenzene in a melt of atactic polystyrene.

5.1 Introduction

Computational modelling of polymer permeation started with the diffusion of gases in amorphous polymer melts and glasses during the early 1990s.[127–134] These early molecular dynamics (MD) simulations uncovered the diffusion mechanism of small penetrant molecules which involves a series of discrete jumps between small cavities in the polymer matrix on time scales typically of the order of 100 ps in molten or rubbery polymers and up to microseconds (and longer) in glassy polymers. Owing to the fact that the time scale for the penetrant's diffusive motion only weakly couples to the time scales for chain segmental relaxations and diffusion, gas diffusion constants can be computed quantitatively, even in "slow systems" for which coarse-grained, transition state methods have been developed.[132,133,146]

In many applications and industrial processes, not only the diffusion of gases but also the diffusion of larger penetrant molecules or additives such as solvents, plasticisers, residual monomer, or other impurities is of significant interest. All-atom MD simulations of such systems, however, are computationally expensive, in particular close the glass transition temperature where it becomes cumbersome, if not impossible, to reach the diffusive time scale where the penetrant's mean square displacement grows linear in time. Because also the equilibration of chain conformations in the pure polymer melts becomes difficult, atomistic simulation approaches are of limited use only. Alternative simulation approaches that provide permeation data for these types of "slow" systems have not been systematically studied so far.

The first scope of this paper is to propose a procedure to overcome the above-described limitation by using coarse-grained (CG) molecular dynamics simulations. Here, coarse-graining refers to the process of replacing an all-atom polymer (and penetrant) model with a simplified model that explores configuration space much faster during the course of a MD simulation.[147–152] The "beads" of the CG models that we employ represent 5-10 atoms of the parent, all-atom model and interact with other beads through a set of bonded and nonbonded CG potentials, which are systematically derived from all-atom simulations.[148,149,152,153] Such a CG polymer representation is still detailed enough to accurately represent the local chain stiffness and conformations, as well as the packing of chain segments in the amorphous melt. We shall be concerned with ethylbenzene (EB) diffusion in atactic polystyrene (PS) and employ a level of coarse-graining in which an EB molecule is represented by two spherical beads and the polymer repeat units are modeled with two CG beads each.

At this CG level of description, the system is modeled with significantly fewer degrees of freedom, however the distribution of empty, molecular-sized cavities, which may potentially hold an EB molecule, can still realistically be described.[150] As was shown previously,[150] such a simple, CG model description can be used to obtain quantitative estimates of the EB tracer diffusion coefficient over a range of experimental temperatures. Moreover, the demand on computer time required to obtain these data can be reduced by approximately 4 orders of magnitude compared to detailed atomistic models. This successful application to penetrant diffusion is largely owing to the CG model, which reproduces the PS segmental dynamics in agreement with the atomistic model at the smallest possible length and time scales it resolves.[149,151] These scales correspond to the dimension of the individual beads (4-5 Å) and the corresponding time scales of their displacement (∼100 ps).

The approach to arrive at a quantitative description of EB dynamics in PS melts requires a "time mapping" in which an experimental or simulated dynamic property, or the corresponding mean square displacement observed in all-atom MD simulations, is mapped onto the corresponding quantity observed in CG simulations. In previous work, reported in Ref. [150], this procedure was applied at different temperatures and resulted in an apparent Arrhenius form of the time mapping constant. This result was interpreted by assuming that the time mapping constant is composed of two contributions that can be treated separately. Since the additive diffusion mechanism is a hopping motion which is coupled to the dynamics of the polymer chains[154], the first contribution was assumed to describe the EB hopping dynamics relative to the motions of the chains. This contribution can qualitatively be described with an Arrhenius function if the motion in the CG system is considered to take place on a smoother energy surface than that of the all-atom system. The second contribution was assumed to follow the time mapping of the chain dynamics between the all-atom and CG systems whose temperature dependence is the same in the atomistic and CG systems.

The EB dynamics is significantly faster in a CG simulation (which makes the simulation computationally cheap) and can be mapped onto a physically realistic time scale through a time mapping procedure with a known dependence on the system's temperature. Clearly, the overall procedure offers a new, powerful route to predict diffusion coefficients at temperatures where neither all-atom simulation nor experiments are feasible. The time mapping procedure used in Ref. [150] is investigated in this work over a larger range of temperatures with a new CG polystyrene model.[152]

It will be shown that the overall time mapping for EB diffusion can accurately be described with a Vogel-Fulcher temperature dependence which allows for quantitative predictions of the EB tracer diffusion coefficient down to temperatures close to the experimental T_g. This result moreover indicates that the separation of the time mapping factor into a contribution deriving from EB hopping (relative to the polymer matrix) and a contribution deriving from the coupling of EB dynamics to the dynamics of the chains is an oversimplified description.

The second scope of this paper is to calculate thermodynamic activity coefficients (excess chemical potentials) of EB in PS over a broad temperature range using a previously described nonequilibrium free energy calculation method.[155,156] Penetrant activity coefficients corresponding to infinite penetrant dilution in the polymer, are particularly difficult to obtain experimentally. Provided that sufficiently accurate all-atom force fields are available, these nonequilibrium free energy calculations have previously shown to provide an efficient route to predict solvent activity coefficients which are difficult to obtain from molecular simulations using alternative free energy calculation methods.[155–157] The atomistic representations of the PS matrix, required in these calculations, is obtained by inverse mapping of PS melts equilibrated with the CG model. Predictions obtained for infinite dilute ethylbenzene activity coefficients with two PS and EB force fields will be presented and compared with experimentally reported data.

5.2 Hierarchical models

5.2.1 Atomistic models

For atomistic simulations perfrormed in this work we used two different models. An all-atom (AA) model[135] of Müller-Plathe and the TraPPE united-atom (UA) model of Siepmann and coworkers,[158] which already includes a level of coarse-graining by having the atoms in CH, CH_2 and CH_3 groups merged into single interaction sites. We used both models for the calculation of EB excess chemical potentials by fast-growth thermodynamic integration (FGTI).[155] To study the diffusion of ethylbenzene in a matrix of long polystyrene chains we used the all-atom model and compared the results with those obtained with the TraPPE united-atom model used in a previous study.[150]

In the all-atom description each PS monomer is described by 16 atoms (see Fig. 5.2). All bond length are constrained using the LINCS method .[144] All-atom PS

T (K)	ρ_{exp} (kg/m^3)	ρ_{AA} (kg/m^3)	ρ_{UA} (kg/m^3)
383	1004		1047±2
403	992		1038±2
423	980	997±2	1028±2
443	969		1018±2
463	956	984±2	1007±2
483	946		997±2
503	934	970±2	987±2

Table 5.1: Mass densities ρ of the pure PS system at different temperatures T and 1 atm and experimental densities ρ_{exp} for a PS system with M_W=9000 g/mol.[162] ρ_{AA} and ρ_{UA} are the mass densities predicted by the all-atom and united-atom models (M_W =9984 g/mol), respectively. All-atom and united-atom systems were obtained by inverse mapping of equilibrated CG melts.

melts were simulated under isothermal-isobaric (NpT) conditions at temperatures of 423, 463, and 503 K and 1 atm using the Berendsen thermostat (coupling time 1 ps) and barostat (coupling time 5.0 ps).[159] The mixed EB/PS systems were simulated under isothermal-isobaric (NpT) conditions at temperatures between 463 K and 593 K. For the mixed EB/PS systems we used the velocity rescaling thermostat[160] (coupling time 0.2 ps) independently for PS and EB. For nonbonded interactions a cutoff distance of 1 nm was used. Cutoff corrections were applied to energy and pressure using standard analytical expressions that assume a uniform density beyond the cutoff.[161] Coulombic interactions beyond the cutoff were treated by particle mash Ewald (PME)[99] with a direct-space cutoff of 1 nm and a grid spacing of 0.12 nm. The integration time step was 1 fs. Details about the AA model can be found elsewhere.[135]

In the united-atom description each PS monomer is described by 8 pseudo-atoms. United-atom PS melts were simulated under isothermal-isobaric (NpT) conditions at temperatures between 383 K and 503 K and 1 atm using the Berendsen thermostat and barostat. For nonbonded interactions a cutoff distance of 1 nm was used. As in the case of the all-atom model, bond lengths were kept fixed and cutoff corrections were applied to energy and pressure. The integration time step was 2 fs. Details about the UA model can be found elsewhere.[148,158] The mass densities obtained with the AA and UA models are shown in Tab. 5.1 together with the experimental data. The mass densities and EB diffusion coefficients obtained with the AA model at 10 % EB concentration are summarised in Tab. 5.2.

T (K)	D_{EB}^{AA} (10^{-5}cm^{2}s^{-1})	density (kg m^{-3})
503	0.16±0.03	952±2
523	0.26±0.03	942±3
553	0.55±0.03	922±3
593	1.02±0.05	897±4

Table 5.2: Simulated atomistic systems of PS/EB. The mass densities correspond to a pressure of 1 atm and a concentration of 10 % EB. The diffusion coefficients D_{EB}^{AA} refer to the the all-atom model and were obtained from simulated trajectories of 8 ns up to 20 ns for the higher and lower temperatures, respectively

5.2.2 Coarse grained model

To study the sorption and diffusion of ethylbenzene molecules in a matrix of polystyrene it is a precondition to generate well-equilibrated atomistic conformations of long polymer chains. For this purpose we use a coarse-grained model of polystyrene, which we developed recently.[152] The idea of coarse-graining is to reduce the number of degrees of freedom in the polymer model severely while statistical properties of the chains, like the local packing or chain dimension in melts, are still described properly. The CG model uses a 2:1 mapping scheme, representing each PS monomer by two CG beads (see Fig. 5.2), in contrast to 16 atoms in the all-atom description. Staying still close to the chemical structure of the polymer allows to reintroduce chemical details into the coarse-grained systems ("inverse mapping"). By that one gets well-equilibrated atomistic conformations, while the actual equilibration of the long polymer chains happens on the CG level. It is not only the reduced number of degrees of freedom in the system which makes coarse-grained simulations more efficient than atomistic ones, but also the much faster dynamics in the CG simulations. This leads to an overall speed-up by a factor of about 10^4.

The CG PS model has been developed based on the all-atom force field[135], which is used in this work as well. The model reproduces the density of the all-atom model at ambient pressure and the local packing of chain segments in the melt in a temperature range between 400 K and above 530 K. Special attention was paid to the development of bonded potentials, which describe local distributions correctly for stereoregular as well as for atactic systems and take into account correlations between neighboring CG degrees of freedom. In that way chain dimensions are in agreement with atomistic simulations on all length scales beyond the CG bead size.

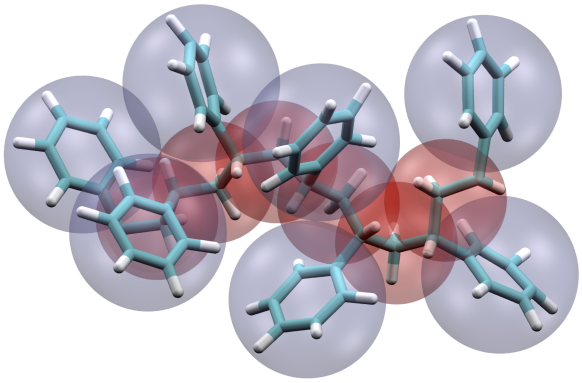

Figure 5.2: Mapping scheme: Each monomer is mapped onto two coarse-grained beads. Bead A is the center of mass of the CH_2-group and the two CH-groups, weighted with half of their masses. Bead B is the center of mass of the phenyl group. Fig. created with VMD.[97]

The systems we studied consist of 24 atactic chains with a length of 96 repeat units (192 CG beads) and a molecular weight M_W =9984 g/mol. Initial systems were prepared at temperatures of 423, 463, and 503 K by randomly placing 24 independent chain conformations in a simulation box at a density which is about 20 % below the final density. After a short steepest descent run the systems reach their final density in a NpT run of 2.5 ns. In the following the systems are simulated for about 1 μs under isothermal-isobaric (NpT) conditions at the respective temperature and 1 atm pressure using the Berendsen thermostat (coupling time 0.5 ps) and barostat (coupling time 5.0 ps). For nonbonded interactions a cutoff distance of 1 nm was used. The integration time step was 3 fs for the system at 503 K, 4 fs at 463 K and 5 fs at 423 K. Systems at other temperatures were obtained by cooling down the previously described systems and equilibration runs of 20 ns. Here we note that the dynamics and therefore also the timescale of the CG system is systematically different from the dynamics in atomistic simulations.[149] Comparing mean-square displacements $g_1(t)$ for all beads in this melt between the CG and corresponding all-atom simulations indicates faster dynamics in the CG system by a factor of about 25-30 (at 503 K).

Mixed systems of ethylbenzene and polystyrene were simulated with an EB weight fraction w_{EB} of 10 % (256 EB molecules), they are presented in Tab. 5.3. The EB molecules in the CG simulations were modeled by the beads also used for PS and the same nonbonded potentials. Mixed systems were obtained by randomly placing the EB molecules in the equilibrated PS matrices, followed by short steepest descent runs and NpT runs of 32 ns. Production runs of 96 ns to simulate the diffusion of

T (K)	D_{EB}^{CG} (10^{-5}cm^{2}s^{-1})	density (kg m^{-3})
398	1.4±0.1	999±2
423	2.0±0.1	987±2
433	2.4±0.1	981±2
448	2.8±0.2	974±2
463	3.25±0.1	967±2
473	3.6±0.1	961±2
503	4.6±0.2	946±2
523	5.3±0.3	935±3
553	6.6±0.4	917±3
593	7.9±0.2	892±3

Table 5.3: Simulated CG systems of PS/EB. The mass densities correspond to a pressure of 1 atm and a concentration of 10 % EB. The diffusion coefficients for these CG systems are not scaled to match with diffusion coefficients of atomistic systems.

EB were performed under isothermal-isobaric (NpT) conditions at 1 atm using the velocity rescaling thermostat[160] (coupling time 0.5 ps) independently for PS and EB and Berendsen barostat. All simulations in this work were performed with the GROMACS package.[98]

5.2.3 Inverse mapping

Having equilibrated coarse-grained systems as described before, we can reintroduce chemical details.[147,148,163,164] The systems have box sizes L^3 with L between 7.2 nm and 7.9 nm.

In a first step the atomistic chains with the correct tacticity are placed in a box, such that the center of mass of atoms representing CG beads coincide with the coordinates of the CG target system. During this first placement of the atomistic chains all inter- and intrachain nonbonded interactions are switched off.

Nonbonded interactions are switched on in a second step. Lennard-Jones (LJ) interactions are introduced by using a soft-core potential:

$$V_{sc}(r) = \lambda V_{LJ}(r_{sc}(r;\lambda)) \tag{5.1}$$

$$r_{sc}(r;\lambda) = \left[\alpha\sigma_{LJ}^6(1-\lambda) + r^6\right]^{\frac{1}{6}} \tag{5.2}$$

with a coupling parameter λ going from 0 (uncoupled) to 1 (fully coupled), V_{LJ} is the LJ potential, the LJ distance σ_{LJ} was set to 0.25 nm and the soft-core parameter α was set to 0.1. For the all-atom model the Coulomb interactions were introduced by linearly interpolating the partial charges from 0 to their normal value. This introduction of the nonbonded interactions causes the phenyl rings to rotate into orientations, where they are not overlapping or concatenated to each other. During this run the CG mapping points are still constrained to their target positions, therefore intersections of the chains are not possible. In the next step a full molecular dynamics NVT simulation is performed for 50 ps followed by a NpT simulation for 8 ns. For the pure PS systems we continued these runs and extracted a few starting configurations for the FGTI simulations at intervals of several nanoseconds. For the mixed EB/PS systems we started production runs at this point to simulate the EB diffusion.

5.3 Results and discussion

5.3.1 Time mapping and diffusion

We studied the diffusion of EB in a matrix of PS chains in all-atom and CG simulations. The self-diffusion coefficient D_i of component i ($i = 1,2$) in the binary polymer/penetrant system is calculated from the linear part of the mean-square displacement (MSD) of the center of mass of component i, $\left\langle (R^i_{\mathrm{cm}}(t) - R^i_{\mathrm{cm}}(0))^2 \right\rangle$, as a function of time using the Einstein relation:

$$D_i = \lim_{t\to\infty} \frac{\left\langle (R^i_{\mathrm{cm}}(t) - R^i_{\mathrm{cm}}(0))^2 \right\rangle}{6t} \tag{5.3}$$

To reach the linear part of the MSDs long trajectories are needed. For all-atom systems these simulations are computationally very expensive at the temperatures at which experimental data are available. Our strategy in the current work is to link diffusion coefficients from atomistic and CG simulations at higher temperatures by determining time scaling factors. By extrapolating these time scaling factors to lower temperatures we can compare the CG diffusion coefficients quantitatively to experimental data. The time scaling factor $s(T)$ is the ratio between the diffusion coefficients from CG and atomistic simulations, $D_{\mathrm{CG}}/D_{\mathrm{AA}}$.

In a first step we analysed the diffusion coefficients which we obtained from CG simulations in a temperature range between 400 K and 600 K (The CG model

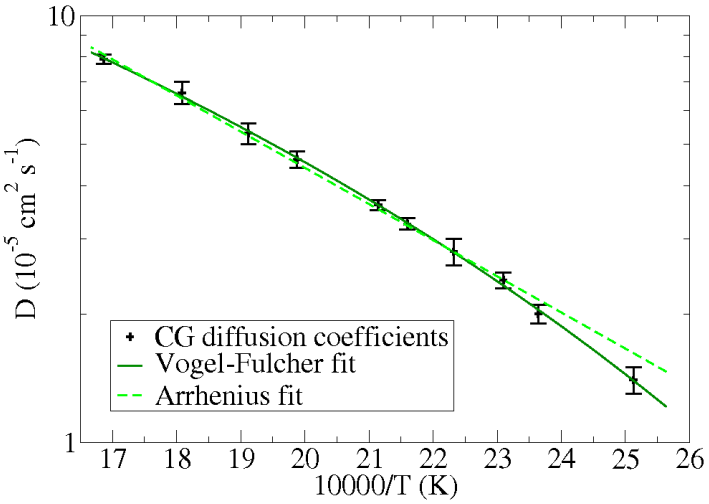

Figure 5.3: Fits of an Arrhenius and a Vogel-Fulcher form to the CG diffusion coefficients of 10% EB in PS. The diffusion coefficients for these CG systems are not scaled to match with diffusion coefficients of atomistic systems.

was developed at 503 K). It is known that CG simulations for polymer dynamics can reproduce the characteristic Vogel-Fulcher behaviour of diffusivity and bead friction exhibited by glass forming polymers.[163] A Vogel-Fulcher functional form, $D_{\mathrm{CG}}(T) = c\exp(-A/k(T - T_{\mathrm{VF}}))$, can be fitted to the CG data very well and delivers a $T_{\mathrm{VF}} = 185 \pm 30\,\mathrm{K}$ (see Fig. 5.3). Even though we study the diffusion of additives and not the one of the long polymer chains, the observed Vogel-Fulcher behaviour reflects that the mobility of additives is linked to the structural relaxation of the polymer melt, which includes the formation and destruction of larger cavities. This process happens on much larger time scales than the local spacial fluctuations of EB in these rather rugged cavities.[154]

If we assume that in the atomistic simulations the connection between penetrant diffusivity and structural relaxations of the melt is the same as in the case of CG simulations and if we assume the same Vogel-Fulcher temperature T_{VF} for the atomistic case, where we have not sufficient data to fit it directly, then the temperature dependence of the time scaling factor s also follows the Vogel-Fulcher equation:

$$s_{\mathrm{VF}}(T) = c_{\mathrm{VF}}\exp\left(\frac{A_{\mathrm{VF}}}{k(T - T_{\mathrm{VF}})}\right) \tag{5.4}$$

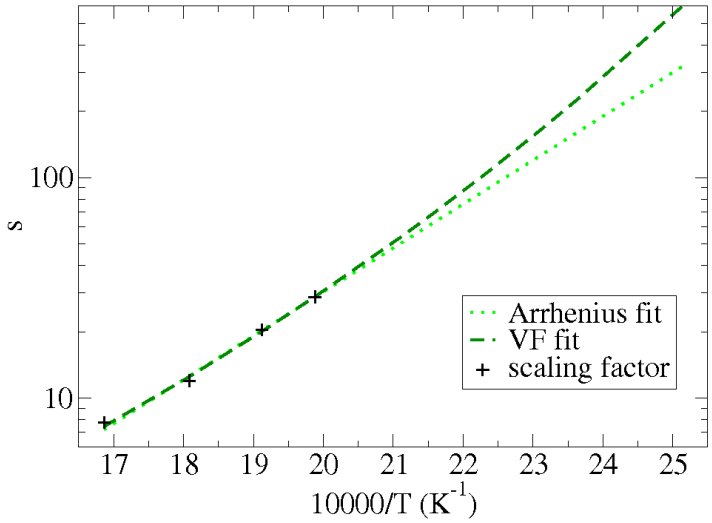

Figure 5.4: Fits of the time scaling factors $s = D_{\mathrm{CG}}^{\mathrm{EB}}/D_{\mathrm{AA}}^{\mathrm{EB}}$, obtained from the diffusion coefficients of EB.

We compare this assumption with another empirical way to describe the temperature dependence of s, which is the Arrhenius equation.

$$s_{\mathrm{Arrh}}(T) = c_{\mathrm{Arrh}} \exp\left(\frac{A_{\mathrm{Arrh}}}{kT}\right) \tag{5.5}$$

These functional forms are used to fit s at high temperatures (above 500 K). In Fig. 5.4 the fits for the Vogel-Fulcher form ($c_{\mathrm{VF}} = 0.062 \pm 0.008$; $A_{\mathrm{VF}}/k = 1952 \pm 50$ K; $T_{\mathrm{VF}} = 185$ K is set fixed) and for the Arrhenius form ($c_{\mathrm{Arrh}} = 0.0032 \pm 0.001$; $A_{\mathrm{Arrh}}/k = 4580 \pm 180$ K) are shown.

Applying the two relations for the time scaling factor from eq. 5.4 and 5.5 to the CG diffusion coefficients we can extrapolate the diffusion coefficients of the all-atom model D_{AA} to the range of experimental temperatures. These diffusion coefficients are shown in Fig. 5.5. The scaled CG diffusion coefficients agree with the atomistic ones for the four temperatures above 503 K, to which the time scaling factor was fitted.

The comparison of the CG simulations to experimental diffusion coefficients[150] shows a clear vertical shift. The scaled diffusivities D_{CG} are too low by a factor of 7 (at all temperatures) for the Vogel-Fulcher scaling and by a factor between 7 (at high temperature) and 3 (at low temperature) for the Arrhenius scaling. It is remarkable that the Vogel-Fulcher scaling predicts a temperature dependence which is in perfect agreement with the experimental data, whereas the Arrhenius scaling predicts higher

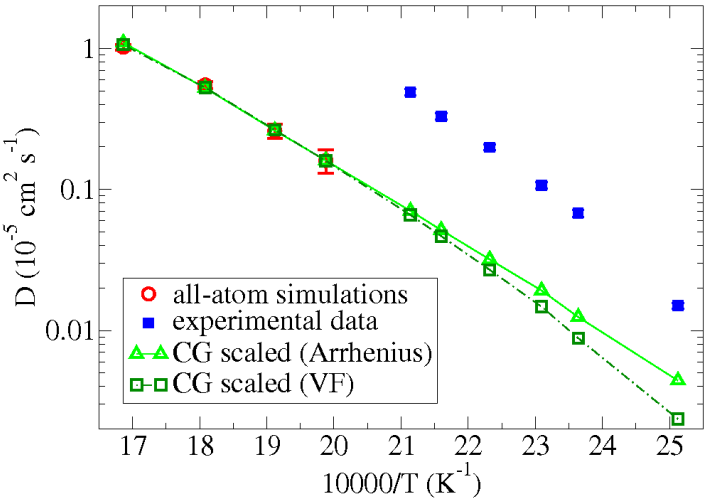

Figure 5.5: Diffusion coefficients from experiments,[150] all-atom simulations and scaled from CG simulations with an Arrhenius and a Vogel-Fulcher (VF) form for the temperature dependence of the scaling factor.

diffusivities for low temperatures. This is a clear indication that the CG model takes into account the structural aspects of the polymer matrix, which are responsible for the non-Arrhenius behaviour of the dynamics, but the non-Arrhenius behaviour also has to be taken into account for the time scaling factor.

To judge the quality of the simulation results we have to keep in mind two characteristic differences to an experimental setup, due to which simulated diffusion coefficients are expected to be lower compared to the experimental ones. First, the experimental sample is polydisperse ($M_W/M_n = 1.07$).[150] The presence of shorter chains in the experimental system contributes to faster dynamics, the extent of which can be large but probably not sufficient to explain the downward shift observed in Fig. 5.5. The second cause explaining the lower diffusion coefficients obtained from simulations is the density of the system which with the all-atom force field used in this work is predicted 2-4 % larger in comparison with experiment (see Tab. 5.1). This is not only an effect of the all-atom force field but also a consequence of the presence of short chains in experimental samples. A slight overestimation of the density has a strong effect on the system dynamics and easily explains a factor of 7. We note that in a recent work based on the same all-atom model, all systems were simulated at a constant volume corresponding to the experimental density.[151] There, a perfect agreement was obtained between the simulated and experimental polymer diffusion coefficients. Preliminary simulations of PS/EB mixtures performed under NVT conditions at densities chosen based on the experimental density of the pure polymer (and taking into account a solvent swelling contribution obtained from

the simulations) reduce the discrepancy between simulated and experimental diffusion data to a factor of 2. Taking into account these two aspects the agreement between simulated and experimental diffusion coefficients is excellent. Hence, the hierarchical simulation approach outlined here to quantitatively obtaining penetrant diffusion data from CG simulations follows a sequence of well-defined procedures that may find potential future application in modelling diffusion in complex fluids.

5.3.2 Excess chemical potentials

We have calculated excess chemical potentials (ECPs) of ethylbenzene in molten atactic polystyrene by using fast-growth thermodynamic integration (FGTI). This free energy sampling method is based on Jarzynski's nonequilibrium work theorem.[165] In FGTI multiple, independent TI runs are performed in which the coupling between the solute molecule and the polymer melt is introduced at finite rate. Each of the paths sampled during a FGTI run typically ends up in a local free energy minimum of the fully coupled end-state; i.e. at full coupling, the solute molecule occupies a cavity in the melt from which it does not move away during the simulation. But since the overall coupling time is of the order of a few nanoseconds, it is feasible to perform 50 – 100 independent FGTI runs, which together provide sufficient sampling of the fully coupled end state. Because the coupling is done at finite rate (rather than infinitely fast as it would be the case in e.g. the Widom test-particle insertion method) local chain relaxation, required to accommodate the solute, is being accounted for. Previous simulations indicate that FGTI runs with coupling times of 1-2 nanoseconds are sufficient to achieve this.[155] By running several FGTI one samples the nonequilibrium work W_{AB} which is performed in perturbing the system from state A to state B along a coordinate λ which couples the solute-polymer interaction. The excess chemical potential μ_{ex} is obtained in the following way:

$$\begin{aligned} \mu_{ex} &= -k_B T \log < \mathrm{e}^{-\beta W_{AB}} >_A \\ &= -k_B T \log \int_{\infty}^{-\infty} \mathrm{e}^{-\beta W_{AB}} P(W_{AB}) dW_{AB} \end{aligned} \tag{5.6}$$

The angular bracket indicates the averaging over a canonical ensemble of the initial state A, $\beta = (k_B T)^{-1}$, and $P(W_{AB})$ denotes the nonequilibrium work distribution.

The coupling time can be chosen such that the sampled work distribution $P(W_{AB})$ is close to a Gaussian. By exponentially reweighting a Gaussian distribution (with mean $\langle W \rangle$ and standard deviation σ) one arrives at another Gaussian function which is shifted by a constant $-\beta\sigma^2$. Then, the ECP μ_{ex}^{G} is given by:

$$\mu_{ex}^{G} = \langle W \rangle - \frac{1}{2}\beta\sigma^2 \tag{5.7}$$

We calculated μ_{ex} from the sampled work distribution (eq. 5.6) and from the Gaussian approximation (eq. 5.7). In practice eq. 5.7 provides a good estimate of μ_{ex} when $\beta\sigma \leq 1$.[155]

In experiments one usually reports infinite dilution activity coefficients, rather than excess chemical potentials. The relation between these quantities is given by:

$$\mu_{ex}^{exp} = RT \ln \left[\frac{M_A p_A^{\circ} \Omega_A^{\infty}}{\rho RT} \right] \tag{5.8}$$

M_A is the molecular weight of the additive, p_A° the saturated vapour pressure of the additive at temperature T and Ω_A^{∞} the mass-fraction based solvent activity coefficient at infinite dilution of the solvent at temperature T.[166,167] The activity coefficients Ω_A^{∞} have been reported for PS melts with M_W=53700 g/mol.[167] The experimental mass density ρ of the polystyrene is taken from Ref. [162] (see also Tab. 5.1). We note that eq. 5.8 has a different form if rather than mass-fraction based activity coefficients mole-fraction based coefficients are reported.

The all-atom and united-atom PS systems are obtained by inverse mapping of equilibrated coarse-grained melts. The calculations have been done at a temperature range between 503 K (polymer melt) to 383 K (close to the experimental T_g). For the pure polystyrene matrix we performed simulations of 16 ns. The starting configurations for the FGTI calculations were taken from the last 8 ns in regular intervals. In the AA simulations the overall coupling time of the additive is 2.4 ns. First the Lennard Jones interactions were coupled within 2.2 ns using a soft-core potential (see eq. 5.1). After that the Coulomb interactions were coupled with a coupling time of 0.2 ns. Accordingly, the overall coupling time for the UA simulations is 2.2 ns since the UA model has no Coulombic part. For the FGTI runs we used a Langevin thermostat with a friction coefficient of 1 ps^{-1}, to obtain a canonical distribution when the

additive is nearly decoupled from the PS matrix.

In general the nonequilibrium work distributions are strongly temperature dependent. For lower temperatures, especially for ones close to the experimental T_g, the distributions are very broad. Here the dynamics of the matrix is slowed down so that it is harder to insert a particle which causes that the low-energy tail of the distribution $P(W_{AB})$ is poorly sampled. On the contrary, it is relatively easy to introduce an additive particle in a high-temperature polymer melt. That causes the work distribution to be narrower. By comparing the work distributions obtained with the all-atom and the united-atom models (see Fig. 5.6) one can see that the former distribution is broader than the latter. This is also shown from the data in Tab. 5.4, which contains the corresponding values for the standard deviations σ of the fitted Gaussian distributions. It is apparently easier to couple EB to the UA PS matrix in which segmental relaxations are faster.[151] In Fig. 5.6 the work distribution for the AA model is contrasted with the one for the UA model at 463 K.

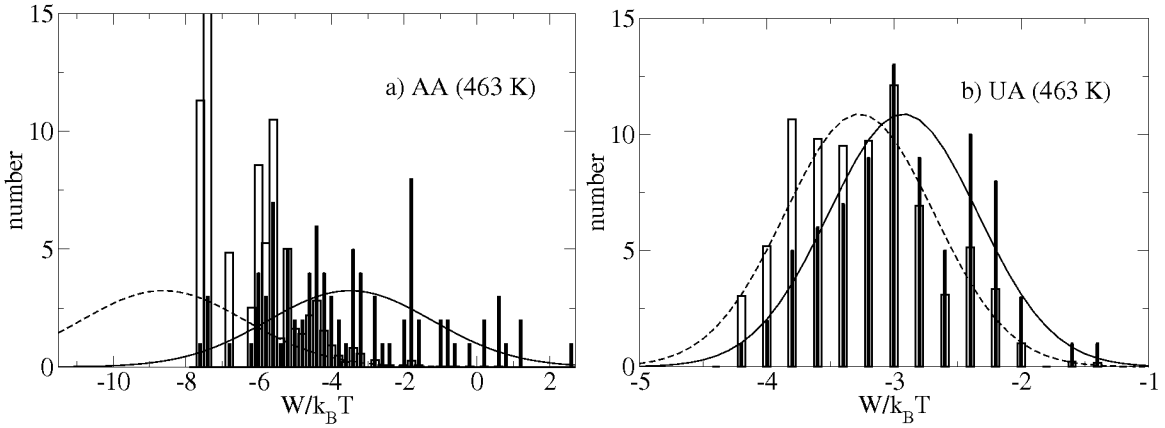

Figure 5.6: Nonequilibrium work distributions for the coupling of a EB molecule at 463 K. In a) the work distribution for the AA model is shown. In b) the UA simulations are shown. The empty bars stand for the exponentially reweighted distribution. The solid line is the Gaussian fit of the sampled distributions. The dashed line is the Gaussian curve but shifted by $-\beta\sigma^2$.

In the all-atom case the sampling is insufficient; i.e. negative values of the coupling work are not sufficiently sampled, hence the low-energy tail of the distribution is not well represented. Furthermore, the distribution is very broad and the value of σ, obtained by fitting a Gaussian function, is bigger than k_BT. Hence, the calculated μ_{ex} contains a systematic error which becomes apparent also when comparing the values of μ_{ex} and μ_{ex}^{G} in Tab. 5.4. As mentioned before, eq. 5.7 provides only a

AA SYSTEMS

T (K)	N	t_{coup} (ns)	$\beta\sigma$	μ_{ex} (kJ/mol)	μ_{ex}^{G} (kJ/mol)	μ_{ex}^{exp} (kJ/mol)	Δ_B (kJ/mol)
423	80	2.4	3.2	-24.3	-34.0	-13.3	0.9
463	80	2.4	2.1	-19.0	-22.3	-11.6	0.8
463	92	4.8	2.3	-20.0	-23.3	-11.6	0.9
503	80	2.4	1.7	-13.5	-15.3		0.7

UA SYSTEMS

T (K)	N	t_{coup} (ns)	$\beta\sigma$	μ_{ex} (kJ/mol)	μ_{ex}^{G} (kJ/mol)	μ_{ex}^{exp} (kJ/mol)	Δ_B (kJ/mol)
383	80	2.2	1.4	-15.2	-15.4		0.6
403	80	2.2	1.0	-13.6	-13.9		0.4
423	80	2.2	0.9	-12.8	-12.8	-13.3	0.4
443	80	2.2	0.8	-12.5	-12.4	-12.5	0.4
463	80	2.2	0.6	-11.9	-11.9	-11.6	0.3
483	80	2.2	0.5	-11.1	-11.0		0.3
503	80	2.2	0.5	-10.1	-10.1		0.2

Table 5.4: Overview of the calculated and experimental ECPs. N denotes the number of performed FGTI runs and t_{coup} the coupling time. ECPs gained from direct sampling μ_{ex} (eq. 5.6), ECPs μ_{ex}^{G} (eq. 5.7) obtained from Gaussian fits with standard deviation σ ($\beta = (k_B T)^{-1}$) and experimental values μ_{ex}^{exp} (eq. 5.8) are shown. Δ_B is the bootstrap error estimate (see the text for details).

good estimate of μ_{ex} when $\beta\sigma \leq 1$. In principle, this can be achieved by finding the optimal balance between the number of performed FGTI runs N and the simulation length t_{coup}. To improve the insufficient sampling in the all-atom simulations we increased the number of FGTI runs as well as the coupling time in order to give the systems more time to accommodate the additive. Unfortunately, these attempts did not lead to any significant improvement. In Tab. 5.4 the values for μ_{ex}, μ_{ex}^{G} and μ_{ex}^{exp} for the different temperatures are shown. The ECPs for the AA model are significantly too low (around two times lower) compared to the experimental values.

On the contrary, the ECPs calculated for the UA systems are in very good agreement with the experimental ones with a discrepancy not bigger than 0.5 kJ/mol over a broad temperature range (see Fig. 5.7). At all temperatures the difference between the ECPs obtained from direct sampling μ_{ex} and the ECPs for a Gaussian distribution μ_{ex}^{exp} is very small. This shows that 80 FGTI runs provide enough sampling. Furthermore we calculated the bootstrap error estimate Δ_B.[155] In this method one assumes that the observed work distribution is close to the correct one. N samples are randomly chosen out of the distribution. By repeating this 100000 times one can calculate the standard error of the resulting free energies. The discrepancy between the calculated ECPs and the ones obtained from experimental data is within bootstrap error Δ_B.

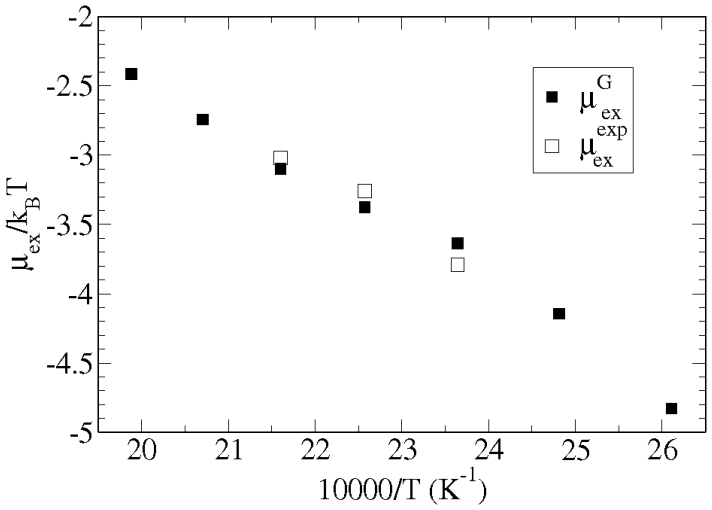

Figure 5.7: Temperature dependence of the calculated ECPs μ_{ex}^{G} obtained with the Wick.2000 force field model (filled symbols) and the experimental ECPs μ_{ex}^{exp} (open symbols).

Based on these calculations we conclude that the AA force field overestimates the strength of the EB-PS thermodynamic interaction causing significantly too low values of μ_{ex}. To provide a clue on the cause of this underestimation we computed the enthalpy of vaporisation of liquid EB with the AA model and compared with the experimental value in order to validate the quality of the EB-EB nonbonded interaction energy. The experimental heat of vaporisation was reproduced with this model (at 383 K) within 2 kJ/mol accuracy. We therefore expect the AA model to also realistically describe the EB interaction with polystyrene which has a similar chemistry. The cause for the underestimation of the EB excess chemical potential in PS must therefore be sought in the excess entropy of EB dissolution which is sensitive to structural correlations in the polymer matrix. Further examination of this issue goes beyond the scope of this work. The UA force field, on the other hand, provides predictions in excellent agreement with the experimental data, which is likely a consequence of the fact that the force field model has been parameterised on vapor-liquid-equilibria and thus on ECPs. In the temperature range where experimental data are available (423-463 K), the UA model slightly underestimates the excess enthalpy, $h_{ex} = (\partial \beta \mu_{ex}/\partial \beta)$, of EB dissolution (which can be obtained from the slope of the data in Fig. 5.7). This observation indicates that the EB-PS nonbonded interactions, as described by the UA model, are too weak. Calculation of the enthalpy of vaporisation of liquid EB with the UA model indeed yields an underestimation of approximately 15 kJ/mol. Here it should be noted that the UA model is an inter-

mediately coarse-grained model and therefore it is not unexpected that the enthalpy and entropy are incorrectly balanced.

5.4 Conclusion

We have proposed a hierarchical simulation approach that provides quantitative predictions of diffusion coefficients and solubilities (excess chemical potentials) of large penetrant molecules in polymer melts. The penetrants are significantly larger than simple gas molecules and have a dimension comparable to that of the polymer repeat unit. Penetrant diffusion coefficients are obtained from MD simulations of a simplified, coarse-grained model. The time mapping procedure, required to compare the simulation time scales to experimental time scales, is studied for the diffusion of ethylbenzene in atactic polystyrene and is shown to obey a Vogel-Fulcher temperature dependency. This observation opens new routes for computationally cheap, coarse-grained molecular dynamics simulations that provide quantitative predictions of penetrant diffusion coefficients at low temperatures and low penetrant concentrations where all-atom simulations fail. In this work we followed the "theoretically clean" route to take densities predicted by the simulated models. Following the same procedure, but using experimental densities, improves the quantitative agreement.

We furthermore applied a nonequilibrium free energy calculation method to predict ethylbenzene excess chemical potentials in molten polystyrene over a wide range of temperatures, using equilibrated all-atom configurations obtained by inverse mapping of the coarse-grained systems. The inverse-mapping method has been performed with an all-atom and a united-atom polystyrene model in order to assess the quality of the atomistic force fields in predicting ethylbenzene excess chemical potentials. The combined coarse-grained and atomistic modelling approach provides full quantitative access to polymer permeation of large penetrant molecules.

6 Thermodynamic transferability of coarse-grained potentials for polymer-additive systems

In this work we study the transferability of systematically coarse-grained (CG) potentials for polymer-additive systems. The CG nonbonded potentials between the polymer (atactic polystyrene) and three different additives (ethylbenzene, methane and neopentane) are derived using the Conditional Reversible Work (CRW) method, recently proposed by Brini et al.[168]. A CRW-based effective pair potential corresponds to the interaction free energy between the two atom groups of an atomistic parent model that represent the coarse-grained interaction sites. Since the CRW coarse-graining procedure does not involve any form of parameterisation, thermodynamic and structural properties of the condensed phase are predictions of the model. We show in this work that CRW-based CG models of polymer-additive systems are capable of predicting the correct structural correlations in the mixture. Furthermore, the excess chemical potentials of the additives obtained with the CRW-based CG models and the united-atom parent models are in satisfactory agreement and the CRW-based CG models show a good temperature transferability. The temperature transferability of the model is discussed by analysing the entropic and enthalpic contributions to the excess chemical potentials. We find that CRW-based CG models provide good predictions of the excess entropies, while discrepancies are observed in the excess enthalpies. Overall, we show that the CRW CG potentials are suitable to model structural and thermodynamic properties of polymer-penetrant systems.

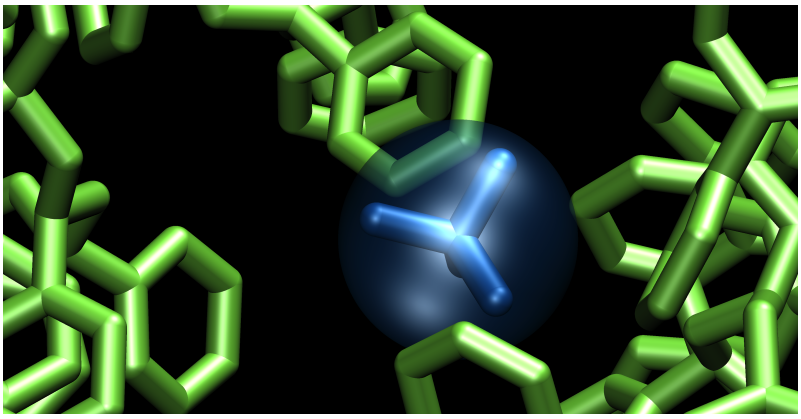

Figure 6.1: Neopentane in a melt of polystyrene.

6.1 Introduction

A detailed microscopic picture is necessary to understand molecular transport processes in polymer-penetrant systems, like liquid and vapour separation membranes, plasticizers in engineering thermoplastics or polymer dissolution processes. Computer simulations have proven to be a useful tool to study the permeation of additives in polymer matrices.[138,169] Atomistic force fields (FFs) are in principle capable of describing these processes accurately, however, often they can not reach the time and length scale needed to simulate, e.g., a polymer swelling or dissolution process. In order to extend time and length scales, coarse-grained (CG) models can be used. To keep a link to the specific chemistry of the system of interest, systematically coarse-grained models are needed, which have been developed in recent years for various macromolecular systems.[148,152,170–176] A CG model is usually obtained by selecting a mapping scheme which merges neighbouring atoms into so-called ”super-atoms” or CG beads and subsequently applying a systematic coarse-graining procedure that provides the corresponding bonded and nonbonded interaction potentials. Reducing the number of particles in the system leads to a reduction of degrees of freedom (DOF), enabling the possibility of studying phenomena happening on time and length scales that atomistic simulations can not capture.

In order to study specific polymer-penetrant systems, the CG potentials should be capable of reproducing both thermodynamic and structural properties of the system. The method used to develop these potentials must therefore cast a certain amount of chemical information into the CG potentials, either through a parameterisation procedure or by other means. The interaction potentials can be parametrised in order to reproduce thermodynamic properties (e.g. partitioning free energy between a polar and an apolar phase[177], liquid-vapour equilibria[178], partition function in the gas-phase[179] or equation of state[180]) or microscopic properties (e.g. liquid structure[181,182] or force distribution[183]). These approaches provide effective pair potentials that are able to reproduce the target property, but nothing can a priori be said about their ability to reproduce other properties or their ability of predicting properties at a state point different from the one used in the parametrisation process. A completely different approach to developing coarse-grained FFs is based on applying the CG mapping scheme at the atomistic level and calculating the effective interaction between the mapped atom groups by a suitable averaging procedure. Examples of quanties that can be used as effective potentials are:

the pair potential of mean force[51,184,185], the effective force[186] and the conditional reversible work (interaction free energy)[168]. This class of methods provides pair potentials that carry-over chemistry-specific information from the detailed atomistic level of description to a coarse-grained mesoscopic level in a systematic manner without resorting to parameterisation. In comparison with potentials obtained by a parameterisation procedure, these methods yield pair potentials which can be more easily related to the distance-dependent interaction between the coarse-grained atom groups. Of course, also with these methods pairwise additivity of the coarse-grained potentials is assumed and nothing can a priori be said about the effectiveness of the potentials to reproduce any property. In this work, the CG nonbonded interaction potentials are developed using the Conditional Reversible Work (CRW) method[168], which was previously shown to model the liquid structure and the density of molecular liquids in good agreement with atomistic simulations. Here, the interaction free energy between the groups of atoms that the beads represent is used as an effective pair potential. An advantage of this method is that effective pair potentials developed in vacuum can be applied in the condensed phase, therefore these potentials are cheap to obtain.[152,168].

The quality of CG models is often discussed in terms of representability and transferability. The representability is the ability of the CG model to predict properties at the state point used for its parametrisation. The transferability is the ability of the model to predict properties at different state points. In our work, the pairwise interactions are developed in vacuum (see section 6.4.1) and are applied in the condensed phase. Therefore, only the transferability of our model will be investigated. In order to understand the quality of the CRW potentials developed in this work, we focus our attention on the prediction of the excess chemical potential (ECP) of small molecules (ethylbenzene (EB), methane (ME) and neopentane (NP)) in a melt of atatic polystyrene (PS)[152]. The choice to study ECPs has several advantages. First of all, this property can be calculated both on an atomistic and CG level (see section 6.2.2), offering the possibility to compare the results obtained using the atomistic model and the derived CG model. This comparison is important since the aim of a systematically developed CG model is to reproduce the results obtained by the parent atomistic model from which it is derived. The second advantage of investigating ECPs is the fact that this property is extremely sensitive to the quality of the pair potentials, therefore providing a good means to investigate the quality of our pair potential. In order to better understand why CG models are transferable we will

study also the entropic and enthalpic contributions to the ECPs (resulting from the reorganisation of the polymer matrix and the binding of the additive to the polymer) such that we can analyse the effect of of coarse-graining on these quantities.

This work is structured as follows: In sections 6.2 and 6.3 we will discuss the methods and the models used in this work. This is followed by a discussion of the computational details in section 6.4. In section 6.5, we will discuss the CG models for the different polymer-additive systems, which have been developed using the CRW method, and study how well these potentials are capable to predict ECPs. Furthermore, we will discuss the temperature transferability of the model and the structural properties of the polymer-additive systems. We will finally summarise the work in section 6.6.

6.2 Methodology

6.2.1 Conditional Reversible Work method

The nonbonded CG potentials used in this work are developed using the CRW method.[168] In the CRW method the interaction free energy between two groups of atoms is used as an effective pairwise CG interaction potential $U_{eff}(r)$. The calculation of the interaction free energy is performed using the thermodynamic cycle presented in Fig. 6.2. This figure shows the computation of the nonbonded interaction potential between a CG bead that represents the phenyl ring of a PS residue, and a CG bead that represents the phenyl ring in the EB molecule. $U_{eff}(r)$ denotes the effective CG pair potential, i.e the interaction free energy between the two groups of atoms when they are at the given distance r under the condition that they are embedded in their respective molecules. This free energy is calculated as the difference between the work of two different reversible processes. The first one ($RW(r)$) is the reversible work needed to bring the two groups of atoms (embedded in their molecule) from infinite distance to the distance r. The second one ($RW_{excl}(r)$) is the reversible work needed to perform the same process but neglecting the direct interaction between the two groups of atoms. The process labelled with $U(\infty)$ in Fig. 6.2 denotes the free energy of the process of switching on the interaction between the two groups of atoms when they are at infinite distance. Since the two groups are not interacting at infinite distance the interaction free energy is zero: $U(\infty) = 0$. According to the thermodynamic cycle, the effective CG pair potential can be calculated as

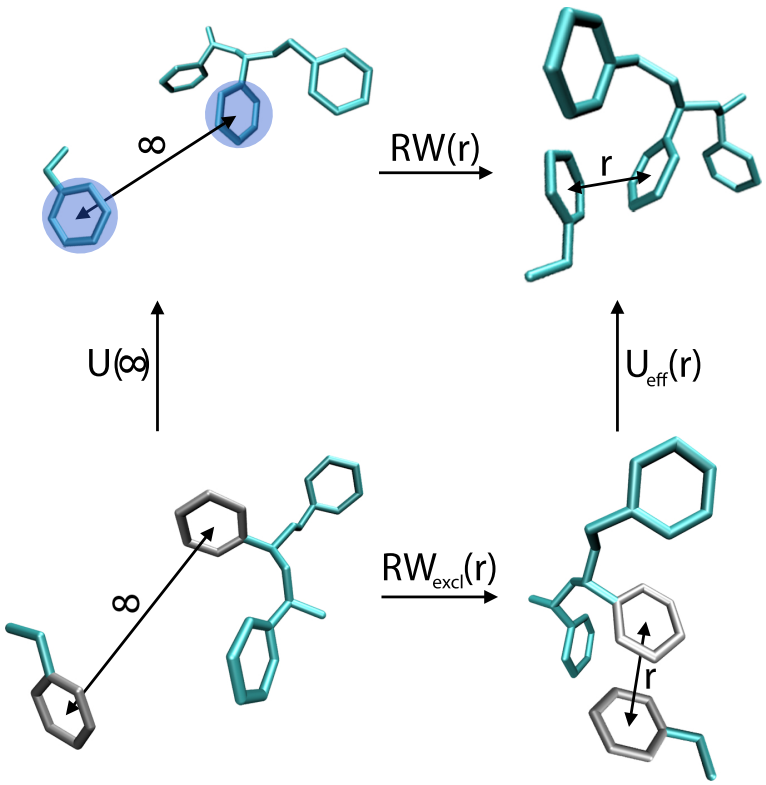

Figure 6.2: Thermodynamic cycle used to calculate the CRW CG potential for the interaction between the phenyl ring of PS and the phenyl ring of EB. The CRW pair potential ($U_{eff}(r)$) is defined as the conditional free energy associated with the process of introducing noncovalent interactions between the atoms in the two rings at a constrained distance r between their centers of mass. Conformational averaging at a selected temperature T is performed over all remaining degrees of freedom. Conditional free energy denotes the fact that conformational averaging is performed with the two atom groups embedded in their immediate chemical environment of the larger molecule. The CRW potential can be calculated as the difference between two reversible work potentials that include ($RW(r)$) and exclude ($RW_{excl}(r)$) the direct noncovalent ring-ring interactions.

$U_{eff}(r) = RW(r) - RW_{excl}(r)$.

Fig. 6.4a) shows the potentials corresponding to $RW(r)$, $RW_{excl}(r)$ and $U_{eff}(r)$ of the thermodynamic cycle for the nonbonded CG interactions between ME and the phenyl ring of PS. $RW(r)$ is the reversible work associated with the process of bringing two molecules together by pulling between the centers of mass of the two groups of atoms. This potential includes indirect contributions due to all the interactions between all the atoms in the two molecules. These indirect interactions are reflected by the irregular shape of the potential. When the same property is calculated excluding the direct interactions between the two group of atoms, we obtain a potential that

contains only indirect interactions ($RW_{excl}(r)$). The difference between these two potentials results in an effective potential $U_{eff}(r)$ between the two group of atoms that does not contain indirect contributions.
The CRW CG potentials used in this work are developed in the gas phase. In order to apply these potentials to polymer-additive systems, they need to be transferable to the condensed phase. Furthermore, the temperature transferability is an important aspect that we will consider in this work. The CRW CG potentials are developed at a certain state point (in this work at 503 K) and it will be shown later, in section 6.5, how transferable they are over a wide temperature range.

6.2.2 Excess chemical potentials

In order to analyse the transferability of the CRW-based CG potentials we studied the excess chemical potentials of three different additives in polystyrene melts. We calculated excess chemical potentials of EB, ME and NP in atactic PS melts on an atomistic and CG level using fast-growth thermodynamic integration (FGTI) [165] for the larger solutes (EB and NP) and test particle insertion (TPI) [187] for ME. Unlike ME, the bulkier NP or EB additives cannot be inserted without severe particle overlaps in the system. In this context, FGTI has proven to be a useful method. [138,155] In FGTI, multiple TI runs are performed, where initially all the interactions between the polymer and the additive are switched off. These interactions are in the course of the simulation slowly turned on with a finite rate and the additive is coupled to the polymer matrix. The nonequilibrium coupling work W_{AB} can be related to the ECP $\Delta\mu_{\mathrm{ex}}$ using Jarzynski's nonequilibrium work theorem. [165]

$$\begin{aligned}\Delta\mu_{\mathrm{ex}} &= -k_B T \log\langle \mathrm{e}^{-\beta W_{\mathrm{AB}}}\rangle_{\mathrm{A}} \\ &= -k_B T \log \int_{\infty}^{-\infty} \mathrm{e}^{-\beta W_{\mathrm{AB}}} P(W_{\mathrm{AB}}) dW_{\mathrm{AB}}\end{aligned} \tag{6.1}$$

The angular brackets indicate an averaging over a canonical ensemble of the initial state A, $\beta = (k_B T)^{-1}$ with k_B the Boltzmann constant and T the temperature, and $P(W_{\mathrm{AB}})$ denotes the nonequilibrium work distribution. Detailed information about this method can be found in the work of Hess et al. [155,156] and Fritz et al. [138]

6.2.3 Thermodynamic analysis

In order to understand how the coarse-graining procedure affects the thermodynamics of the system, different contributions to the ECP are analysed. We consider a system at constant pressure and temperature. Solute insertion (additive sorption) in a polymer melt can be considered as a two-step process. First, (i) a cavity of suitable size and shape for inserting the additive is created inside the polymer, followed by (ii) introducing the binding interactions between the additive and the cavity. The free energy ($\Delta\mu_{\mathrm{ex}}$) of the overall process can be decomposed to obtain an entropic contribution (ΔS_{ex}) and an enthalpic contribution (ΔH_{ex}). These two components can be further subdivided according to the two elementary steps above.[188,189] ΔH_{ex} is then written as

$$\Delta H_{\mathrm{ex}} = \Delta H_{\mathrm{R}} + \Delta H_{\mathrm{B}} \tag{6.2}$$

where ΔH_{R} is the reorganisation enthalpy associated with the loss of cohesive interactions in the cavity formation process, and ΔH_{B} is the binding enthalpy associated with the energy gained in the second step where the additive-polymer binding interactions are introduced. Hence, $\Delta H_{\mathrm{R}} > 0$ and $\Delta H_{\mathrm{B}} < 0$. Similarly, the excess entropy can be split in two contributions[188,189]

$$\Delta S_{\mathrm{ex}} = \frac{\Delta H_{\mathrm{R}}}{T} + \Delta S_{\mathrm{ap}} \tag{6.3}$$

In the literature, ΔS_{ap} has been referred to as the fluctuation entropy[190] or the solute-solvent entropy[191] because it can be related (through statistical mechanics formulas) to fluctuations of the solute-solvent interaction energy. Here, we use the subscript 'ap' where 'a' denotes the additive and 'p' the polymer melt. In Van der Waals systems, the major contribution to ΔS_{ap} arises from excluded volume interactions. ΔS_{ap} is the entropic cost of solute insertion; it is always negative and quantifies the loss of entropy associated with the reduced phase space that the polymer is able to sample due to the presence of an additive. Formally, $\exp[\Delta S_{\mathrm{ap}}/k_B]$ can be interpreted as the probability to observe an empty, transient cavity in the polymer melt. This cavity has the polymer repeat units in the equilibrium positions and orientations appropriate for accommodating all chemical moieties of the additive molecule. The contribution $\Delta H_{\mathrm{R}}/T$ to the excess entropy accounts for changes in all other in-

teractions (the polymer-polymer interactions) not involving the solute. At constant pressure, $\Delta H_R/T$ is positive[188] and partly compensates the negative contribution from ΔS_{ap}.

The excess enthalpy ΔH_{ex} and excess entropy ΔS_{ex} are temperature derivatives of the free energy, i.e. $\Delta S_{ex} = -\left(\partial \Delta\mu_{ex}/\partial T\right)_p$ and $\Delta H_{ex} = \left(\partial \beta \Delta\mu_{ex}/\partial \beta\right)_p$, and can therefore be obtained from the temperature dependence of $\Delta\mu_{ex}$ at constant pressure. ΔH_B is the sum of the nonbonded interaction energies between the polymeric matrix and the additive and is obtained directly from the simulations. ΔH_R and ΔS_{ap} can then be calculated by applying eq. 6.2 and eq. 6.3.

The CG model is temperature transferable if the predicted temperature dependence of $\Delta\mu_{ex}$ agrees with the prediction obtained with the parent atomistic model, i.e. a transferable model reproduces the excess entropy (ΔS_{ex}). We point out that there is no a priori reason to expect that the CG model reproduces ΔH_{ex} and ΔS_{ex} in agreement with the UA model. CRW pair potentials are not energies but free energies. This means that a part of the entropy associated with a pairwise molecular interaction in the UA model description is contained in the effective pair potential of the CG model. This 'interaction entropy' is unfavorable (interactions bias the sampling of available phase space) and compensates part of the energetic attractions between two chemical groups, leading to effective pair potentials with shallow minima in comparison to the parent UA model. Therefore, the interactions in the CG model are effectively weaker (i.e. potential energy minima are less deep) than those in the UA model, while the entropy in the CG model is effectively larger. These implicit entropy contributions in the effective CG pair potentials may however cancel in the thermodynamic quantities ΔH_{ex} and ΔS_{ex} since they appear in the terms on the right hand sides of eq. 6.2 and 6.3 with opposite sign.

6.3 Models

6.3.1 United-atom model

All united-atom (UA) MD simulations for calculating of thermodynamic and structural properties were performed using the TraPPe UA FF[158]. This FF is targeted to reproduce vapour-liquid equilibria of molecular liquids. The development of the CG potentials has been done using the TraPPe FF, which has been applied successfully to polymer-additive systems in previous work[138] and it has been shown that it predicts values for the ECPs over a wide range of temperatures close to the experimental

values. The CG polystyrene model of Fritz et al.[152] is based on the all-atom model of Müller-Plathe et al.[135] All the equilibrated atomistic starting configurations of the PS melt of the 24 chains of atactic 96mers are obtained by inverse mapping of equilibrated CG melts at different temperatures. Details can be found in the work of Fritz et al.[138]

6.3.2 Coarse-grained model

We have used the CRW method developed by Brini et al.[168] to develop polymer-additive CG potentials. The mapping scheme is of crucial importance since different mapping schemes can lead to different results with respect to the transferability and representability of the CG model. The EB CG model, developed in this work, is composed of two beads: the first one represents the ethyl substituent (A_{EB}) an the second one represents the phenyl ring (B_{EB}) (see Fig. 6.3). The CG mapping points of these two beads are chosen as the center of mass of the group of atoms that they represent. NP and ME are represented as a single CG site, with the mapping point in its center of mass. The size of the atomistic and the CG methane is directly comparable, since we used a united-atom force field for the atomistic description. The coarse-grained PS model was previously developed following a CRW approach by Fritz et al.[152] The PS unit is represented by a two-bead model, one describes the phenyl ring and the other one represents the backbone. The model is capable of simulating polymer chains with different tacticity and is able to reproduce different structural and thermodynamic properties, for further informations we refer to the original paper of Fritz and et al.[152]

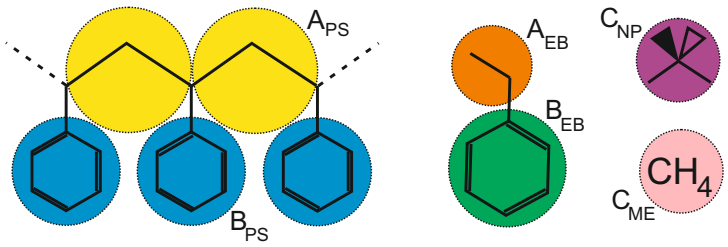

Figure 6.3: Mapping scheme for PS[152] and EB. NP and ME are both represented as a single bead in the CG representation.

Besides the nonbonded interactions, the bonded potentials are another crucial aspect of the CG model. ME and NP are mapped as single beads, therefore there is no bonded interaction needed. The CG EB is represented by two beads (A_{EB} and B_{EB}),

this molecule is modelled as a rigid dumbbell, with the interatomic distance fixed at the equilibrium distance. For a description of the bonded interaction in the PS model, we refer the reader to the original work by Fritz and et al. [152]

6.4 Computational details

All simulations performed in this work were done using the GROMACS simulation package. [98]

6.4.1 CRW

Non-bonded CRW potentials are developed in vacuum through a series of distance constraint simulations between the centers of mass of the groups of atoms for which we want to calculate the CG interaction potential. The constraint algorithm employed is the linear constrain solver (LINCS). [144] The average constraint force is obtained from a 800 ns simulation trajectory generated employing a time step of 2 fs. The reversible work is then calculated integrating the average constraint force of every simulation over the constrain distance. [152] This distance is varied between 1.1 nm and 0.32 nm in steps of 0.02 nm. The constraint dynamics simulations are all performed at 503 K using a stochastic dynamics integrator with an inverse friction coefficient 0.5 ps. The cut-off distance for Lennard Jones interactions is 4.0 nm, this ensures that even at the largest sampling distance all the atoms of the two molecules are interacting. Since the sampling is carried out using a united atom force field no charges are involved.

As a CG mapping point for the additive the center of mass of the atoms that the CG beads represent is used. For the B_{PS} bead the center of mass of the central ring of a PS trimer is used. The interaction potentials of the additive with the A_{PS} bead is less straight forward to calculate. As it can be seen in Fig. 6.3 this CG bead represent a CH group and two $1/2$ CH groups. The interaction free energy for half atoms cannot be calculated. Therefore, we choose to define $RW_{excl}(r)$ as the potential that results from the arithmetic average between a $RW_{excl}(r)$ calculated in a process where only the direct interaction of the additive with the central CH is excluded and another $RW_{excl}(r)$ that characterises a process where all the interaction between the additive and the atom of A_{PS} are excluded. We note that this can cause uncertainties in the

enthalpic interactions. To obtain the second series of interaction potentials for the NP-PS interaction, a pentamer of PS has been employed instead of a trimer.

6.4.2 Excess chemical potentials

All simulations are performed under NpT conditions at a pressure of 1 atm. It has been shown that under these condition the Fritz PS CG model is able to reproduce the thermal expansion coefficient, although the densities of the CG and UA model are slightly different[138,152]. The atomistic PS systems used in this work for the calculation of ECPs are obtained by inverse mapping of equilibrated coarse-grained melts. The calculations have been done in a temperature range between 503 K (polymer melt) and 383 K (close to the experimental T_g of 373 K). The T_g of the CG PS model is 363 K.[192] For the pure polystyrene matrix we performed simulations of 16 ns at each temperature. The starting configurations for the FGTI calculations were taken from the last 8 ns. The ECPs of NP and EB in the atomistic and CG systems are calculated by performing 50 independent FGTI calculations. The overall coupling time of the additive is 2 ns, in which the Lennard Jones interactions are switched on. For the FGTI runs we used a Langevin thermostat with a friction coefficient of 1 ps^{-1}, to obtain a canonical distribution when the additive is nearly decoupled from the PS matrix. The ECPs of ME in PS of the atomistic and CG systems were calculated using TPI. 3000000 insertions are performed every 10000 timesteps in an overall 20 ns PS trajectory, obtained at different temperatures using a Berendsen[159] thermostat with a coupling time of 1ps.

6.4.3 MD simulation

We have performed MD simulations at 503 K in order to calculate radial distribution functions (RDFs) for the three different polymer-additive systems. The systems contain a melt of 24 chains (96mers) of atactic PS and 10 additive molecules. The simulations are performed under isothermal-isobaric conditions using a Parrinello-Rahman barostat[140,141] with a coupling time of 1 ps and a Nose-Hoover thermostat[142,143] with a coupling time of 0.1 ps. The bonds are constrained using the LINCS algorithm.[144]. The UA simulations are 60 ns long using an integration time of 2 fs. The CG simulations are 40 ns long using the same integration time step.

6.5 Results and discussion

We studied the transferability of CRW CG potentials for different polymer-additive systems. To this end, structural and thermodynamic properties are calculated for the following three systems: ethylbenzene, methane and neopentane in polystyrene. In this work, we have studied the ECPs of the additives in a melt of 24 chains of atactic 96mers of PS. Firstly, we will present the CRW CG potentials developed in this work, then we discuss the temperature dependence of the ECPs for the three different systems to then, in a later section, discuss the structure of the system and analyse the different enthalpic and entropic contributions to the ECPs.

6.5.1 CG potentials

Using the CRW method we obtained CG nonbonded interaction potentials between the additives and the polymer. These potentials are reported in Fig. 6.4 in panel b), c) and d). All the potentials have a monotonically varying tail, which is a clear indication that the potentials are not containing any multi-body contributions[168]. Also the relative magnitudes of the interaction potentials between the additives and A_{PS} and B_{PS} are reasonable. In fact, all the interaction potentials in which B_{PS} is involved are deeper and show a bigger excluded volume compared to the one where A_{PS} is involved.

Fig. 6.4c) shows the interaction between EB and PS. The interaction $B_{EB} - B_{PS}$ is the deepest of the four; this reflects the bigger size and the stronger interaction that phenyl rings have compared to few atoms of the backbone. It is also interesting to note that the potential $A_{EB} - B_{PS}$ and $B_{EB} - A_{PS}$ (dashed lines) are to some extent similar, since they both represent the interaction between alkyl chains with a phenyl ring.

Fig. 6.4b) shows two sets of potentials for the interaction between ME and PS. The difference between these two sets is the distance at which the interaction between the beads is considered negligible, for the first set (continuous lines) this distance is 1.1 nm and for the second set (dashed lines) it is 1.0 nm. The difference between the two sets is minimal but its effect on the ECP is not negligible, as we will see later in section 6.5.2). This gives us an idea of how small variations in the potential (due to any possible cause, even statistical errors) can influence the computed ECPs.

In Fig. 6.4d) the interaction potentials between NP and PS are reported. These

are shifted to bigger distance and are deeper compared to the interaction potential between ME and PS, reflecting the bigger size of NP molecule. In order to pinpoint eventual sampling issues during the CRW procedure in vacuum, two sets of potentials have been calculated. The first set (continuous line) refers to a model parametrised using a 3mer of PS, the second set (dashed line) refers to a model parametrised using a 5mer of PS. The interaction potentials are similar, but the potentials obtained with the 5mer are smoother.

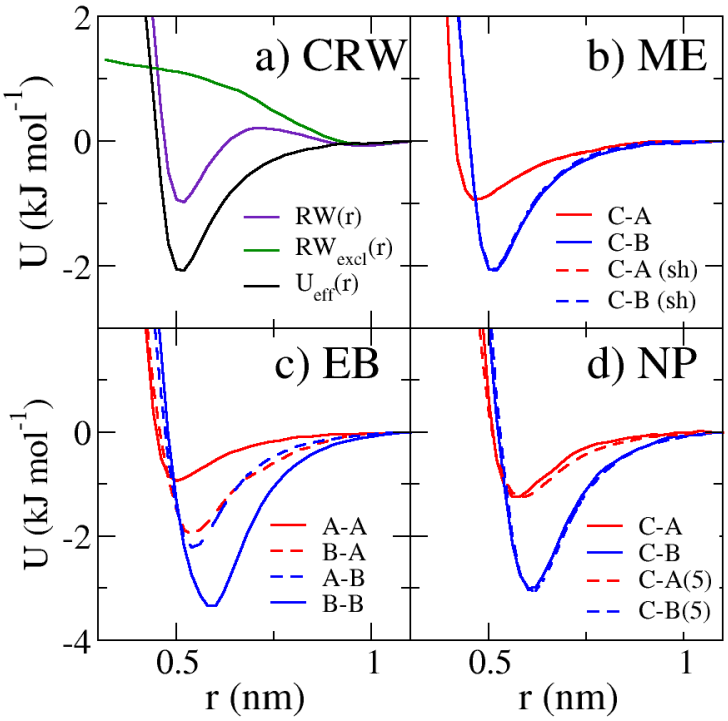

Figure 6.4: Non-bonded interaction potentials developed in this work. Panel a) describes how the CRW method works taking as example the interaction $C_{ME} - B_{PS}$. Panels b), c) and d) show the interaction potentials between PS and ME, EB and NP, respectively. In the legends of these three panels the first letter denotes the additive bead and the second letter denotes the PS bead to which the interaction is referred; also all the interactions with A_{PS} are coloured in red and with B_{PS} are coloured in blue. In b) and d) dashed lines refers to a second set of potentials developed respectively considering a cutoff of 1.0nm and using during the development of interaction potential a pentamer of PS instead of a trimer.

6.5.2 ECPs of additives in polystyrene melts

Fig. 6.5 shows the ECPs for the three different polymer-additive systems. The black dots show the UA ECPs and the red triangles are the results from the CG simulations. The dashed lines show the temperature dependence of the ECPs. The slopes of these linear fits provide the excess entropies. As shown in previous work, the UA force field for EB is capable of predicting ECPs close to the experimental values.[138] Quantitative differences are observed between the ECPs obtained with the CG and

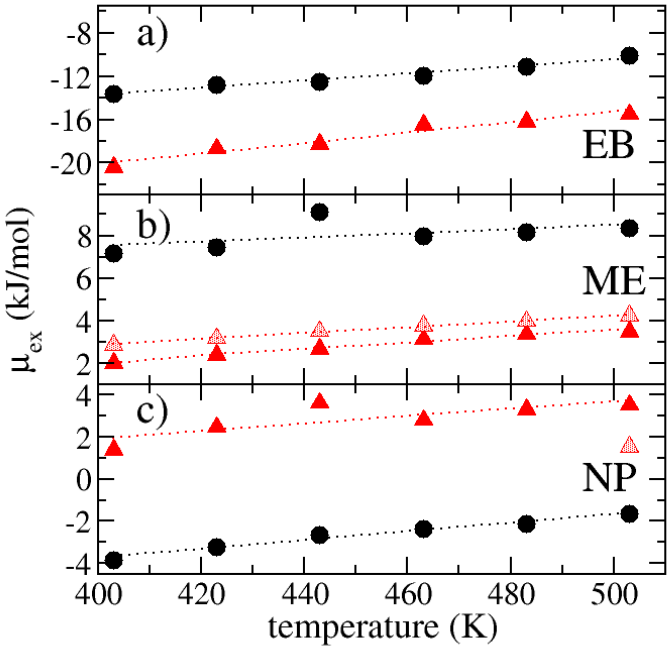

Figure 6.5: Temperature dependence of the excess chemical potentials of EB, ME and NP in a PS melt. The black dots show the UA simulation results, the red triangles the CG simulation results. Linear regressions are shown as dashed lines. The red patterned triangles in panel b) show results obtained with the potentials C-A(sh) and C-B(sh) in Fig. 6.4b). The red patterned triangle in panel c) shows the result obtained with the potentials C-A(5) and C-B(5) in Fig. 6.4d).

reference atomistic models. The differences will be discussed below. Interestingly, the temperature dependence of the ECPs is the same for the CG and UA models, indicating that the CG model is temperature transferable and the excess entropies of these additive are correctly represented by the CG model. Fig. 6.5a) shows that the CG simulations predict too low values for the ECPs of EB in PS. This also happens in the case of ME (shown in Fig. 6.5b)). The ECPs of ME are positive, indicating

low solubility of ME at these temperatures. Contrary to what is observed in a) and b), Fig. 6.5c) shows that the UA simulations predict negative values for the ECPs of NP and larger, positive values at the CG level. We will discuss this inverse trend in section 6.5.4, where we discuss in greater detail enthalpic and entropic contributions to the ECPs.

Shen et al. have shown before that small changes in the CG potentials can lead to big changes in the thermodynamic properties.[51] We address this issue by varying the CG potentials used in this work and study the effect on the ECPs. As described in section 6.5.1, we have derived two CG potentials for the interaction between PS and ME using two different cutoffs. Fig. 6.5b) shows the results for the ECPs derived with a cutoff of 1.1 nm (red filled triangles) and with a cutoff of 1.0 nm (red patterned triangles). The potentials are reported in Fig. 6.4b). The difference between the potentials is almost not visible. However, small changes in the CG potentials can lead to relatively large differences in the ECPs. The differences in the potentials are of the order of magnitude of the errors that occurs when deriving the potentials. The ECPs for the CG potential with a cutoff of 1.0 nm are shifted around 1 kJ/mol in comparison to the one calculated using the CG potential with a cutoff of 1.1 nm. In principle, this opens a route to tailor the CG potentials such that they are in perfect agreement with the UA values. Since already small changes in the potentials are enough to achieve this, it will not have any significant effect on the structural properties. As previously mentioned in section 6.5.1, we have also developed a second set of potentials for the interaction of NP with PS. This second set is derived using a 5mer of PS for the vacuum sampling instead of a trimer. In general, the vacuum sampling of the polymer strand of a given length is only an approximation to describe the interaction with the polymer. The isolated PS strand is normally embedded in a polymer chain and could therefore sample slightly different conformations than when being part of the longer polymer chain. This might lead to structural or thermodynamic discrepancies between the UA reference system and the CG model. Fig. 6.4d) shows the different CG potentials. The CG potentials that are based on the 5mer sampling show only a small shift to larger distances. The corresponding ECP shown in Fig. 6.5c) (red patterned triangle) however differs significantly from the value obtained with the 3mer potential. The ECP using the CG potential obtained with the 5mer sampling is about 2 kJ/mol lower and therefore closer to the UA reference. This shows that on the one hand the ECP is very sensitive to small changes in the interaction potential. On the other hand, it indicates that the way the CG potentials are derived can strongly influ-

ence the transferability and representability of the model. Under these conditions, it is even more striking that such simplified CG models can predict sensitive thermodynamic quantities, like the ECPs, in the right order of magnitude and with the correct temperature dependence.

6.5.3 Structure

In order to compare the ECPs of the UA and CG system it is mandatory that the local chemical environments of the additives in the UA and CG polymer matrix are similiar. For this reason we calculated RDFs for the three different systems at the UA and CG level at 503 K. Fig. 6.6 and 6.7 show the radial distribution functions of EB with PS, and ME and NP with PS, respectively. The UA and CG RDFs are in a good agreement, considering that this property is a prediction of the CG model that we remind is not parametrized to reproduce any properties. However, the CG RDFs are slightly shifted to smaller distances. This is probably due to the spherical representation of slighly anisotropic groups. Because the ring structure of the phenyl group of PS is modeled as a sphere, the interaction potentials between B_{PS} and the additives represent averages of additive-ring face and additive-ring side interactions. This causes the effective excluded volume of the beads to be an average between these two limiting configurations, and this can lead to a small shifting in the calculated RDF. We note that the shifting in the RDFs involving B_{EB} in Fig. 6.6 b) and d) is more pronounced compared to the shifting of the other bead pairs reported in the same figure and in Fig. 6.7.

The comparison of the UA RDFs and CG RDFs indicate that the chemical environment of the additives is similar in both systems. Therefore, the UA and CG ECPs can be meaningfully compared and deviations can be related to details of the CRW potentials.

6.5.4 Entropy and enthalpy contributions to ECPs

In order to analyse discrepancies in the ECPs in greater detail, we studied the excess enthalpies and excess entropies and their thermodynamic contributions to the UA and the CG systems, as described in section 6.2.3. All data are reported in Tab. 6.1, where the arrows illustrate the direction of the trend between UA and CG quantities. All values are reported at the temperature of 503 K in units of kJ/mol. Firstly, we discuss the excess enthalpy (ΔH_{ex}) and the excess entropy (ΔS_{ex}) of the

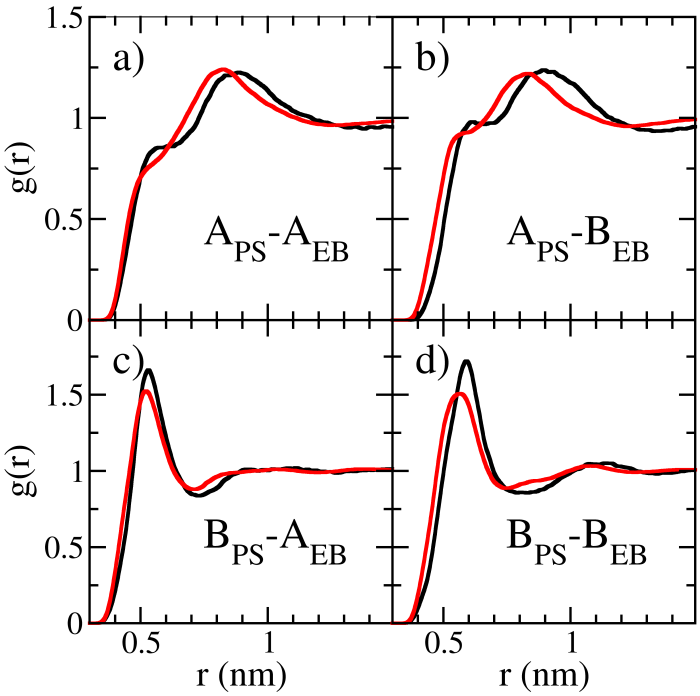

Figure 6.6: Radial distribution functions of the PS CG beads A_{PS} and B_{PS} with the EB CG beads A_{EB} and B_{EB}. The black lines are obtained from the UA simulations and the red lines form the CG simulations using the CRW-derived CG potentials.

three different systems and after that we analyse the different contributions to them. Fig. 6.5 and the data in Tab. 6.1 show that a reasonable agreement is achieved in the temperature dependence of the ECPs with an approximately constant offset between the UA and CG data. Hence, the excess entropies ΔS_{ex} of the additives are reproduced with the CG model while the mismatch between the UA and CG ECPs is of enthalpic origin (ΔH_{ex}). The three different additives show different trends (indicated by the arrows in Tab. 6.1). In the case of NP, the CG model predicts systematically too high ECPs (where in the case of EB and ME the ECPs are too low). A comparison of the UA and CG predictions of ΔH_{ex} and $-T\Delta S_{\text{ex}}$ in Tab. 6.1 shows that the largest, absolute discrepancies are obtained with EB. In order to better understand these discrepancies we have decomposed ΔH_{ex} and $-T\Delta S_{\text{ex}}$ according to the scheme discussed in section 6.2.3. If we compare the relative changes in binding enthalpies among ME, NP and EB (the order of increased binding interaction) at both the UA and CG level, we find that the CG model is consistent with the UA model. For example, the ΔH_{B} associated with the insertion of a EB molecule in the polymeric matrix is about 4 times the ΔH_{B} associated with the insertion of a ME

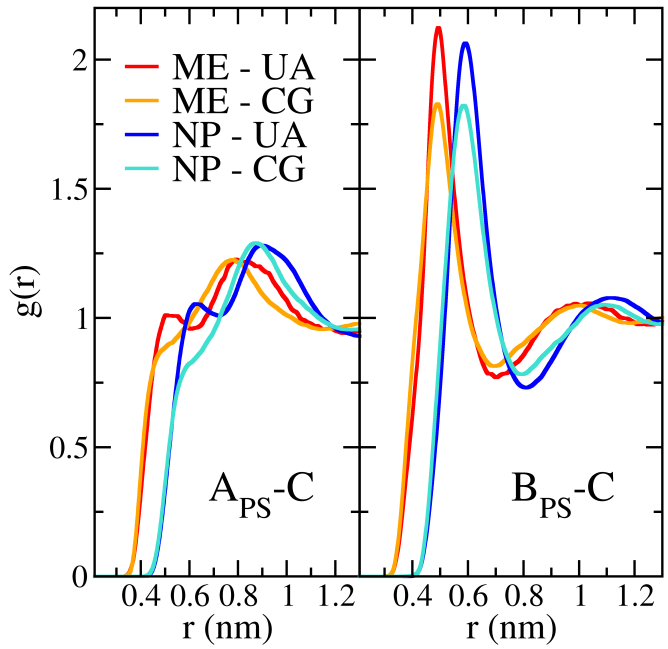

Figure 6.7: Radial distribution functions of the PS CG beads A_{PS} and B_{PS} with the coarse-grained ME, beadtype C_{ME}, and with the coarse-grained NP, bead type C_{NP}. The red and blue lines are obtained from the UA simulations and the orange and turquoise lines form the CG simulations using the CRW derived CG potentials.

molecule, both in the UA and in the CG simulations. This observation is very interesting since it indeed indicates that the newly developed CRW potentials provide a chemically realistic description of changes in ΔH_{B} upon varying chemical groups in condensed phase systems. A similar comparison made for the relative changes in reorganization enthalpies among ME, NP and EB (the order of increasing reorganization enthalpy as predicted by the UA model) however clearly points out that ΔH_{R} obtained for EB with the CG model is unrealistically small. As a result, ΔH_{ex} of EB, predicted by the CG model, is underestimated (too negative) in comparison with the UA model. This observation is consistent with the structural analysis in section 6.5.3 which indicated that the spherical description of the phenyl bead yields a CRW potential with too small excluded volume repulsion. The excess entropy contains two contributions (eq. 6.3), which, at constant pressure, have opposite sign. If ΔH_{R} is predicted too small, we expect that ΔS_{ap} is also predicted too small; i.e. if the enthalpy cost of cavity formation (ΔH_{R}) becomes smaller, the probability increases that thermal fluctuations lead to the formation of transient cavities. This can be observed

in the last column of Tab. 6.1 where, in comparison to the data of the UA model, $-T\Delta S_{ap}$ of EB(CG) is not significantly bigger than that of NP(CG). This leads to an underprediction of the excess entropy for EB.

We finally note that in the CG system ΔH_R, ΔH_B and ΔS_{ap} are strongly dependent on the mapping scheme and therefore on the number of degrees of freedom that are lost in the CG procedure. It therefore is difficult to quantitatively compare these quantities for the three different additives, which all map a different number of atoms in an effective CG interaction site. Although the contributions of ΔH_R, ΔH_B and ΔS_{ap} to the excess entropies and enthalpies add up to reasonably accurate predictions in some cases (e.g. the excess entropy of ME and NP), it remains unclear why the excess enthalpy of NP is overpredicted, while being underpredicted for ME and EB. To address these questions, a systematic study of a single system with different CG mapping schemes is required where enthalpy-entropy compensation of implicit entropy contributions in the effective interaction potentials is studied in greater detail (see discussion of eq. 6.2 and 6.3 in section 6.2.3).

	$\Delta\mu_{ex}$	ΔH_{ex}	$-T\Delta S_{ex}$	ΔH_R	ΔH_B	$-T\Delta S_{ap}$
EB (UA)	-10.1	-26.8	16.6	35.5	-62.3	52.2
EB (CG)	-15.5 ↑	-40.0 ↑	24.7 ↓	10.2 ↑	-50.2 ↓	34.7 ↑
ME (UA)	8.3	3.0	5.0	18.3	-15.3	23.6
ME (CG)	3.5 ↑	-4.2 ↑	7.7 ↓	8.3 ↑	-12.5 ↓	16.0 ↑
NP (UA)	-1.6	-12.2	10.6	30.7	-42.9	41.3
NP (CG)	3.5 ↓	-5.8 ↓	9.1 ↑	21.1 ↑	-26.9 ↓	30.4 ↑

Table 6.1: Excess chemical potentials ($\Delta\mu_{ex}$), excess entropies (ΔS_{ex}), excess enthalpies (ΔH_{ex}), reorganisation enthalpy (ΔH_R), binding enthalpy (ΔH_B) and the solute-solvent entropy (ΔS_{ap}) for three systems studied in this work: EB, ME and NP in PS. We report the values for the UA and the CG system at 503 K. The arrows illustrate the direction of the trends between the CG and UA quantities. All units are in kJ/mol.

6.6 Conclusions

We have studied the thermodynamic transferability of CRW derived CG potentials for three different polymer-additive systems. We have shown in this work that these CG potentials are capable of predicting the correct structural correlations in the mixture. Furthermore, the ECPs of the additives obtained with the UA and the CG models are in acceptable agreement, given that this quantity is very sensitive to small changes in the potentials. It is striking that the CRW-based CG models show

a good temperature transferability. This means that the excess entropies are well reproduced, while discrepancies are observed in the excess enthalpies.

Although we already achieve a relatively good agreement with the UA reference system, one can try to improve the models even further. Theoretically, CRW-based CG models can be tailored such that thermodynamic quantities, like the ECPs, are in excellent agreement with the atomistic reference system. We have shown that a small shift in potential can cause a relatively big shift in the ECPs. Since this shift is very small, structural properties will not be affected. This opens up a way to simulate chemistry-specific polymer-solvent systems with coarse-grained models on large length and time scales, examples of which include plasticizers in polymer networks, polymer swelling and dissolution in specific solvents, polymer wetting processes, etc.

7 Outlook

A realistic polymer coating system can be described using comprehensive multiscale modelling simulations, which involve a systematic bottom-up approach encompassing the bridging of quantum, atomistic and mesoscale levels of resolution. This represents a computationally complex task and this thesis has presented approaches that can help to achieve it. The biggest challenge in this context is the quantum-classical modelling of surface interactions. An optimised and automated fitting routine has been presented that allows for the parameterisation of complex interfacial interactions. Furthermore, methods to obtain representable and reliable force fields have been demonstrated, an aspect that has only been poorly addressed in the current literature. Preliminary results for a polyurethane coating system on ZnO(0001) have been presented and it has been shown that recent coarse-grained techniques can access polymer permeation processes. This is especially important since the water permeation in such polymer coatings can influence the coating's properties quite strongly.

Although these techniques provide an important contribution towards the multiscale modelling of polymer coatings, some open questions remain. Besides the development of a coarse-grained model for the bulk polyurethane, the coarse-grained modelling of surface interactions, in particular, is one of the major challenges. Only a few studies that model surface interactions on a coarse-grained level can be found in the literature but none of these models consider the transfer of information from the quantum to the atomistic level.[171,193–196] To the best of our knowledge, the only coarse-grained model that is based on quantum chemical information is the polycarbonate-on-Ni(111) model of Abrams, Delle Site et al.[4,21] Johnston et al. have subsequently refined this model to study the structure, dynamics and impurity diffusion in this system.[16] This model presents a first promising step towards the simulations of realistic systems. However, it misses out an intermediate atomistic stage and parameterises the coarse-grained surface interactions with adsorption energies calculated at the quantum level. As shown in chapter 6, the interactions between coarse-grained beads are normally softer (i.e., the interaction potentials are shallower) than in the atomistic system. An interaction between two coarse-grained

beads with an interaction strength of the order of the quantum adsorption energies, which can be up to 1 eV or even more depending on the system, might lead to a mismatch in the sensitive interplay of the entropic and enthalpic contributions at the interface. Structure-based coarse-graining techniques, such as Iterative Boltzmann Inversion,[197] have successfully been applied to model surface interactions on a coarse-grained level.[171,196] However, this approach relies on well equilibrated atomistic systems that, ideally, have explored the full conformational phase space. On an atomistic level, this is a non-trivial problem since the barriers between different near-surface conformations are often on the order of tens of k_BT and therefore cannot be overcome by thermal activation. Furthermore, in the coarse-grained modelling of polymer coating systems, it is important that thermodynamic properties, such as the excess chemical potential of a penetrant in the polymer, are captured correctly. This is not a priori clear in structure-based coarse-grained models. Chapter 6 demonstrated that the application of the Conditional Reversible Work method of Brini et al.[168] can provide thermodynamically transferable models. However, at present, this method has not been used to model surface interactions. The next step, then, is to test the application of the CRW method and apply it to the polyurethane-ZnO system. This would provide the missing step towards a comprehensive multiscale model of a polyurethane coating system that encompasses the bridging of three scales of resolution. Subsequent studies employing such a model could have a strong impact on the design and improvement of the properties of coatings and provide an understanding of the mechanisms that take place on larger length and time scales, such as delamination effects.

Bibliography

[1] M. I. McCarthy, G. K. Schenter, C. A. Scamehorn, and J. B. Nicholas. *J. Phys. Chem.*, 100:16989–16995, 1996.

[2] A. V. Bandura and J. D. Kubicki. *J. Phys. Chem. B*, 107:11072–11081, 2003.

[3] O. Borodin, G. D. Smith, R. Bandyopadhyaya, and O. Byutner. *Macromolecules*, 36:7873–7883, 2003.

[4] L. Delle Site, C. F. Abrams, A. Alavi, and K. Kremer. *Phys. Rev. Lett.*, 89:156103, 2002.

[5] P. Schravendijk, N. F. A. van der Vegt, L. Delle Site, and K. Kremer. *Chem. Phys. Chem.*, 6:1866–1871, 2005.

[6] V. Carravetta and S. Monti. *J. Phys. Chem. B*, 110:6160–6169, 2006.

[7] M. L. Sushko, A. Y. Gal, and A. L. Shluger. *J. Phys. Chem. B*, 110:4853–4862, 2006.

[8] D. J. Cole, M. C. Payne, G. Csanyi, S. M. Spearing, and L. Colombi Ciacchi. *J. Chem. Phys.*, 127:204704, 2007.

[9] P. Schravendijk, L. M. Ghiringhelli, L. Delle Site, and N. F. A. van der Vegt. *J. Phys. Chem. C*, 111:2631–2642, 2007.

[10] J. S. Smith, O. Borodin, G. D. Smith, and E. M. Kober. *J. Polym. Sci. Part B Polym. Phys.*, 45:1599–1615, 2007.

[11] K. B. Tarmyshov and F. Müller-Plathe. *J. Chem. Phys.*, 126:074702, 2007.

[12] F. Iori, R. Di Felice, E. Molinari, and S. Corni. *J. Comput. Chem.*, 30:1465–1476, 2008.

[13] L. M. Ghiringhelli, B. Hess, N. F. A. van der Vegt, and L. Delle Site. *J. Am. Chem. Soc.*, 130:13460–13464, 2008.

[14] T. G. A. Youngs, D. Weber, L. F. Gladden, and C. Hardacre. *J. Phys. Chem. C*, 113:21342–21352, 2009.

[15] J. Schneider and L. Colombi Ciacchi. *J. Chem. Theory Comput.*, 7:473–484, 2011.

[16] K. Johnston and V. Harmandaris. *J. Phys. Chem. C*, 115:14707, 2011.

[17] C. R. Herbers, K. Johnston, and N. F. A. van der Vegt. *Phys. Chem. Chem. Phys.*, 13:10577–10583, 2011.

[18] K. Johnston, C. R. Herbers, and N. F. A. van der Vegt. submitted, 2012.

[19] K. Johnston and V. A. Harmandaris. *Phys. Chem. Chem. Phys.*, submitted, 2012.

[20] A. Butenuth, G. Moras, J. Schneider, M. Koleini, S. Köppen, R. Meissner, L. B. Wright, T. R. Walsh, and L. Colombi Ciacchi. *Phys. Status Solidi B*, 2:292–305, 2012.

[21] C. F. Abrams, L. Delle Site, and K. Kremer. *Phys. Rev. E*, 67:021807, 2003.

[22] L. Delle Site, S. Leon, and K. Kremer. *J. Am. Chem. Soc.*, 126:2944–2955, 2004.

[23] K. Nakanishi, T. Sakiyama, and K. Imamura. *J. Biosci. Bioeng.*, 91:233–244, 2001.

[24] J. H. Harding and D. M. Duffy. *J. Mater. Chem.*, 16:1105–1112, 2006.

[25] R. A. Latour. *Biointerphases*, 3:FC2–FC12, 2008.

[26] J. H. Harding, D. M. Duffy, M. L. Sushko, P. M. Rodger, D. Quigley, and J. A. Elliot. *Chem. Rev.*, 108:4823–4854, 2008.

[27] O. Cohavi, S. Corni, F. De Rienzo, R. Di Felice, K. E. Gottschalk, M. Hoefling, D. Kokh, E. Molinari, G. Schreiber, A. Vaskevich, and R. C. Wade. *J. Mol. Recognit.*, 23:259–262, 2010.

[28] R. Di Felice and S. Corni. *J. Phys. Chem. Lett.*, 2:1510–1519, 2011.

[29] J. Hermans, H. J. C. Berendsen, W. F. van Gunsteren, and J. P. M. Postma. *Biopolymers*, 23:1513, 1984.

[30] L. D. Schuler, X. Daura, and W. F. J. van Gunsteren. *J. Comp. Chem.*, 22:1205, 2001.

[31] C. Oostenbrink, A. Villa, A. E. Mark, and W. F. van Gunsteren. *J. Comp. Chem.*, 25:1656–1676, 2004.

[32] B. R. Brooks, R. E. Bruccoleri, B. D. Olafson, D. J. States, S. Swaminathan, and M. Karplus. *J. Comput. Chem.*, 4:187, 1983.

[33] A. D. MacKerell, J. Wiorkiewicz-Kuczera, and M. Karplus. *J. Am. Chem. Soc.*, 117:11946, 1995.

[34] A. D. MacKerell Jr., D. Bashford, M. Bellot, R. L. Dunbrack Jr., J. D. Evanseck, M. J. field, S. Fischer, J. Gao, H. Guo, S. Ha, D. Joseph-McCarthy, L. Kuchnir, K. Kuczera, F. T. K. Lau, C. Mattos, S. Micknick, T. Ngo, D. T. Nguyen, B. Prodhom, W. E. Reiher, B. Roux, M. Schlenkrich, J. C. Smith, R. Stote, J. Straub, M. Watanabe, J. Wiorkiewicz-Kuczera, D. Yin, and M. Karplus. *J. Phys. Chem. B*, 102:3586, 1998.

[35] W. L. Jorgensen and J. Tirado Rives. *J. Am. Chem. Soc.*, 110:1657–1666, 1988.

[36] W. L. Jorgensen, D. S. Maxwell, and J. Tirado-Rives. *J. Am. Chem. Soc.*, 118:11225–11236, 1996.

[37] P. K. Weiner and P. A. Kollman. *J. Comput. Chem.*, 2:287, 1981.

[38] W. D. Cornell, P. Cieplak, C. I. Bayly, I. R. Gould, K. M. Merz, D. M. Ferguson, D. C. Spellmeyer, T. Fox, J. W. Caldwell, and P. A. Kollman. *J. Am. Chem. Soc.*, 117:5197, 1995.

[39] D. A. Pearlman, D. A. Case, J. W. Caldwell, W. S. Ross, T. E. Cheatham, S. DeBolt, D. Ferguson, G. Seibel, and P. A. Kollman. *Comput. Phys. Comm.*, 91:1, 1995.

[40] J. Qian, R. Hentschke, and W. Knoll. *Langmuir*, 13:7092–7098, 1997.

[41] D. Horinek, A. Serr, M. Geisler, T. Pirzer, U. Slotta, S. Q. Lud, J. A. Garrido, T. Scheibel, T. Hugel, and R. R. Netz. *Proc. Natl. Acad. Sci.*, 105:2842–2847, 2008.

[42] H. Heinz, R. A. Vaia, B. L. Farmer, and R. R. Naik. *J. Phys. Chem. C*, 112:17281–17290, 2008.

[43] H. Heinz, B. L. Farmer, R. B. Pandey, J. M. Slocik, S. S. Patnaik, R. Pachter, and R. R. Naik. *J. Am. Chem. Soc.*, 131:9704–9714, 2009.

[44] A. Pavese, M. Catti, S. C. Parker, and A. Wall. *Phys. Chem. Miner.*, 23:89, 1996.

[45] N. H. de Leeuw and S. C. Parker. *Phys. Rev. B*, 58:13091–13908, 1998.

[46] M. Wilson and T. R. Walsh. *J. Chem. Phys.*, 113:9180, 2000.

[47] N. H. de Leeuw and S. C. Parker. *Phys. Chem. Chem. Phys.*, 3:3217–3221, 2001.

[48] C. L. Freeman, J. H. Harding, D. J. Cooke, J. A. Elliot, J. S. Lardge, and D. M. Duffy. *J. Phys. Chem. C*, 111:11943–11951, 2007.

[49] C. L. Freeman, I. Asteriadis, M. Yang, and J. H. Harding. *J. Chem. Phys. C*, 113:3666–3673, 2009.

[50] P. Raiteri, J. D. Gale, D. Quigley, and P. M. Rodgers. *J. Phys. Chem. C*, 114:5997–6010, 2010.

[51] J. W. Shen, L. Li, N. F. A. van der Vegt, and C. Peter. *J. Chem. Theory Comput.*, 7:1916–1927, 2011.

[52] A. A. Skelton, P. Fenter, J. D. Kubicki, D. J. Wesolowski, and P. T. Cummings. *J. Phys. Chem. C*, 115:2076–2088, 2011.

[53] A. A. Skelton, D. J. Wesolowski, and P. T. Cummings. *Langmuir*, 27:8700–8709, 2011.

[54] L. B. Wright and T. R. Walsh. *J. Chem. Phys. C*, 116:2933–2945, 2012.

[55] P. E. M. Lopes, V. Murashov, M. Tazi, E. Demchuck, and Jr. A. D. MacKerell. *J. Phys. Chem. B*, 110:2782–2792, 2006.

[56] O. Alexiadis, V. A. Harmandaris, V. G. Mavrantzas, and L. Delle Site. *J. Phys. Chem. C*, 111:6380–6391, 2007.

[57] L. Delle Site and D. Sebastiani. *Phys. Rev. B*, 70:115401, 2004.

[58] M. Alimohammadi and K. A. Fichthorn. *J. Phys. Chem. C*, 115:24206–24214, 2011.

[59] K. Johnston, A. Gulans, T. Verho, and M. J. Pusk. *Phys. Rev. B*, 81:235428, 2010.

[60] J. P. Perdew, K. Burke, and Y. Wang. *Phys. Rev. B*, 54:16533, 1996.

[61] J. P. Perdew, K. Burke, and M. Ernzerhof. *Phys. Rev. Lett.*, 77:3865, 1996.

[62] J. P. Perdew, K. Burke, and M. Ernzerhof. *Phys. Rev. Lett.*, 78:1396(E), 1997.

[63] J. P. Perdew, K. Burke, A. Zupan, and M. Ernzerhof. *J. Chem. Phys.*, 108:1522, 1998.

[64] Y. Zhang and W. Yang. *Phys. Rev. Lett.*, 80:890, 1998.

[65] P. Perdew, K. Burke, and M. Ernzerhof. *Phys. Rev. Lett.*, 80:891, 1998.

[66] A. D. Becke. *Phys. Rev. A*, 38:3098, 1988.

[67] C. Lee, W. Yang, and R. G. Parr. *Phys. Rev. B*, 37:785, 1988.

[68] K. Johnston, J. Kleis, B. I. Lundqvist, and R. M. Nieminen. *Phys. Rev. B*, 77:121404(R), 2008.

[69] K. Tonigold and A. Groß. *J. Chem. Phys.*, 132:224701, 2010.

[70] J. Wellendorff, A. Kelkkanen, J. J. Mortensen, B. I. Lundqvist, and T. Bligaard. *Top. Catal.*, 53:378–383, 2010.

[71] H.-J. Kim, A. Tkatchenko, J.-H. Cho, and M. Scheffler. *Phys. Rev. B*, 85:041403, 2012.

[72] G. Li, I. Tamblyn, V. R. Cooper, H.-J. Gao, and J. B. Neaton. *Phys. Rev. B*, 85:121409(R), 2012.

[73] R. M. Nieminen K. Johnston and K. Kremer. *Soft Matter*, 7:6457, 2011.

[74] K. Wandelt and S. Thurgate. *Solid-liquid interfaces: Macroscopic phenomena - microscopic understanding*. Springer-Verlag, Berlin, 2003.

[75] S. Mann. *Biomineralization, Principles and Concepts in Bioinorganic Materials Chemistry*. Oxford, 2001.

[76] D. K. Chattopadhyay and K. V. S. N. Raju. *Prog. Polym. Sci.*, 32:352–418, 2007.

[77] E. Rauls, S. Blankenburg, and W. G. Schmidt. *Phys. Rev. B*, 81:125401, 2010.

[78] L. Pastewka, S. Moser, and M. Moseler. *Tribol. Lett.*, 39:49–61, 2010.

[79] G. Voskerician, M. S. Shive, R. S. Shawgo, H. von Recum, J. M. Anderson, M. J. Cima, and R. Langer. *Biomaterials*, 24:1959, 2003.

[80] G. Grundmeier, W. Schmidt, and M. Stratmann. *Electrochimica Acta*, 45:2515–2533, 2000.

[81] A. A. Skelton, T. Liang, and T. R. Walsh. *Appl. Mater. Interfaces*, 1:1482–1491, 2009.

[82] D. Bonn, J. Eggers, J. Indekeu, J. Meunier, and E. Rolley. *Rev. Mod. Phys.*, 81:739–805, 2009.

[83] D. J. Cole, M. C. Payne, and L. Colombi Ciacchi. *Phys. Chem. Chem. Phys.*, 11:11395–11399, 2009.

[84] D. E. Goldberg. *Genetic Algorithms in Search, Optimization, and Machine Learning*. Addison-Wesley Professional, 1989.

[85] J. D. Gale. *JCS Faraday Trans.*, 93:629, 1997.

[86] T. Strassner, M. Busold, and A. H. Wolfgang. *J. Comput. Chem.*, 23:282–290, 2002.

[87] M. Valtiner, M. Todorova, G. Grundmeier, and J. Neugebauer. *Phys. Rev. Lett.*, 103:065502, 2009.

[88] P. E. Bloechl. *Phys. Rev. B*, 24:17953, 1994.

[89] G. Kresse and J. Joubert. *Phys. Rev. B*, 3:1758, 1999.

[90] G. Kresse and J. Fuerthmueller. *Comp. Mat. Sci.*, 6:15, 1996.

[91] G. Kresse and J. Fuerthmueller. *Phys. Rev. B*, 54:11169, 1996.

[92] A. V. Berezkin, P. Schravendijk, and P. U. Biedermann. *manuscript in preparation*.

[93] R. S. Mulliken. *J. Chem. Phys.*, 23:1833–1840, 1955.

[94] I. G. Csizmadia. *Theory and Practice of MO Calculations on Organic Molecules*. Elsevier, Amsterdam, 1976.

[95] F. M. Bickelhaupt, N. J. R. van Eikema Hommes, C. Fonseca Guerra, and E. J. Baerends. *Organometallics*, 15:2923–2931, 1996.

[96] M. Schiek, K. Al-Shamery, M. Kunat, F. Traeger, and Ch. Wöll. *Phys. Chem. Chem. Phys.*, 8:1505–1512, 2006.

[97] W. Humphrey, A. Dalke, and K. Schulten. *J. Molecular Graphics Modell.*, 14:33–38, 1996.

[98] B. Hess, C. Kutzner, D. van der Spoel, and E. Lindahl. *J. Chem. Theory Comput.*, 4:435–447, 2008.

[99] U. Essmann, L. Perera, M. L. Berkowitz, T. Darden, H. Lee, and L. G. Pedersen. *J. Chem. Phys.*, 103:8577–8593, 1995.

[100] H. J. C. Berendsen, J. P. M. Postma, W. F. van Gunsteren, and J. Hermans. *Interaction Models for Water in Relation to Protein Hydration, in Intermolecular Forces*. D. Reidel Publishing Company, Dordrecht, 1981.

[101] G. Kresse and J. Hafner. *Phys. Rev. B*, 48:13115, 1993.

[102] M. Dion, H. Rydberg, E. Schröder, D. C. Langreth, and B. I. Lundqvist. *Phys. Rev. Lett.*, 95:109902(E), 2005.

[103] A. Gulans, M. J. Puska, and R. M. Nieminen. *Phys. Rev. B*, 79:201105(R), 2009.

[104] G. Henkelman, A. Arnaldsson, and H. Jonsson. *Comput. Mat. Sci.*, 36:254–360, 2006.

[105] E. Sanville, S. D. Kenny, R. Smith, and G. Henkelman. *J. Comp. Chem.*, 28:899–908, 2007.

[106] W. Tang, E. Sanville, and G. Henkelman. *J. Phys.: Condens. Matter*, 21:084204, 2009.

[107] N. S. Sangaj and V.C. Malshe. *Prog. Org. Coat.*, 50:28–39, 2004.

[108] G. Grundmeier and M. Stratmann. *Annu. Rev. Mater. Res.*, 35:571–615, 2005.

[109] K. N. Allahar, B. R. Hinderliter, D. E. Tallman, and G. P. Bierwagen. *J. Electrochem. Soc.*, 155:F201–F208, 2008.

[110] V. Sauvant-Moynot, S. Gonzalez, and J. Kittel. *Prog. Org. Coat.*, 63:307–315, 2008.

[111] P. A. Sorensen, S. Kiil, K. Dam-Johansen, and C. E. Weinell. *J. Coat. Technol. Res.*, 6:135–176, 2009.

[112] S. Vlad, I. Spiridon, C. Vasile Grigoras, M. Drobota, and A. Nistor. *e-Polymers*, 004:1–11, 2009.

[113] J. Bandekar and S. Klima. *J. Mol. Struc.*, 263:45–47, 1991.

[114] J. Bandekar and S. Klima. *Spectrochimica Acre*, 48A:1363–1370, 1992.

[115] L. Ning, W. De-Ning, and Y. Sheng-Kang. *Macromolecules*, 30:4405–4409, 1997.

[116] L.-S. Teo and C.-Y. Chen ad J.-F. Kuo. *Macromolecules*, 30:1793–1799, 1997.

[117] R. L. McKiernan, A. M. Heintz, S. L. Hsu, E. D. T. Atkins, J. Penelle, and S. P. Gido. *Macromolecules*, 35:6970–6974, 2002.

[118] V. Romanova, V. Begishev, V. Karmonov, A. Kondyurin, and M. F. Maitz. *J. Raman Spectrosc.*, 33:769–777, 2002.

[119] H. Sun. *Macromolecules*, 26:5924–5936, 1993.

[120] E. Yilgör and I. Yilgör E. Yurtsever. *Polymer*, 43:6551–6559, 2002.

[121] G. D. Smith, D. Bedrov, O. Byutner, O. Borodin, C. Ayyagari, and T. D. Sewell. *J. Phys. Chem. A*, 107:7552–7560, 2003.

[122] Z. Ren, D. Ma, and X. Yang. *Polymer*, 44:6419–6425, 2003.

[123] J. Repakova, P. Capkova, M. Studenovsky, and Ilavsky M. *J. Mol. Model.*, 10:240–249, 2004.

[124] Z. Ren, X. Zeng, X. Yang, D. Ma, and S. L. Hsu. *Polymer*, 46:12337–12347, 2005.

[125] P. Cysewski, P. Krol, and A. Shyichuk. *Macromol. Theory Simul.*, 16:541–547, 2007.

[126] D. Fritz and K. Kremer. *in preparation*, 2012.

[127] H. Takeuchi and K. Okazaki. *J. Chem. Phys.*, 92:5643–5652, 1990.

[128] J. Sonnenburg, J. Gao, and J. H. Weiner. *Macromolecules*, 23:4653–4657, 1990.

[129] H. Takeuchi. *J. Chem. Phys.*, 93:2062–2067, 1990.

[130] H. Takeuchi. *J. Chem. Phys.*, 93:9042–9048, 1990.

[131] F. Müller-Plathe. *J. Chem. Phys.*, 94:3192–3199, 1991.

[132] A. A. Gusev and U. W. Suter. *J. Chem. Phys.*, 99:2228–2234, 1993.

[133] A. A. Gusev, F. Müller-Plathe, W. F. van Gunsteren, and U. W. Suter. *Adv. Polym. Sci.*, 116:207–247, 1994.

[134] F. Müller-Plathe. *Acta Polym.*, 45:259–293, 1994.

[135] F. Müller-Plathe. *Macromolecules*, 29:4782–4791, 1996.

[136] F. Müller-Plathe. *J. Membr. Sci.*, 141:147–154, 1998.

[137] D. Hoffmann, L. Fritz, J. Ulbrich, C. Schepers, and M. Bohning. *Macromol. Theor. Simul.*, 9:293–327, 2000.

[138] D. Fritz, C. R. Herbers, K. Kremer, and N. F. A. van der Vegt. *Soft Matter*, 5:4556–4563, 2009.

[139] Ch. Wohlfarth and B. Wohlfarth. *Landolt-Börnstein, New Series: Surface Tension of Pure Liquids and Binary Liquid Mixtures, V/16 2.17*. SpringerMaterials, 1997.

[140] M. Parrinello and A. Rahman. *J. Appl. Phys.*, 52:7182–7190, 1981.

[141] S. Nose and M. L. Klein. *Mol. Phys.*, 50:1055–1076, 1983.

[142] S. Nose. *Mol. Phys.*, 52:255–268, 1984.

[143] W. G. Hoover. *Phys. Rev. A*, 31:1695–1697, 1985.

[144] B. Hess, H. Bekker, H. J. C. Berendsen, and J. G. E. M. Fraaije. *J. Comput. Chem.*, 18:1463–1472, 1997.

[145] L. Martinez, R. Andrade, E. G. Birgin, and J. M. Martinez. *J. Comp. Chem.*, 30:2157–2164, 2009.

[146] M. L. Greenfield and D. N. Theodorou. *Macromolecules*, 31:7068–7090, 1998.

[147] B. Hess, S. Leon, N. F. A. van der Vegt, and K. Kremer. *Soft Matter*, 2:409–414, 2006.

[148] V. A. Harmandaris, N. P. Adhikari, N. F. A. van der Vegt, and K. Kremer. *Macromolecules*, 39:6708–6719, 2006.

[149] V. A. Harmandaris, D. Reith, N. F. A. van der Vegt, and K. Kremer. *Macromol. Chem. Phys.*, 208:2109–2120, 2007.

[150] V. A. Harmandaris, N. P. Adhikari, N. F. A. van der Vegt, K. Kremer, B. A. Mann, R. Voelkl, H. Weiss, and C. C. Liew. *Macromolecules*, 40:7026–7035, 2007.

[151] V. A. Harmandaris and K. Kremer. *Macromolecules*, 42:791–802, 2009.

[152] D. Fritz, V. Harmandaris, K. Kremer, and N. F. A. van der Vegt. *Macromolecules*, 42:7579–7588, 2009.

[153] G. A. Voth, editor. *Coarse-Graining of Condensed Phase and Biomolecular Systems*. CRC Press, New York, 1 edition, 2009.

[154] O. Hahn, D. A. Mooney, F. Müller-Plathe, and K. Kremer. *J. Chem. Phys.*, 111:6061–6068, 1999.

[155] B. Hess, C. Peter, T. Ozal, and N. F. A. van der Vegt. *Macromolecules*, 41:2283–2289, 2008.

[156] B. Hess and N. F. A. van der Vegt. *Macromolecules*, 41:7281–7283, 2008.

[157] T. A. Ozal, C. Peter, B. Hess, and N. F. A. van der Vegt. *Macromolecules*, 41:5055–5061, 2008.

[158] C. D. Wick, M. G. Martin, and J. I. Siepmann. *J. Phys. Chem. B*, 104:8008–8016, 2000.

[159] H. J. C. Berendsen, J. P. M. Postma, W. F. van Gunsteren, A. DiNola, and J. R. Haak. *J. Chem. Phys.*, 81:3684–3690, 1984.

[160] G. Bussi, D. Donadio, and M. Parrinello. *J. Chem. Phys.*, 126:014101, 2007.

[161] M. P. Allen and D. J. Tildesley. *Computer Simulation of Liquids*. Clarendon, Oxford, 1987.

[162] P. Zoller and D. J. Walsh. *Standard Pressure-Volume-Temperature Data for Polymers*. Technomic, Lancaster, 1995.

[163] W. Tschoep, K. Kremer, O. Hahn, J. Batoulis, and T. Bürger. *Acta Polym.*, 49:75–79, 1998.

[164] T. Mulder, V. A. Harmandaris, A. V. Lyulin, N. F. A. van der Vegt, K. Kremer, and M. A. J. Michels. *Macromolecules*, 42:384–391, 2009.

[165] C. Jarzynski. *Phys. Rev. Lett.*, 78:2690, 1997.

[166] D. Ambrose, B. E. Broderick, and R. Townsend. *J. Chem. Soc. A*, 633–641, 1967.

[167] R. H. Schuster, H. Gräter, and H.-J. Cantow. *Macromolecules*, 17:619–625, 1984.

[168] E. Brini, V. Marcon, and N. F. A. van der Vegt. *Phys. Chem. Chem. Phys.*, 13:10468–10474, 2011.

[169] S. Pandiyan, D. Brown, S. Neyertz, and N. F. A. van der Vegt. *Macromolecules*, 43:2605–2621, 2010.

[170] D. Fritz, K. Koschke, V. A. Harmandaris, N. F. A. van der Vegt, and K. Kremer. *Phys. Chem. Chem. Phys.*, 13:10412, 2011.

[171] H. Eslami, H. A. Karimi-Varzaneh, and F. Müller-Plathe. *Macromolecules*, 44:3117–3128, 2011.

[172] L. Delle Site, C. Holm, and N. F. A. van der Vegt. *Top. Curr. Chem.*, 307:251–294, 2012.

[173] C. Li, J. Shen, C. Peter, and N. F. A. van der Vegt. *Macromolecules*, 45:2551–2561, 2012.

[174] F. Müller-Plathe. *Chem. Phys. Chem.*, 3:754–769, 2002.

[175] C. Chen, P. Depa, J. K. Maranas, and V. Garcia Sakai. *J. Chem. Phys.*, 128:124906, 2008.

[176] P. Carbone, H. A. Karimi Varzaneh, X. Chen, and F. Müller-Plathe. *J. Chem. Phys.*, 128:064904, 2008.

[177] S. J. Marrink, H. J. Risselada, S. Yefimov, D. P. Tieleman, and A. H. de Vries. *J Phys. Chem. B*, 111:7812–7824, 2007.

[178] K. A. Maerzke and J. I. Siepmann. *J. Phys. Chem. B*, 115:3452–3465, 2011.

[179] J. D. McCoy and J. G. Curro. *Macromolecules*, 31:9362–9368, 1998.

[180] B. M. Mognetti, P. Virnau, L. Yelash, W. Paul, K. Binder, M. Müller, and L. G. MacDowell. *J. Chem. Phys.*, 130:044101, 2009.

[181] D. Reith, M. Pütz, and F. Müller-Plathe. *J. Comput. Chem.*, 24:1624–1636, 2003.

[182] A. Lyubartsev and A. Laaksonen. *Phys. Rev. E*, 52:3730–3737, 1995.

[183] F. Ercolessi and J. Adams. *Europhys. Lett.*, 26:583, 1994.

[184] N. Zacharopoulos, N. Vergadou, and D. N. Theodorou. *J. Chem. Phys.*, 122:244111, 2005.

[185] A. Villa, N. F. A. van der Vegt, and C. Peter. *Phys. Chem. Chem. Phys.*, 11:2068–2076, 2009.

[186] Y. Wang, W. G Noid, P. Liu, and G. A. Voth. *Phys. Chem. Chem. Phys.*, 11:2002–2015, 2009.

[187] B. Widom. *J. Chem. Phys.*, 39:2802, 1963.

[188] C. Peter and N. F. A. van der Vegt. *J. Phys. Chem. B*, 111:7836–7842, 2007.

[189] N. F. A. van der Vegt, V. A. Kusuma, and B. D. Freeman. *Macromolecules*, 43:1473, 2010.

[190] D. Ben-Amotz, F. O. Raineri, and G. Stell. *J. Phys. Chem. B*, 109:6866–6878, 2005.

[191] N. F. A van der Vegt and W. F. van Gunsteren. *J. Phys. Chem. B*, 108:1056–1064, 2004.

[192] V. Marcon, D. Fritz, and N. F. A. van der Vegt. *Soft Matter*, (accepted), 2012.

[193] H. Wu, A. Borhan, and K. A. Fichthorn. *J. Low. Temp. Phys.*, 157:277–295, 2009.

[194] T. Sanghi and N. R. Aluru. *J. Chem. Phys.*, 132:044703, 2010.

[195] D. M. Huang, R. Faller, K. Do, and A. D. Moule. *J. Chem. Theory Comput.*, 6:526–537, 2010.

[196] A. Ghanbari, T. V. M. Ndoro, F. Leroy, M. Rahimi, M. C. Böhm, and F. Müller-Plathe. *Macromolecules*, 45:572–584, 2012.

[197] D. Reith, M. Pütz, and F. Müller-Plathe. *J. Comput. Chem.*, 24:1624–1636, 2003.

Curriculum Vitae

Name:	Claudia Rosemarie Herbers
Place of Birth:	Lingen (Ems), Germany
Date of Birth:	17.01.1984
Nationality:	German

Education:

1994 – 2003:	Franziskusgymnasium Lingen (Ems)
10/2003 – 05/2008:	Westfälische Wilhelm-Universität Münster (Chemisty Studies)
07/2008 – 05/2009:	Max Planck Institute for Polymer Reseach, Mainz
05/2009 – 06/2012:	Center of Smart Interfaces, Darmstadt University of Technology (Doctoral Studies)

_____

(Claudia R. Herbers)

Claudia Herbers
Kaiserstr. 36
55116 Mainz

Tel.: 0176 22718922
E-mail: herbers@csi.tu-darmstadt.de

Darmstadt, den 03. Mai 2012

Erklärung

Ich erkläre hiermit, noch keinen Promotionsversuch unternommen zu haben.

_____

(Claudia R. Herbers)

Claudia Herbers
Kaiserstr. 36
55116 Mainz

Tel.: 0176 22718922
E-mail: herbers@csi.tu-darmstadt.de

Darmstadt, den 03. Mai 2012

Eidesstattliche Erklärung

Ich erkläre mich hiermit an Eides Statt, dass ich meine Dissertation selbständig und nur mit den angegebenen Hilfen angefertigt habe.

_____

(Claudia R. Herbers)